Eindhoven University of Technology

MASTER

Implementation of pattern matching and photogrammetric measurement techniques for bed evolution through a moving water surface

Wilting, Twan J.S.

Award date:
2019

Link to publication

EINDHOVEN UNIVERSITY OF TECHNOLOGY

Department of Applied Physics
Turbulence and Vortex Dynamics

Implementation of pattern matching and photogrammetric measurement techniques for bed evolution through a moving water surface

Master Thesis

T.J.S. Wilting

First version

Eindhoven, January 2019

Abstract

This study presents results of the implementation and performance of two morphological measurement optical techniques. These techniques can measure the changing underwater sediment bed thickness in a fast, non-intrusive, safe and cheap manner using only a digital projector and one camera. The digital projector, positioned under an angle, projects a set of dot patterns onto the sediment bed that is photographed by the camera. The first measurement technique is a pattern matching technique, in which variations in the projected dot patterns on the sediment bed are related to changes in the height of the sediment bed. The second measurement technique is a photogrammetric technique. This technique calculates the intersections between the light trajectories from the projector to the illuminated dots on the bed and from the centroid of these dots on the bed to the camera. The intersections correspond to the positions of the dots on top of the sediment bed.

Both techniques are first tested and investigated for dry and stagnant underwater conditions, where refraction at the water surface is included. The height calculations of the photogrammetric technique are superior to the pattern matching technique, and reflection is only included in the photogrammetric technique.

Afterwards, we performed underwater measurements of the changing morphology under an oscillating flow inside a channel during flow reversal. These measurements where complemented with simultaneous Particle Image Velocimetry (PIV) measurements of the flow velocity at the water surface. A random sediment distribution self-organizes into a ripple that migrates through the tidal channel. PIV measurements show an asymmetry in the oscillating flow that explains this migration.

Preface

This master thesis is written as a result of my graduation project at the Technical University of Eindhoven (TU/e) over the past 15 months. After my (experimental) Bachelor project at the WDY group, where I studied the residual currents inside a semi-enclosed basin subjected to tides via a tidal inlet, I wanted to do an experimental Master project in the same group since their research inspired me, resulting in a (still) growing passion for experimental fluid dynamics. During my research, I gained not only a lot of hands-on experience while constructing and optimizing the measurement techniques, but also a way of scientific reasoning further increasing my curiosity in general (experimental) physics. In the beginning of this project, my supervisor gave me the freedom to propose my own ideas and define a self-chosen research topic. From the conclusions and recommendations of previous works and open questions that I could find in literature, I came up with a several proposals. None of the first ideas were planned thoroughly and thus rejected. I improved the quality of new experiments that could be performed in the laboratory tank that was assigned to me. Finally, after weeks of exploration, an interesting phenomenon was found in one of the test configurations. In a specific set of conditions, I had found sand patches/dunes that were stable and migrated trough the channel. The study of (scaled) migrating sand dunes in a tidal channel where the effect of a standing vortex is investigated, was a straightforward problem to investigate. Morphodynamic measurements together with Particle Image Velocimetry (PIV) measurement could then be used to look for a possible relation in the velocity field at the free water surface and the bed morphology.

After a while, I found a few seemingly inexplicable artifacts in the measurement technique. Via a new and more complete description, better calculations were proposed until finally, after 9 months, I found yet another incorrect aspect between the location on images and real world coordinates. Unfortunately, these misunderstandings can not be planned beforehand which meant that sometimes weeks of (experimental) work had to be redone and rewritten due to a new/more complete description. These setbacks together with the loss of two loved ones, J. who was a wonderful person and S. to whom I owe a lot of love and support during my Master, made it sometimes difficult but showed me that changes allow for a new start. It is due to all the support I received from the people around me that I could complete this work. I would therefore like to use this opportunity to express my gratitude to the people who helped me during the past year(s). In particular, I would like to thank my graduation supervisor Matias Duran-Matute, who was always willing to help and guide the work when necessary. Also, I would like to thank the (technical) support I received from Gerald Oerlemans, Freek van Uitterd and especially Samuel Gonzalez and Ad Holten who worked with me many hours in the lab and from whom I learned many practical aspects. Last but not least, I would like to thank all my fellow students, family and friends who always supported me during the past year.

I hope you will enjoy reading this thesis,

Twan Wilting

Contents

Chapter 1

Introduction

In the study of sediment transport and morphodynamics, laboratory experiments have always been crucial for the understanding of basic processes and the development of a theoretical framework. This is because the conditions in laboratory setups can easily be controlled, which allows isolating particular physical phenomena and systematically change the values of the governing parameters. For example, Bagnold (1946) who studied the influence of the wave amplitude on sand ripples, McLaren & Bowles (1985) who investigated the effect of sediment transport on grain-size distribution or the study of Aagaard *et al.* (2004) where the effects of sea level rise are investigated on the morphological evolution of the shore. Despite possible scaling issues in these experiments, they are not bounded by the discretization in space and time, or approximations found in numerical simulations.

In experimental morphological studies, there is an increasing need for non-intrusive accurate techniques to measure changes in underwater sediment beds with a high spatial and temporal resolution. These measurements are performed in either dry conditions, by removing the water in the setup before performing the measurement, or in underwater conditions. The underwater measurements can be performed in stagnant conditions or during the experiment itself. The latter is, clearly, the only possibility to measure the transient bed evolution without disturbing the system by, for example, pausing the experiment or removing the water. However, the measurement techniques must be fast and be capable of dealing with the aquatic medium by either using underwater equipment or considering the change from air to water.

There is a range of different measurement techniques that can be used to measure the bed changes in laboratory experiments. However, each of them has its own advantages and limitations. The classic technique is a graded rod placed vertically on the sediment bed, but with this technique the bed thickness is measured only at one location at a time. In the past two decades, a number of more advanced techniques have been developed. For example, measuring the electrical resistance between the top and bottom of the bed to calculate the thickness (Rooij, Dalziel & Linden 1999). In terms of optical techniques there are more non-intrusive techniques such as a light attenuation technique, where the light passing through a bed of translucent sediment is used to estimate the bed thickness. This technique was used by Munro & Dalziel (2005) to measure the changes in bed thickness after a downward traveling vortex collides with the sediment bed. Both of these techniques allow for fast measurements but are limited in the type of sediment particles and range of sediment layer thickness. Moreover, they require specific practical conditions like a transparent bottom wall for light exposure. A different method is an ultrasonic depth profiler or echo-sound measurement techniques. They can provide accurate reconstructions of the bed level but are expensive and limited in temporal resolution and thus incapable of measuring a transient bed morphology (Porter, Simons & Harris 2014). Other optical measurement techniques use a laser projection of a (single) line or a dot pattern that is projected onto the sediment. Via a photogrammetric technique, one can triangulate the positions of the patterns on the bed captured

by calibrated cameras (Stancanelli *et al.* (2011); Sumer *et al.* (2012); Baglio *et al.* (2001) and Foti *et al.* (2011)). A laser can provide high intensity lines or points and is often used to measure two or three dimensional bed profiles in experiments with suspended (sediment) particles. In a recent study of Cebrián-Robles & Ortega-Casanova (2016), a set of laser lines is used to perform three dimensional measurements. The illumination by a digital projector allows for safer projections and more flexibility in the chosen patterns (Gorte, Vargas-Luna & Sirmacek (2013) and Porter, Simons & Harris (2014)).

In this work, we present two calculation methods of the bed morphology that only use a single camera and a digital projector. The first measurement technique is called a pattern matching technique and is based on the work of Munro, Dalziel & Jehan (2004), who studied the same morphological changes as Munro & Dalziel (2005), where a downward traveling ring vortex collides on a sediment bed. Because the patterns are projected under an angle, changes in the height of the bed deform the photographed pattern. Via pattern matching, we use these changes and calculate the corresponding variation in bed thickness. The second technique is a photogrammetric technique, where we use triangulation to measure the bed thickness. The most studies using photogrammetry use two or more cameras to triangulate projected patterns. However, during this project we only use one single camera. When a dot is projected onto the sediment bed and captured by the camera, one can find the light trajectories from the projector to the illuminated dot and from the centroid of the dot to the camera. Since these two trajectories intersect at the bed, we calculate this intersection point for each dot on the image. The science that retrieves three dimensional information of photographed objects out of the images, is called photogrammetry. Since both techniques presented here use the images of the dot projections to calculate the height, each techniques can be seen as a different form of photogrammetry. The name difference in current work is chosen according to the work of Munro, Dalziel & Jehan (2004), whose measurement technique is referred to as the pattern matching technique.

The techniques are tested and implemented into a system of an oscillating flow to investigate the performance of underwater morphological measurements trough a moving water surface. The oscillating flow is a tidal motion inside a channel in which the water level varies over time. To correctly calculate the reflection at the water surface, a synchronisation of the measurement moments and tidal motion is required. Moreover, the measurements have to be performed in a short time interval to remove variations of the water level.

When sediment is added on the bottom of the channel, the bed morphology changes over time and measurements are performed during flow reversal. During the time interval of flow reversal we can measure the stationary sediment bed thickness due to the absence of bed-load transport during the change of tides. We have added a Particle Image Velocimetry (PIV) measurement technique to measure the velocity field at the water surface. Via UV LED lights we illuminate luminescent particles and photograph their displacement over time using a PIV camera. Via a novel synchronisation between the illumination of projector and illumination of the PIV tracer particles, we can perform both measurements simultaneously. We investigated the transient behaviour of a perturbed sediment bed and measured the migration of these perturbation inside the channel. We found that these sediment patches self-organize into dunes and migrate trough the channel. This experimental setup together with the PIV and the morphological measurement techniques, can be used to investigate the formation and migration of dunes in a tidal channel. More experiments have to be performed to find a possible relation between the measured transient morphology and the measured asymmetric tidal fluid velocity.

At several tidal inlets world wide, the presence of sediment banks on the bottom of the tidal channel have been observed. An example of such an observation can be found between the North Sea and the Wadden Sea, where the presence of sand bank is revealed during low tide, shown in figure 1.1. The Wadden Sea is connected to the North Sea by multiple tidal inlets and is strongly influenced by the tidal motions of the North Sea (Duran-Matute *et al.* 2014). These connections are also be found elsewhere. For instance in a harbour, bay or an estuary that is connected to the ocean via a tidal channel. Therefore, they are subject to the influence of the tides. As a result of

Figure 1.1: Example of sand banks in the Wadden Sea where an aerial photograph taken during low tide. It reveals the presence of a variety of sand banks (Holger Weitze, 2018).

the rising and falling of the sea level, a tidal flow will be induced trough these channels.
The hydrodynamics inside these tidal channels are strongly controlled by the morphodynamics and tidal motion, possibly resulting in a net transport of sediment due to tidal asymmetry or the occurrence of sand banks (Solari *et al.* 2002). Many studies are devoted to the sediment transport inside tidal inlets as they are important conduits between estuarine waters and ocean for the movement of contaminants and nutrients (e.g. Signell & Butman (1992) and Sheng, Peene & Yassuda (1996)), sediments (Christiansen, Wiberg & Milligan 2000), and biota (Fagherazzi & Sun 2004). Improving our understanding of the processes in these systems and predicting their long-term evolution is a critical step when addressing issues of conservation of tidal systems, exposed to the effects of climate changes and human interference (Elias & van der Spek (2006) and Ridderinkhof *et al.* (2016)). A wide literature exists, describing the hydrodynamics of tidal systems and their morphodynamic evolution (see, e.g., Allen (2000); Friedrichs & Perry (2001); Fagherazzi & Overeem (2007) and De Swart & Zimmerman (2009) for thorough reviews).
Next to the theoretical work, (Hench & Luettich Jr (2003); Van der Molen, Gerrits & De Swart (2004)) experimental studies have been performed to investigate morphological processes in laboratory conditions (Tambroni, Bolla Pittaluga & Seminara (2005); Kleinhans *et al.* (2014) and Stefanon *et al.* (2010)). These studies can validate aspects of new theoretical models since the conditions in laboratory setups can easily be controlled with respect to field measurements (Barnard *et al.* (2013) and references therein). In contrast, laboratory experiments are often scaled versions and a correct scaling is required and not always possible (Claudin & Andreotti 2006).

The report is organized as follows. Chapter 2 presents the projected dot patterns, pattern matching technique and photogrammetric technique. The basic principles of both techniques and height calculations are explained together with two possible approximations of the pattern matching technique. After the techniques are discussed, we give a comparison between the two techniques. Chapter 3 describes the experimental setup that is used to perform non-intrusive morphological measurements trough a moving water layer. This setup is used to study the (scaled) morphodynamics inside a tidal channel. The implementation of PIV and the synchronization to the tidal motion are discussed before the results of the measured sediment beds and velocity fields are given. The conclusions of the techniques together with recommendations for future work are given in Chapter 4.

Chapter 2

Morphological measurement techniques

In order to study the morphodynamics of an underwater sediment bed in real time, a non-intrusive and fast measurement technique is required. Two different measurement techniques are presented here: a pattern matching technique and a photogrammetric technique. Both techniques use a digital projector and a single camera. By positioning the camera and digital projector outside the (moving) water, a non intrusive optical measurement can be performed. The accuracy of both measurement techniques is investigated in this project. The speed of the measurement techniques depends primarily on the properties of the camera and digital projector, i.e. the frame rates at which images and projections can be made.

The digital projector is positioned under an angle and projects a set of dot patterns onto the sediment bed, as shown in figure 2.1. These projection are then photographed by the camera placed on top of the setup looking down. The projected patterns consist of ellipses. When these ellipses are projected onto a horizontal surface, they appear as circles on the photographs taken by the camera. In the remainder of this work, these ellipses are referred to as circles or dots.

Because the projector is positioned under an angle, a variation in the sediment bed thickness $h(x, y)$ results in a deformation in the projected pattern, indicated by the black dots in figure 2.1. These displacements of the locations of the projected dots are captured by the camera and are used to calculate the corresponding height difference.

This chapter describes all technical and theoretical aspects of the measurement techniques, and is organized as follows. The dot patterns, projected by the digital projector and captured by the camera, are discussed in section 2.1. Three different version of the pattern matching technique are given in section 2.2. In section 2.3, we present the photogrammetric technique. A comparison on the performance of both techniques is given in section 2.4.
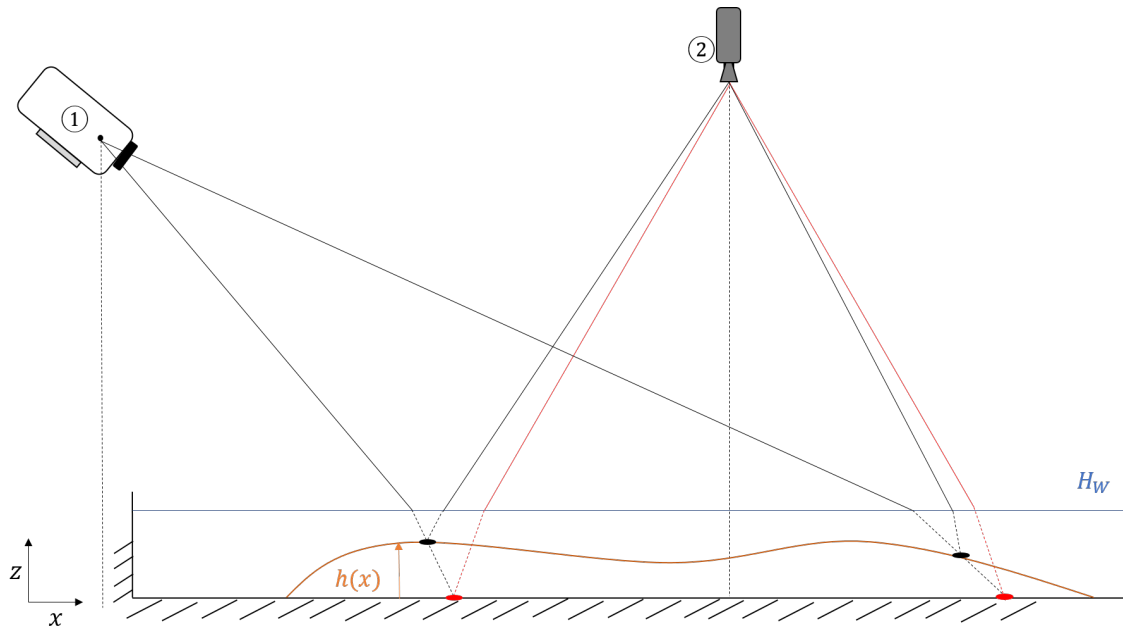
Figure 2.1: Two dimensional schematic side view of the morphological measurement setup. A digital projector ① is positioned under an angle and projects a set of dot patterns on the sediment bed. Two dots are used as an example and are indicated by the black and red dots. The red dots represent the position of the projected dots during an underwater reference measurement (no sediment). The black dots represent the position of the projected dots that are projected on the measured sediment bed indicated by the brown curved $h(x)$. The camera ② photographs the projected grid patterns on the sediment bed. The red lines indicate the trajectory of the dot captured in the reference measurement whereas the black lines indicate the trajectory of the dot on the sediment. The dot patterns and the field of view of the camera are deformed due to refraction at the water surface $z = H_W$ and are indicated by dashed lines.

2.1 Imaging and projections

The dot patterns are projected by the digital projector and form a 10×20 grid of dots. In total, 15 different projections are used to measure the bed morphology. An image of the first projected projection as captured by the camera is given in figure 2.2. Every projection consists of the same 10×20 grid of dots, but the projections are shifted to cover the entire measurement area (65 cm $\times$ 21 cm).

This is shown schematically in figure 2.3, where the order of the projections is indicated. The order here is randomized due to practical limitations of the technique inside the tidal channel. The entire measurement area consists of $15 \times 10 \times 20 = 3000$ dots, at which the sediment bed thickness is measured using the position of the centroid of the dots.

The diameter of the projected dots was optimized for detection and to increase the spatial resolution inside the measurement area. When the size of the dots decreases, the number of dots per projection can be increased. Decreasing the number of projections needed to cover the entire measurement area, and thus the measurement time. However, smaller dots are more sensitive to image distortion due to the roughness of the sediment, which decreases the performance of the detection of the centroids of the projected dots. Through testing, we found an optimal size for the dots to be approximately 2.5 times the particle diameter of the sediment used in current work ($d_p \approx 2.1$ mm).

To avoid overlapping and merging of the projected dots, a minimum distance between the dots is required. This distance depends on the deformations of the sediment bed and the angle of projection. In the current setup, we did not investigate the effect of the projection angle, and the projector is positioned under an fixed angle. For the particular experiments discussed in this report, the magnitude of ΔX and ΔY are not equal. The projected dots will shift predominantly in the $x-$direction due to the positioning of the projector. A maximum horizontal displacement of the dot, corresponds to the maximum height difference that is limited by the angle of repose of the sediment. By testing the expected height differences, we found that the maximum dot displacement is less than four times the diameter of the projected dot. Therefore, a sufficient ΔX of five dot diameters was chosen. The distance between two columns in the $y-$direction ΔY is three times the dot diameter. The result is a 3×5 division of the structured grid, shown in figure 2.3. The ΔY value between dots could be further decreased since only small variations in $y-$direction occur for the bedmorphologies that where found in the test conditions. These bed morphologies have little variation along the $y-$direction and a maximum height h of 3.5 cm was found under the initial set of testing conditions. The projected pattern used in this project is generated using prior knowledge of the bed morphology. When no such information is known, a set of test runs might be required to optimize the dots size and positioning.
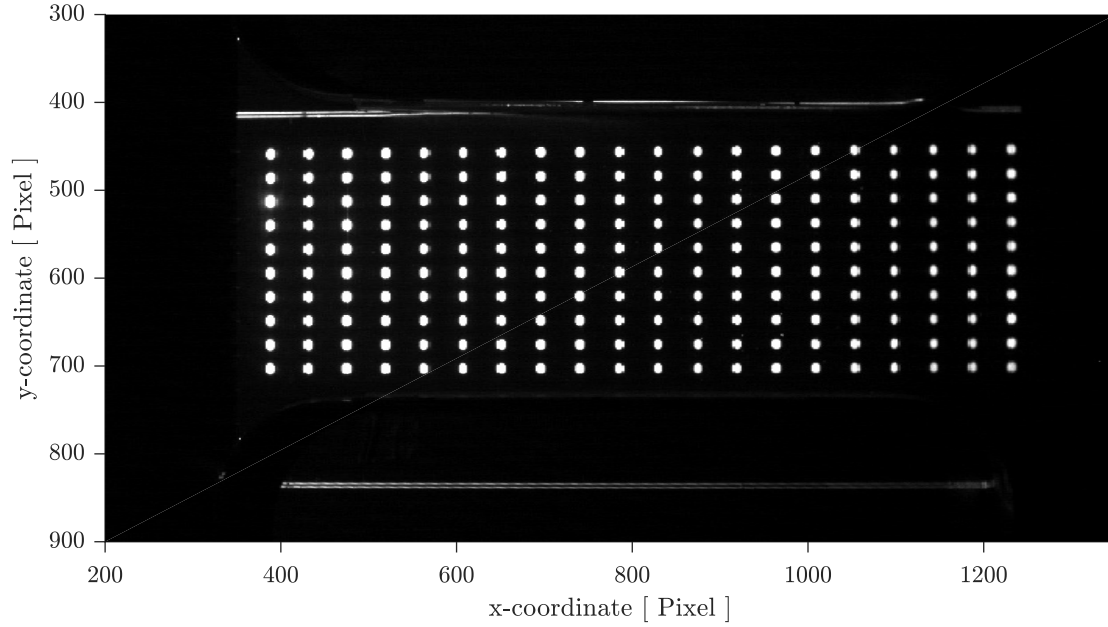
Figure 2.2: Photograph of the first projected dot pattern, consisting 200 dots positioned in 10 rows and 20 columns. The patterns is projected on the flat horizontal bottom $z = 0$ cm, under a water level $H_W = 7$ cm. The measurement area is 65 cm $\times$ 21 cm.
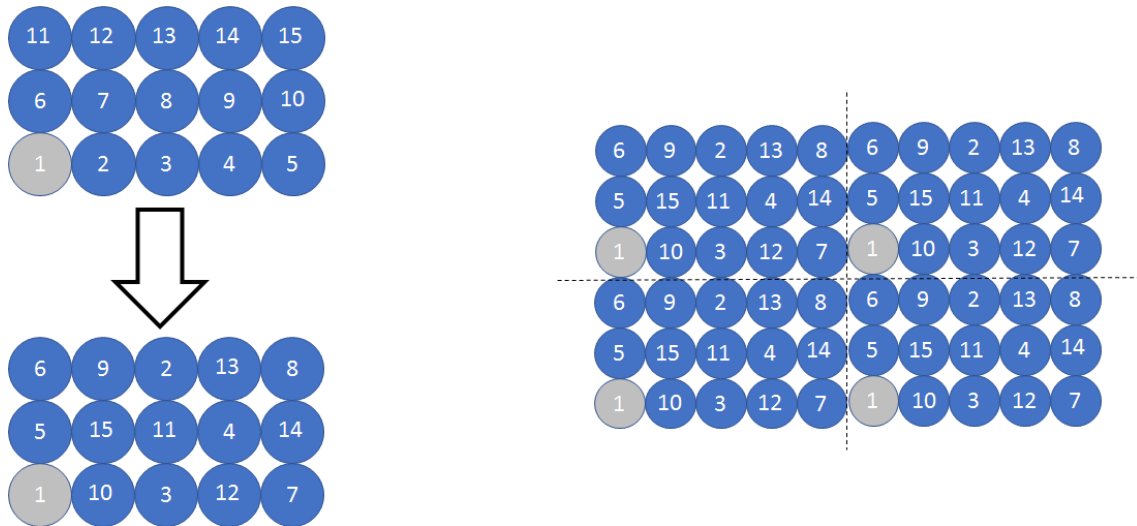
Figure 2.3: Schematic representation of a section of the projected dot patterns. The numbers correspond to the order of patterns (total of 15 patterns). The order at which each pattern is projected is randomized. A collection of four sections is shown at the right. The grey dots indicate four out of the 200 dots from the first projection, as is shown in figure 2.2.

In the raw image taken by the camera, shown in figure 2.2, there is a decrease in the light intensity along the x-direction, resulting in decreasing dot sizes. This is a results of the illumination of the digital projector with respect to the camera. The angle of the projected and reflected light rays increases along the x-direction. Therefore, the intensity of the light captured by the camera decreases, resulting in a decreasing area size. Despite the changes in the area size, we assume that the measured centroid of the dot does not depend on the light intensity. The gradient in light intensity strongly depends on the surface onto which the dots are projected. In the reference measurements, the dots are projected onto a metal bottom plate, which reflects most of the incoming light. However, in the case of sediment, there is less reflection and an increase in scattered light. Therefore, the intensity of the dots is almost constant throughout the measurement area. By using an adaptive Matlab transformation *imbinarize*, using gradients in the intensity, we can convert images to binary and accurately measure all the centroids of the projected dots for underwater measurements, shown ine figure 2.4 (b). These binary maps are used to determine the location of the centroid of every dot in pixel coordinates (x_p, y_p).

The height calculation of the sediment bed thickness only uses the centroids (x_p, y_p) of the dots. Because of possible small unevenness at the edges of the dots, the location of the centroids are better determined using a smoothed image. The irregular edges are smoothed via a filter. Figure 2.4 (c), shows the red ellipses[1] that represent the edges of the smoothed dots. For each dot one can measure the following relevant properties using the Matlab function *regionprops*: centroid (x_p, y_p), minor axis, major axis and area in pixel units. As mentioned before, only the centroids are being used during the height calculations. However, the obtained domains from *regionprops* can contain white areas that do not represent projected dots. Via the minor and major axis we remove these white areas. There are several causes for distortion of the dots or additional white areas on the binary image that do not represent projected dots. An overview of these effects is given in section 3.1.2.

When all the correct locations of the projected dots are known, it is important to index each dot. Measuring the shift of a dot in pixel coordinates $\Delta x_p(x_p, y_p) = (x_{pr}, y_{pr}) - (x_{pm}, y_{pm})$ requires the pixel coordinates of projected dots (x_{pr}, y_{pr}) at the reference plane and measured surface (x_{pm}, y_{pm}), hence the additional subscript r and m indicating reference and measurement, respectively. The difference in pixel position only has value when a measured dot is coupled correctly to its corresponding position in the reference measurements. The order of the 200 selected centroids from *regionprops* is rearranged. The function *regionprops* scans the binary image from left to right and from top to bottom. The order in which the dots are found strongly depends on the bed morphology. First, the dots are sorted based on the x_p values. This sorts the pattern column-wise, i.e. 20 groups of 10 dots with comparable x_p values. Each group of 10 dots (column) is now sorted based on their y_p values. The sorting mechanism together with the chosen ΔX and ΔY of the grid provided a suitable indexing technique for the bed morphologies used throughout this project.

---

[1]In Matlab the function *regionprops* finds all the white regions of a binary image and reconstructs ellipses for the edges of these domains. They are called ellipses while they can be approximated as circles.
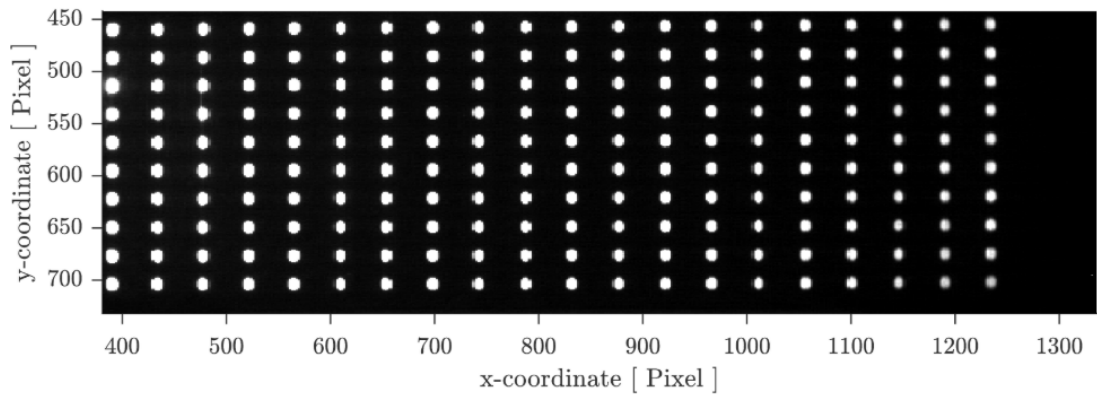
(a)
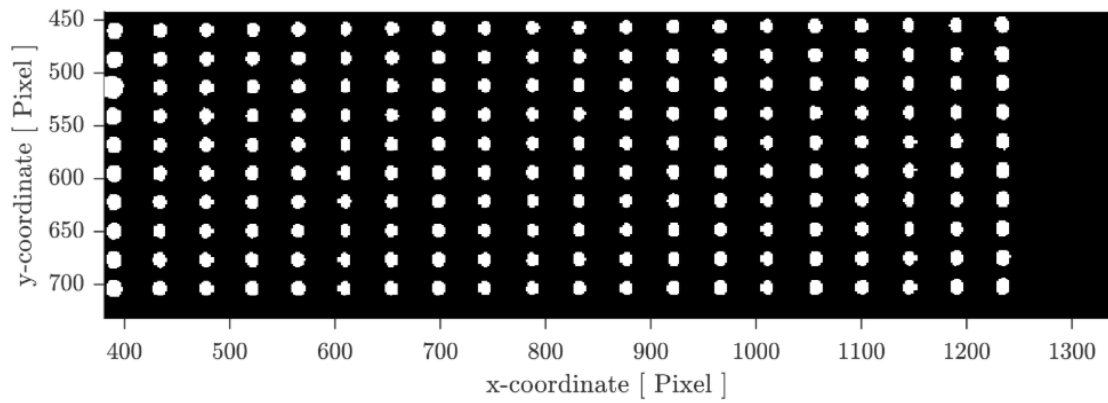
(b)
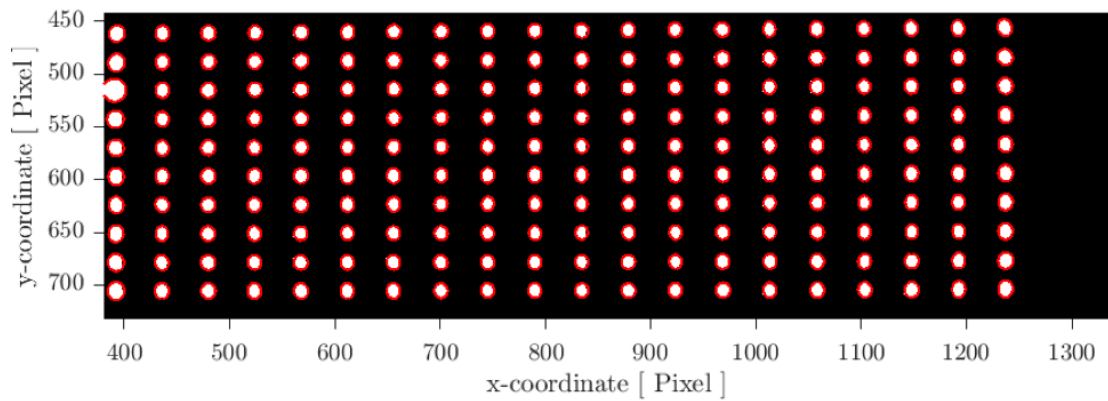
(c)

Figure 2.4: Overview of the image processing. (a) Section of the photograph shown in figure 2.2, where the channel walls on the image are removed. (b) Binary and filtered image of the projection. (c) Obtained ellipses at the edges of all white areas to detect the centroids.

2.2 Pattern matching technique

The first method that is used to measure the sediment bed thickness is the pattern matching technique, inspired by the work of Munro, Dalziel & Jehan (2004), who investigated changes in the sediment bed thickness after a downward travelling vortex ring collided on the bed. The technique is based on the changes in the projected pattern due to variations in height of the sediment. A similar technique was used by De Zwart (2017), who projected a set of dot patterns to study the morphodynamics at a tidal inlet. In current project, this technique is further developed and three versions with a different degree of complexity are presented.
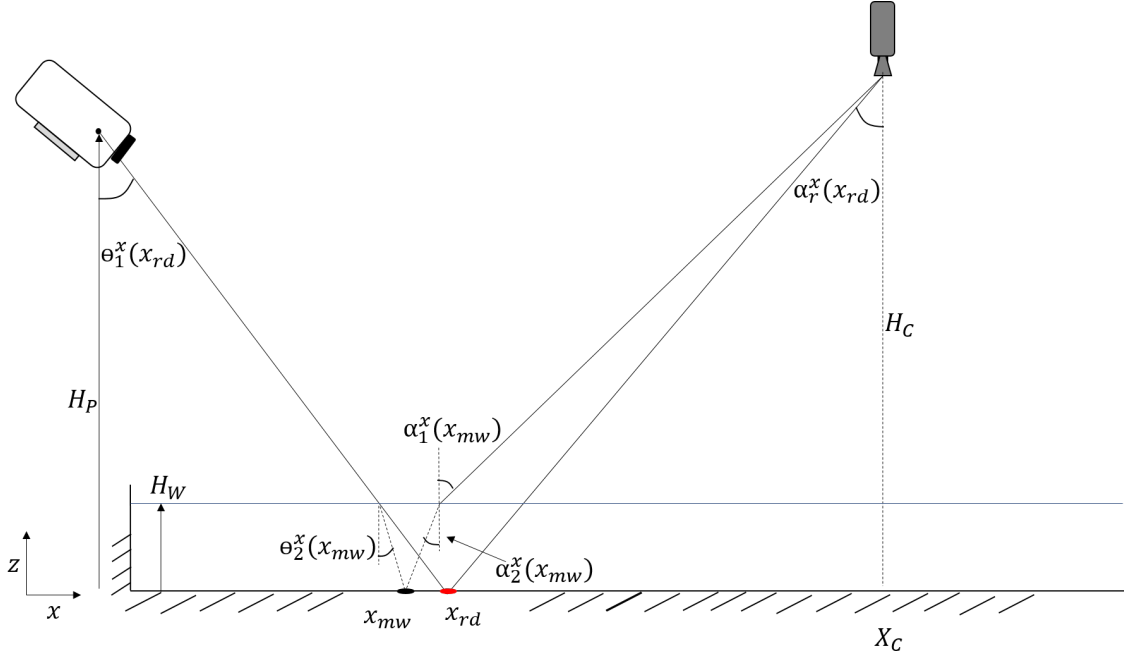
Figure 2.5: Two dimensional schematic representation of the side view of a trajectory of a projected dot on the horizontal bottom. Two different situation are shown where the dot is projected onto the bottom in dry conditions (red dot) and in underwater conditions (black dot). The digital projector and camera are positioned at $(0, H_P)$ and (X_C, H_C), respectively. The refracted light trajectories are represented by dashed lines at $z = H_W$. The angles of the projections are given by $\theta_1^x(x_{rd})$ and $\theta_2^x(x_{mw})$ for dry and underwater conditions, respectively. The angles between the dot and camera are given by $\alpha_r^x(x_{rd})$ and $\alpha_{1,2}^x(x_{mw})$ for dry and underwater conditions, respectively.

2.2.1 Bottom morphology calculation

In this section, a two dimensional description is given for the pattern matching technique and is shown in figure 2.5. The projection angles θ^y along the $y-$axis are small. Therefore, the variations along the $y-$axis are minor. The magnitude of the shifts along x and y can be treated separately. The measured pixel difference $\Delta y_p(x_p, y_p)$, as a result of variations of bottom height, is only used to allocate the y-coordinate of the height measurement correctly. Only the shift along the $x-$coordinate is used to calculate the sediment bed thickness $h(x)$. The digital projector is assumed to be described by a pinhole model, i.e. there is a point where all the dot trajectories intersect: $(0, 0, H_P)$. For the camera, we also use a pinhole model for the point in which all pixel trajectories intersect: (X_C, Y_C, H_C).

The following calculation gives a description for infinitesimally small dots. These dots are assumed to originate from $(0, 0, H_P)$ and are projected under an angle $\theta_1^x(x_{rd})$ onto the bottom

as is shown in figure 2.5. The positions x_{rd} and x_{mw} are the positions of the projected dot at $z = 0$ cm in real world coordinates for dry and underwater measurements, respectively. The dots are then photographed by the camera, where the pixels trajectories are defined by line between the projected on the bed and the point (X_C, Y_C, H_C).

Due to the interface between water and air, light gets refracted and refraction must be taken into account for the projected dots and field of view of the camera. In the remainder of the work, we indicate the measured positions with subscripts d or w, representing dry and underwater conditions, respectively. The reference measurements are performed in dry conditions and are indicated by an additional subscript r, x_{rd}. The underwater morphology measurements are performed with a water level of $z = H_W$ and are indicated by x_{mw}, where the subscript m indicates measurement. For the angles used in this work, we also define two subscripts depending on the media in which the angles are defined. The subscript of an angles is 1 or 2 representing air and water, respectively.

Two different situations are shown in figure 2.5. First, a dry reference measurement is performed where the dots are projected on the bottom plate at $z = 0$ cm, indicated by red dots. The pixel locations of the 3000 dots of the 15 projections are saved as reference centroids (x_{pr}, y_{pr}). Secondly, black dots indicate the position of dots projected through the air-water interface at $z = H_W$. The refracted trajectories under the water surface are indicated by dashed lines.

Via the pinhole model of the digital projector, it is possible to determine $\theta_1^x(x_{rd})$

$$\theta_1^x(x_{rd}) = \arctan\left(\frac{x_{rd}}{H_P}\right), \tag{2.1}$$

where H_P is the height of the digital projector. The camera is positioned vertically at $z = H_C$ above the measurement area at $z = X_C$. The angle $\alpha_r^x(x_{rd})$ represents the angle of the trajectory between the dot and pinhole of the camera with respect to the vertical:

$$\alpha_r^x(x_{rd}) = \arctan\left(\frac{X_C - x_{rd}}{H_C}\right). \tag{2.2}$$

When water is added, both the projected pattern and the field of view of the camera are deformed due to the refraction of light at the air-water interface at $z = H_W$. The angles of the refracted dot and pixel trajectories are given by $\theta_2^x(x_{rd})$ and $\alpha_2^x(x_{rd})$, respectively. Via the law of refraction, we can calculate the angles of refraction:

$$\begin{aligned} n_1 \sin\left(\theta_1^x(x_{rd})\right) &= n_2 \sin\left(\theta_2^x(x_{rd})\right), \\ n_1 \sin\left(\alpha_1^x(x_{rd})\right) &= n_2 \sin\left(\alpha_2^x(x_{rd})\right), \end{aligned} \tag{2.3}$$

where n_1 and n_2 are the refractive indices of air and water, respectively. Two important remarks have to be made before we calculate the angles of incidence at the bottom of the tank in underwater measurements. First, the refracted angle of the dot equals the angle of incidence at the bottom plate: $\theta_2^x(x_{rd}) = \theta_2^x(x_{mw})$. Secondly, the angle of the pixel trajectory at which the reference measurement was captured $\alpha_r^x(x_{rd})$ is not equal to the angle (in air) at which the centroid is captured during underwater measurements $\alpha_1^x(x_{mw})$.

Eliminating the refracted angles from equations (2.3) and substituting them into equations (2.1) and (2.2), we find

$$\theta_2^x(x_{mw}) = \arcsin\left[\frac{n_1}{n_2} \sin\left\{\arctan\left(\frac{x_{rd}}{H_P}\right)\right\}\right], \tag{2.4}$$

$$\alpha_2^x(x_{mw}) = \arcsin\left[\frac{n_1}{n_2} \sin\left\{\arctan\left(\frac{X_C - x_{mw}}{H_C}\right)\right\}\right]. \tag{2.5}$$

In figure 2.6, a two dimensional schematic representation is given for the situation when a dot is projected onto an unknown sediment bed morphology $h(x)$ under water. The water level is given by H_W and the reference location is known and indicated by the red dot x_{rd}.

In the presence of water, one can calculate the magnitude of the horizontal displacement of the
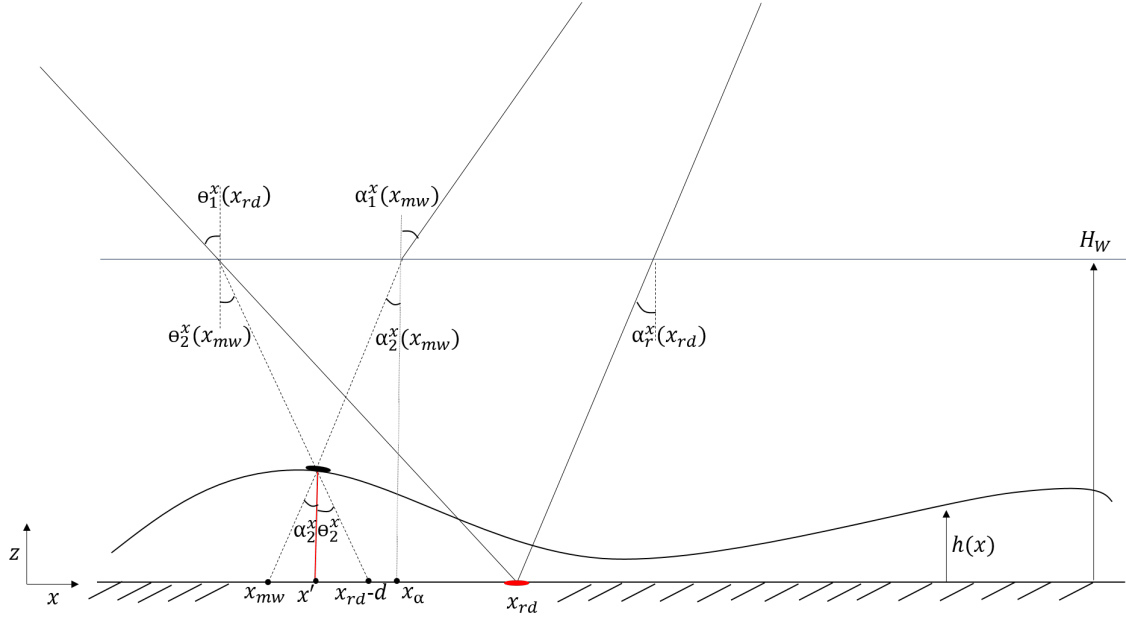
Figure 2.6: Two dimensional schematic representation of the side view of one dot projected in two situations, the dry reference measurement at $z = 0$ cm, and the underwater measurement of a unknown sediment bed morphology $h(x)$. The refracted trajectories are indicated by dashed lines. The reference measurement is indicated by the red dot x_{rd} projected in dry conditions in the absence of sediment. During the measurement of $h(x')$, the dot is refracted at $z = H_W$ and projected onto the sediment bed at x' indicated by the black dot. The position where the dot would have been projected in the absence of sediment is given by $x_{rd} - d$. The trajectory of the pixel at which the centroid of the dot is captured is extended and indicated by x_{mw}. The position at which the pixel trajectory is refracted at the water surface is indicated by x_α.

dot along the $x-$ direction due to refraction. The horizontal displacement of the projected dot is given by $d(x_{rd}, H_W)$ and can be calculated via

$$d(x_{rd}, H_W) = H_W \big[\tan\big(\theta_1^x(x_{rd})\big) - \tan(\theta_2^x(x_{mw})) \big]. \tag{2.6}$$

The position $x_{rd} - d(x_{rd}, H_W)$ can be thought of as an underwater reference positions since it represents the positions of the dot at the bottom of the tank. If the bed morphology changes, the projected dot patterns changes, and these displacements only depend on the height of the sediment.

The height calculation of $h(x')$, indicated by the red line, is given by

$$h(x') = \frac{x_{rd} - d(x_{rd}, H_W) - x'}{\tan\big(\theta_2^x(x_{mw})\big)}, \tag{2.7}$$

where the position of $x_{rd} - d(x_{rd}, H_W)$ and x' are needed in real world coordinates together with the refracted projection angle $\theta_2^x(x_{mw})$. The position x', at which the refracted dot is projected, can be calculated using the following relation

$$h(x') = \frac{x' - x_{mw}}{\tan\big(\alpha_2^x(x_{mw})\big)}, \tag{2.8}$$

so that

$$x' = h(x')\tan\big(\alpha_2^x(x_{mw})\big) + x_{mw}. \tag{2.9}$$

By substituting equation (2.9) into equation (2.20), we find a new expression for the height of the bed

$$h(x') = \frac{x_{rd} - d(x_{rd}, H_W) - x_{mw}}{\tan\left(\theta_2^x(x_{mw})\right) + \tan\left(\alpha_2^x(x_{mw})\right)}. \tag{2.10}$$

The only unknown in this equation is $\alpha_2^x(x_{mw})$, which can be found using x_α, the position at which the pixel trajectory of the captured dot refracts at the water surface:

$$x_\alpha = X_C - (H_C - H_W)\tan\left(\alpha_1^x(x_{mw})\right). \tag{2.11}$$

Using x_α, we can determine $\alpha_2^x(x_{mw})$

$$\alpha_2^x(x_{mw}) = \arctan\left(\frac{x_\alpha - x_{mw}}{H_W}\right), \tag{2.12}$$

$$\alpha_2^x(x_{mw}) = \arctan\left(\frac{X_C - (H_C - H_W)\tan\left(\alpha_1^x(x_{mw})\right) - x_{mw}}{H_W}\right). \tag{2.13}$$

After substituting $\alpha_1^x(x_{mw})$ into equation (2.13) by using the refraction relation, we find the following condition for $\alpha_2^x(x_{mw})$

$$\alpha_2^x(x_{mw}) = \arctan\left(\frac{X_C - (H_C - H_W)\tan\left(\arcsin\left\{\frac{n_2}{n_1}\sin\left[\alpha_2^x(x_{xm})\right]\right\}\right) - x_{mw}}{H_W}\right). \tag{2.14}$$

This equation can not be solved analytically and has to be solved numerically.

Three dimensional measurement area

The height calculations are performed in a two dimensional plane, using only the displacement of the dots in the $x-$direction. However, the allocation of the measured height is three dimensional (x, y, z). Because the angle of projection varies in the $y-$direction, we have to include $\theta_1^y(x_{rd}, y_{rd})$ and $\alpha_1^y(x_{rd}, y_{rd})$, to correctly calculate the $y-$coordinate of the measured height. Figure 2.7 gives a three dimensional schematic representation of the projected measurement area in real world coordinates for dry conditions. The transparent red lines represent the trajectories of the projected dots at the corners of the measurement area. They form an obtuse pyramid with apex $(0, 0, H_P)$ and base at $z = 0$ cm. The projection angle in the $x-$ and $y-$directions are given by $\theta_1^x(x_{rd}, y_{rd})$ and $\theta_1^y(x_{rd}, y_{rd})$, respectively:

$$\theta_1^x(x_{rd}, y_{rd}) = \arctan\left(\frac{x_{rd}}{H_P}\right), \tag{2.15}$$

$$\theta_1^y(x_{rd}, y_{rd}) = \arctan\left(\frac{y_{rd}}{H_P}\right). \tag{2.16}$$

Note the independence of y in $\theta_1^x(x_{rd}, y_{rd})$ along the $y-$axis: $\theta_1^x(x_{rd}, y_{rd}) \to \theta_1^x(x_{rd})$. The same hold for x and the angle in the (x, y) plane, $\theta_1^y(x_{rd}, y_{rd}) \to \theta_1^y(y_{rd})$. For the $y-$direction in underwater measurements, we calculate the refracted angle $\theta_2^y(y_{rd})$, which is equal to the angle of incidence $\theta_2^y(y_{mw})$ at the measured bed using equation (2.3). When both angles are known, we calculate the shift $d(y_{rd}, H_W)$ similar to equation (2.6). The position of the projected dot at the sediment bed can finally be calculated via

$$(x, y, z) = \begin{cases} x = x_{rd} - d(x_{rd}, H_W) - h(x') \tan\left(\theta_2^x(x_{mw})\right) \\ y = y_{rd} - d(y_{rd}, H_W) - h(x') \tan\left(\theta_2^y(y_{mw})\right) \\ z = h(x'). \end{cases} \tag{2.17}$$
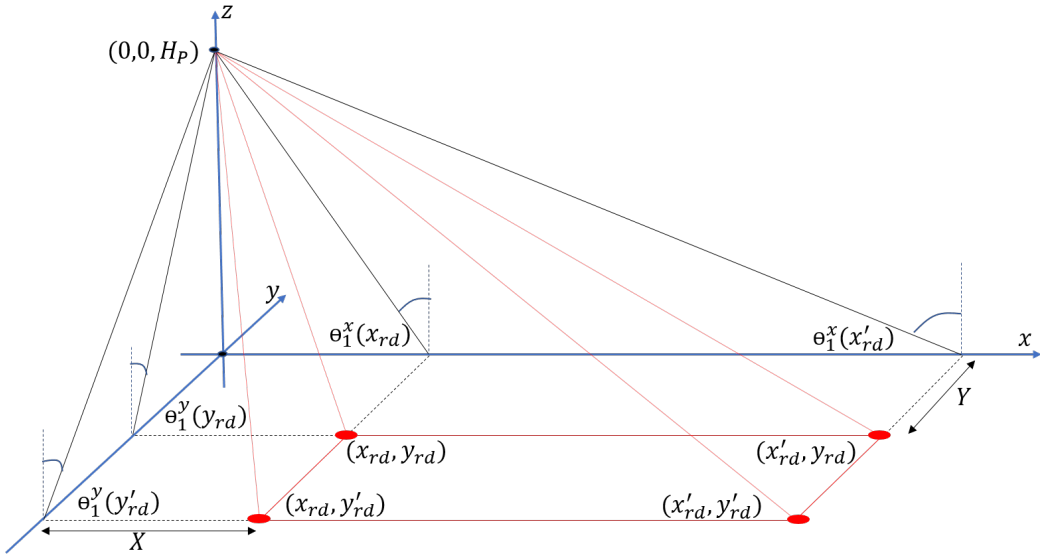
Figure 2.7: Schematic representation of the measurement area defined by the outer projections (four red dots) of the projected dot patterns at $z = 0$ cm. The pinhole of the digital projector at $(0, 0, H_P)$ defines the origin of the coordinate system. The projected dot trajectories are indicated by transparent red lines that are mathematically projected onto the (x, z) and (y, z) planes, indicated by black lines. The angles that these black lines make with the $(x, y, 0)$ plane are indicated by the four angles $\theta_1^{x,y}$.

2.2.2 Approximations of the pattern matching technique

The final version of the height calculation, equation (2.10), is the result of a series of improvements on the measurement technique of De Zwart (2017). The implementation of his height calculations, provided incorrect reconstructions of the bed morphology in the current project. We found that under different conditions, approximations of equation (2.10) can be made that provide accurate reconstructions of the sediment bed thickness. In the following, we present the basic principle of two dimensional height calculations under different assumptions. The first version describes the pattern matching technique for a situation where variations in the angle of projection are small. Furthermore, the variations in the angles at which the dots are captured are also small. Therefore, the angle of projection, and angle with the camera, are described by the constants, θ and α, respectively. However, the magnitudes of θ and α are not measured, and a general calibration factor $C_{1,2}$ is used to perform the height calculations, where 1 and 2 indicate dry and underwater measurements, respectively.

For the second version of the pattern matching technique, we include the variations in the projection angle $\theta(x)$ over the region of interest. However, the effect of the angle under which the projection is photographed is still not included and $\alpha = 0°$.
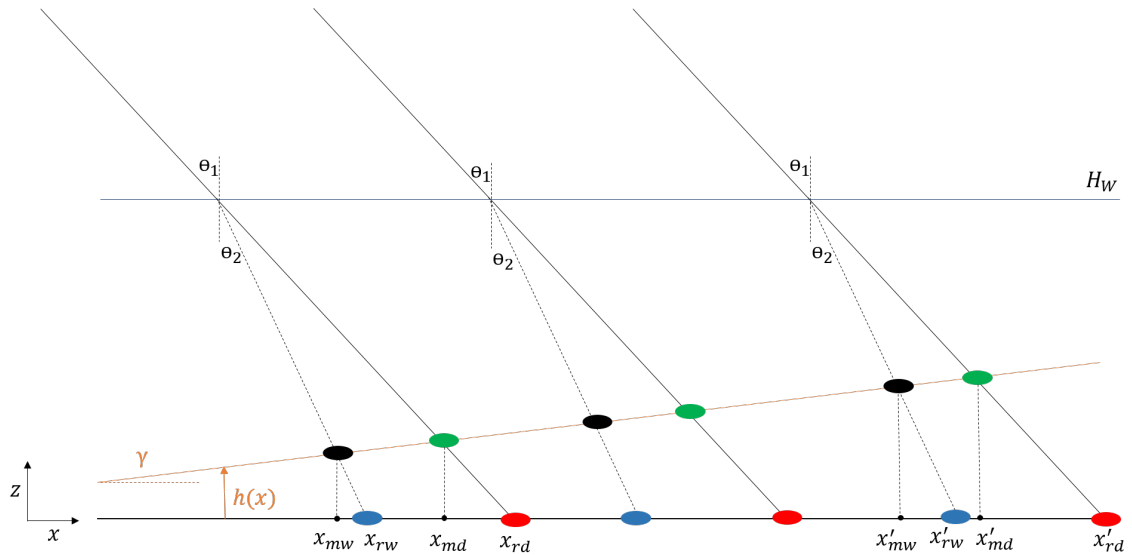
Figure 2.8: Two dimensional schematic representation of the side view of the calibration of the vertical factors $C_{1,2}$ for dry and underwater conditions, respectively. For three projected dots four possible positions are indicated. The red dots represent the reference measurement in dry conditions x_{rd}. The green dots indicate the locations of the projection x_{md} on the inclined plate indicated by the brown line $h(x)$ with angle angle γ. In the underwater calibration, where the water surface height is indicated by $z = H_W$, the dot patterns are refracted and indicated by the dashed lines. The underwater reference locations are given by the blue dots x_{rw}. The black dots x_{mw} indicate the measured positions of projected dots onto the inclined plate underwater.

Pattern matching technique, version I

The measurement technique used by De Zwart (2017), represents the first version of the pattern matching technique of this work. A constant vertical factor $C_{1,2}$ [cm/pixel] is used to calculate the bottom morphology $h(x)$ [cm], where the subscript 1 and 2 indicate dry and underwater conditions, respectively. A shift in the $x-$position of the centroid of a projected dot in the image $\Delta x_p(x,y)$ [pixel] is multiplied by a constant factor $C_{1,2}$. This then calculates the height in real world coordinates, i.e. $h(x) = C_{1,2} \cdot \Delta x_p(x_p, y_p)$. Therefore, in dry conditions a movement of 1 pixel corresponds to a vertical change of C_1 cm.

The constant vertical factors $C_{1,2}$ are determined via two calibration measurements. A two dimensional schematic representation is given in figure 2.8, where three projected dots are represented at four possible locations. A rigid metal plate is positioned under an angle γ, indicated by the brown line $h(x)$. The dry calibration is indicated by the red and green dots. The red dots represent the reference measurement, and are labelled x_{rd} and x'_{rd}. The green dots represent the locations of the projections on the inclined plate $\big(x_{md}, h(x_{md})\big)$ and $\big(x'_{md}, h(x'_{md})\big)$. The shift in the pixel locations $\Delta x_p(x_p, y_p)$, is measured on the image for each dot. In real world coordinates these corresponding differences are given by $x_{rd} - x_{md}$ and $x'_{rd} - x'_{md}$.

The angle of the calibration plane is $\gamma = \arcsin(\frac{\Delta h}{\Delta x})$, where $\Delta h = h'(x'_{md}) - h(x_{md})$ is the height difference over the measurement area, and $\Delta x = x'_{md} - x_{md}$ the distance between the projected dots of the outer columns. Using $h(x) = \sin(\gamma) \cdot x + h_0$, we can calculate the (averaged) vertical factor

$$C = \frac{h(x)}{\Delta x_p(x_p, y_p)}. \tag{2.18}$$

The projections in underwater measurements, with a water level at $z = H_W$, are deformed by refraction. The refracted positions of the dots on the inclined plate are represented by the black dots at x_{mw} and x'_{mw}, shown in figure 2.8. The corresponding refracted dot trajectories are indicated by the dashed lines under a constant angle θ_2. The same calculations for the (averaged) vertical factor can be made to find the factor C_2 for underwater measurements.

The first version of the height calculation is then given by

$$h(x_{md}) = C_1 \cdot \Delta x_p(x_{p1}, y_{p1}) = \frac{x_{rd} - x_{md}}{\tan(\theta_1)}, \tag{2.19}$$

$$h(x_{mw}) = C_2 \cdot \Delta x_p(x_{p2}, y_{p2}) = \frac{x_{rw} - x_{mw}}{\tan(\theta_2)}, \tag{2.20}$$

where (x_p, y_{p1}) and (x_{p2}, y_{p2}) represent the obtained pixel coordinates of the centroids in dry and underwater conditions. Using equation (2.10), we can find $C_1 \sim \frac{1}{\tan(\theta_1)}$ for dry, and $C_2 \sim \frac{1}{\tan(\theta_2)}$ for underwater conditions. The final result of the approximation on equation (2.17) is then given by

$$(x, y, z) = \big(x_{mw}, y_{mw}, h(x_m)\big). \tag{2.21}$$

Pattern matching technique, version II

In our setup we have an increasing angle of incidence along the x-coordinate: $26° < \theta_1^x(x_{rd}) < 42°$. [2] The assumption of a constant projection angle θ does no longer hold and we include this variation $\theta \to \theta_{1,2}^{x,y}(x,y)$ into the height calculation of $h(x)$. Moreover, the second version of the height calculation uses the positions of only dry reference measurements. For underwater measurements, we have to calculate the shift in dot position, due to the refraction of the projections at the water surface. This shift is given by $d(x_{rd}, H_W) = x_{rd} - x_{rw}$ and depends on the water level H_W.[3]

The two dimensional representation of the first version (figure 2.8) is adjusted to account for the change in projection angle as shown in figure 2.9. The calculation of the projection angles $\theta_1^x(x_{rd})$ is similar to equation (2.15) where the refracted angle $\theta_2^x(x_{rd})$ is calculated using equation (2.3). The corresponding shift in dot position $d(x_{rd}, H_W)$ for underwater measurements with a water level of $z = H_W$ is then given by equation (2.6). The new height calculation is given by

$$h(x_{mw}) = \frac{x_{rw} - x_{mw}}{\tan\left(\theta_2^x(x_{mw})\right)} = \frac{x_{rd} - d(x_{rd}, H_W) - x_{mw}}{\tan\left(\theta_2^x(x_{mw})\right)}. \tag{2.22}$$

Note the resemblance with equation (2.10), exept for the fact that the angle to the camera is not included. The measured position is then defined by

$$(x, y, z) = \left(x_{mw}, y_{mw}, h(x_{mw})\right). \tag{2.23}$$
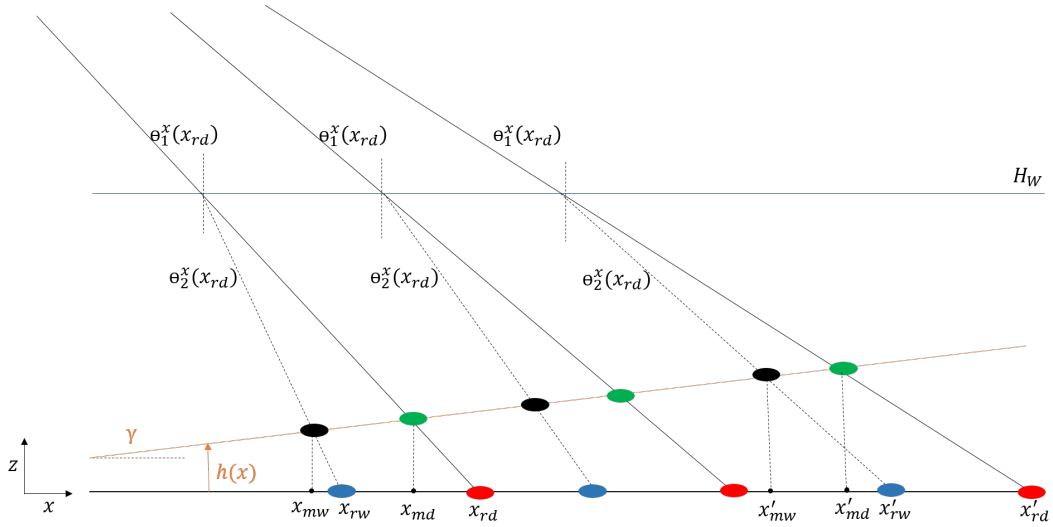
Figure 2.9: Two dimensional schematic representation of the side view (x,z)-plane of the measurement of a inclined plate. For three projected dots, four possible positions are indicated whose $x-$coordinate is labelled. The red dots represent the reference measurement in dry conditions. The green dots indicate the locations of the projection x_{md} on the inclined plate $h(x)$ positioned under an angle γ. For underwater measurements $z = H_W$, the projections get refracted $\theta_1^x(x_{rd}) \to \theta_2^x(x_{rd})$. The new positions of the dots projected onto the plane are indicated by black dots x_{mw}.

---

[2]The change in the angle of incidence for one single dot is small and does not violate the assumption of the description of a point. Using equation (2.1) and the diameter of the dot d_{dot}, only a maximum change of $\Delta\theta = 0.12°$ over one dot is found at the end of the channel.

[3]Because d depends on H_W, we calculated this shift. This removes the need to perform (new) reference measurements for each water level. Via only one dry reference measurement, we can now include the shift in positions due to refraction for any given H_W.

2.2.3 Pixel coordinates to real-world coordinates

The height calculation in equation (2.10), requires the physical locations of the projected dots x_{rd} and x_{mw}. In the two dimensional representation of figure 2.6, the measured position is given by the dashed black line of $\alpha_2^x(x_{mw})$, not representing a single position but a collection of possible points on this pixel trajectory. On the photograph, the pixel position (x_p, y_p) represents both $(x_{mw}, 0)$ and (x', h). However, the conversion from pixel to real world coordinates is done at $z = 0$ cm. Therefore, only the real world coordinates of $(x_{mw}, 0)$ can be calculated from the images since h is unknown and the transformation function depends on the height.

Calibration

The horizontal bottom plate at $z = 0$ cm is used to calibrate the camera and obtain the relation between pixel coordinates (x_p, y_p) and real world coordinates $(x, y, 0)$ in dry conditions. By measuring the physical dimensions of different projections on the bottom of the tank [cm] together with the dimensions on the photograph [pixel], a calibration factor of $Pix2Cm(z = 0) = 0.073$ cm/pixel is found along both $x-$ and $y-$direction. Therefore, the relation between pixel and real world coordinates inside the measurement area at $z = 0$ cm is given by

$$(x_p, y_p) \cdot Pix2Cm(z = 0) = (x, y, 0). \tag{2.24}$$

A rectangular object or projection of dimensions 10 cm $\times$ 10 cm at $z = 0$ cm, will thus be captured within a window of $\frac{10}{0.073} \times \frac{10}{0.073} = 137$ pixels $\times$ 137 pixels.

The value of this calibration factor depends on the distance between the camera and the plane of interest. Note that the horizontal plane and normal of the camera are perpendicular, as is shown in figure 2.10. Due to the vertical positioning of the camera, and little to no deformations found in the images, a constant calibration factor is a good approximation for the relation between pixel and real world coordinates inside the measurement area.[4]

In the dry test measurements of horizontal plates at different heights, we found the importance of the magnification effect, i.e. the seemingly increasing dimensions of an object when it is photographed closer to the camera, shown in figure 2.10. The points (x, y, z) and (x, y, z') are captured under an angle $\alpha_1^x(x(z))$ and $\alpha_1^x(x(z'))$, respectively. The horizontal dimensions are the same but because $\alpha_1^x(x(z)) < \alpha_1^x(x(z'))$, the photographed object is magnified. Since the sediment level is variable and calibration measurements are performed at different heights, it is important to take this effect into account. Additional calibration measurements are performed for a horizontal plane positioned at $z = 9.5$ cm and $z = 32$ cm. We have marked four points on the plate, at the corners of the measurement domain at $z = 0$ cm. By measuring the physical distance and the distance between these corner points on the images. We find the new relation between real world coordinates and pixels. For the plane at the heights $z = 9.5$ cm and $z = 32$ cm, we found calibration factors of 0.0677 cm/pixel and 0.0588 cm/pixel, respectively. The goal here was to find the relation between the vertical z and the transformation of pixel coordinates to real world coordinates, that is finally given by

$$Pix2Cm(z) = \frac{0.0588 - 0.0677}{32.0 - 9.5} \cdot z + Pix2Cm(0) = -3.955 \times 10^{-4} \cdot z + Pix2Cm(0). \tag{2.25}$$

A control measurement at $z = 21.9$ cm, shows that a linear relation correctly predicts the $Pix2Cm(z)$ factor. The measured $Pix2Cm$ factor of 0.0619 cm/pixel is in agreement with equation (2.25): $Pix2Cm(21.9) = 0.0613$ cm/pixel. For the morphological measurements, only small variations in the vertical are present $0 < h < 4$ cm. The heights here are only used to validate the linear relation. The goal was to use equation (2.25), to transform the measured (x_p, y_p) into (x', y'). Later, we found that the actual measured position was given by $(x_{mw}, y_{mw}, 0)$. Moreover, the $Pix2Cm(z)$ is obtained in dry conditions. For images of underwater measurements, we can

---

[4]A rectangular object at $z = 0$ cm is also captured by a rectangle on the image. The maximum curvature/bending in the edges of the photographed rectangle is 3 pixels.

not use this relation, because of refraction in the field of view of the camera. However, in this project we did not implement this effect, since the final pattern matching technique is only used to measure in dry conditions. In the two approximations of the pattern matching technique, we did make the (double) incorrect assumption that $(x_p, y_p) \cdot Pix2Cm(z = 0) = \big(x', y', h(x')\big)$ for underwater conditions. However, we included the following correction for dry test measurements.

In the calibration measurements, we found that the position of a measured dot varies under changing heights. This shift in pixel coordinates due to the magnification is included, see figure 2.10. The figure shows an object that is photographed at height z and z'. The position of the physical object only differs in the vertical coordinate. However, in pixel coordinates two shifts $\Delta x_p(x_p, y_p)$ and $\Delta y_p(x_p, y_p)$ will be measured

$$\Delta x(x, y) = \Delta H \tan\big(\alpha_1^x(x, y)\big), \qquad (2.26)$$

and

$$\Delta y(x, y) = \Delta H \tan\big(\alpha_1^y(x, y)\big), \qquad (2.27)$$

where $\Delta H = z' - z$ is the difference in height and α_1^x the angle with respect to the centre line of the camera. Unfortunately, it is not possible to implement these effects for morphological measurements since the height of the bed is needed to adjust the coordinates. The effect is given here because in the test measurements of horizontal planes, we can measure the height and the effect was implemented.
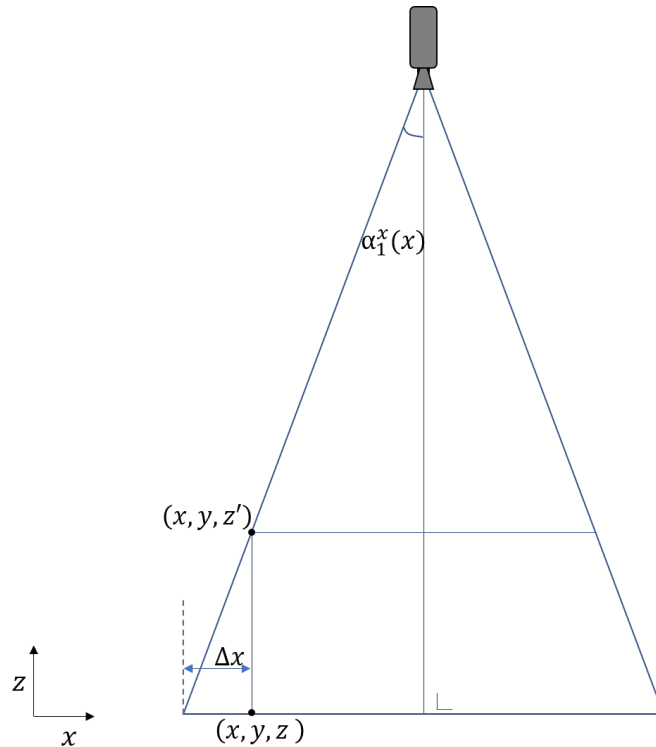
Figure 2.10: Schematic representation of the magnification effect between z and z' in dry conditions. A point that is photographed at (x, y, z) will have different pixel coordinates than a point positioned at (x, y, z'). Since only the vertical position changes, there should be no shift in the obtained horizontal real world coordinates. However, current $Pix2Cm(z)$ will incorrectly include two shifts of $\Delta x(x, y)$ and $\Delta y(x, y)$, that are corrected for when the height difference is known.

2.3 Photogrammetric technique

Photogrammetry is the science of making measurements from photographs, especially for recovering the exact positions of surface points. In current project, we use a photogrammetric technique to measure the bed morphology underneath an oscillating flow of water. When a dot is projected onto the sediment and captured by the camera, one can find the light trajectories from the projector to the illuminated dot and from the centroid of the dot to the camera. In the remainder of this work we use dot trajectory and pixel trajectory to indicate these light trajectories. These two trajectories intersect at the surface onto which the dot is projected. By calibrating the camera and the digital projector, it is possible to determine the dot and pixel trajectories in real world coordinates. We define the trajectories by vectors $(x_P, y_P, z_P, dx_P, dy_P, dz_P)$ and $(x_c, y_c, z_c, dx_c, dy_c, dz_c)$, where the indices P and c stand for projector and camera respectively.[5] The intersection is represented by the real world coordinate (x, y, h). The technique is capable of measuring the sediment bed thickness without removing the water in the setup. Because there is a water layer on top of the sediment bed, light is refracted at the interface between the two media. Via dry calibrations, of the digital projector and the field of view of the camera, and a three dimensional calculation of Snells law, we can correctly implement the refraction of both trajectories. By calculating the point of intersection, we find the height of the sediment bed. Because the technique can be implemented in different ways, a more general description is given here.

2.3.1 Calibration of Camera and Projections

Calibration measurements are performed to determine both sets of trajectories: the projected dot trajectory $(x_P, y_P, z_P, dx_P, dy_P, dz_P)$ representing the physical light ray of the centroid of the projected dot, and the pixel trajectory $(x_c, y_c, z_c, dx_c, dy_c, dz_c)$ representing the physical line in space that is captured by one single pixel. The camera is calibrated before the digital projector because the digital projector calibration is done with the calibrated camera. Both calibrations are performed in the absence of water. The refraction at the water surface is later included via a three dimensional calculation of Snells law. For the dot trajectories, 3000 fixed trajectories have to be determined since each dot is projected via a specific and constant trajectory throughout this project. For the camera, we find each pixel trajectory in the field of view of the camera using a third order polynomial fit.

Camera

The calibration of the camera is performed by photographing a PIV calibration plate at different heights. The calibration plate consists of a rectangular grid of 23×23 white dots with a diameter of 0.50 cm, and a separation of 2.50 cm from center to center. In figures 2.11 (a) and (b), images are shown of the calibration plate at two different heights: $z = 12.99$ cm and $z = 23.93$ cm. The height of the calibration plate is changed without changing the horizontal coordinates (x, y).

---

[5]Note that for the projector a capital P is used since the index p is already used to indicate pixel coordinates.
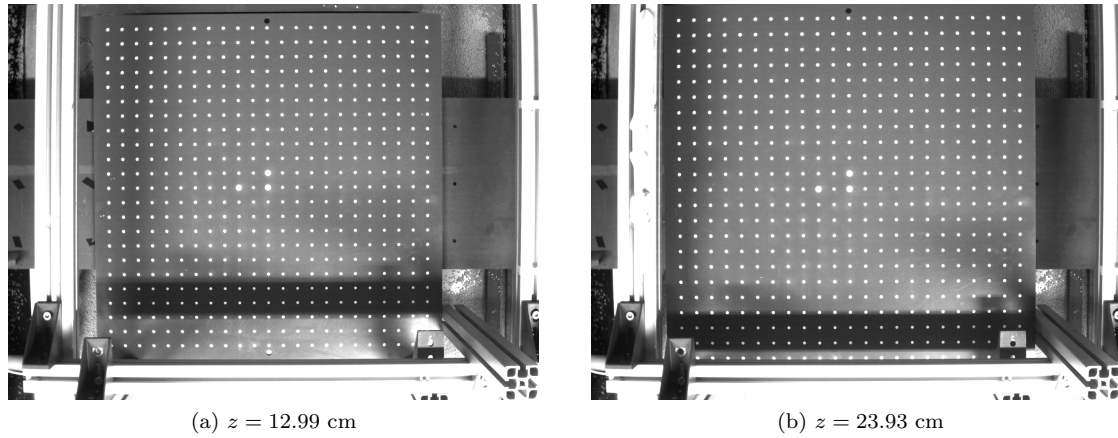
(a) $z = 12.99$ cm

(b) $z = 23.93$ cm

Figure 2.11: Photographs of the PIV calibration plate at two different heights. The plate consists of a 23×23 grid of white dots with a diameter of 0.50 cm, that have a separation of 2.50 cm from center to center. The plate is positioned horizontally against vertical barriers. One barrier is shown in the bottom right corner in both photographs.
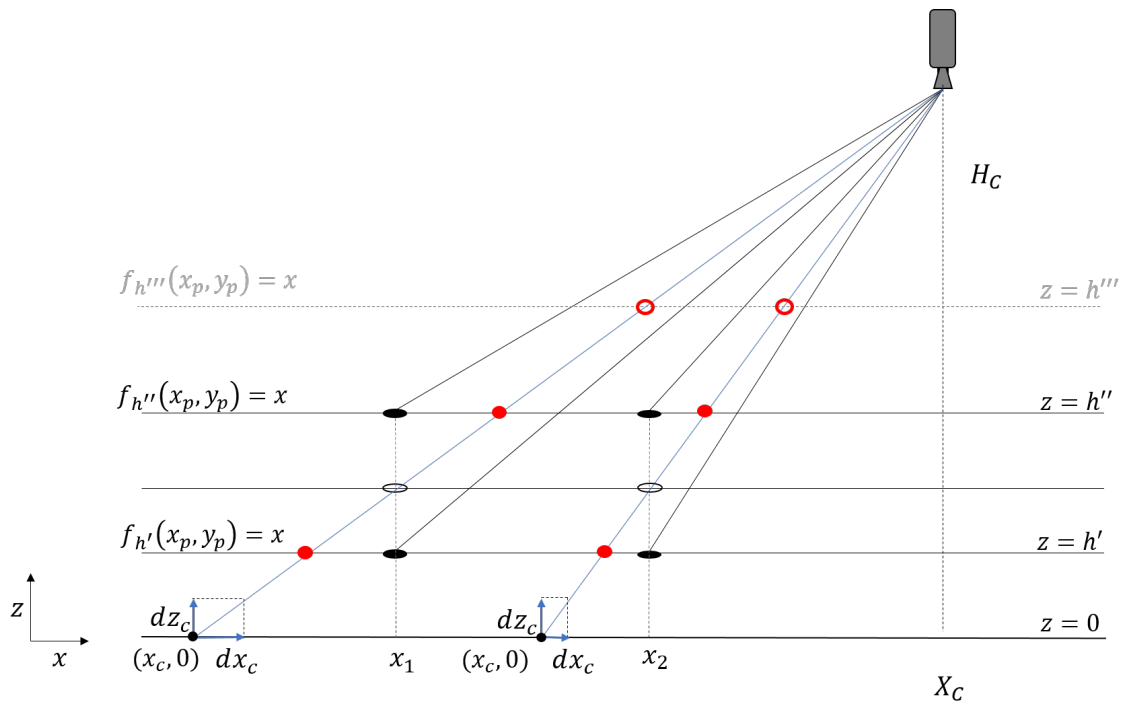
Figure 2.12: Two dimensional schematic representation of the camera calibration. The PIV calibration plane is positioned at $z = h'$ and $z = h''$. Two points of the plane x_1 and x_2 are indicated by solid black ellipses, the corresponding pixel trajectories are represented by the black lines between the points and the pinhole of the camera (X_C, H_C). An arbitrary calibration point/pixel grid is defined and is represented by the blue lines and open black ellipses at $h' < z < h''$. The real world locations where these pixel trajectories intersect the calibration heights h' and h'' are indicated by solid red dots. Via the functions $f_{h'}(x_p, y_p)$ and $f_{h''}(x_p, y_p)$ one can calculate the real world locations at the heights h' and h'' for this arbitrary set of points/pixels. These coordinates, indicated by red dots, are then used to construct the pixel trajectory and are defied by a vector having its origin at $(x_c, z_c = 0$ cm$)$ and magnitudes $(dx_c, dz_c = 1$ cm$)$. The horizontal dashed gray line represents an additional calibration height h'''.

The position of the dots on the calibration plate only differ in the $z-$coordinate in real world coordinates. However, due to the magnification effect, different positions are found for the pixel coordinates for the dots on the plate at the different heights. A relation can be found between the pixel coordinates and the real world coordinates. These relations depend on the height of the plate and convert pixel coordinates (x_p, y_p) into real world coordinates (x, y, h). The relations are obtained via a third order polynomial fit and are given by $f_z(x_p, y_p)$ and $g_z(x_p, y_p)$

$$
\begin{aligned}
x &= f_z(x_p, y_p) \\
&= a_0^z + a_1^z x_p + a_2^z y_p + a_3^z x_p y_p + a_4^z x_p^2 + a_5^z y_p^2 + a_6^z x_p^3 + a_7^z x_p^2 y_p + a_8^z y_p^3 + a_9^z x_p y_p^2, \quad (2.28) \\
y &= g_z(x_p, y_p) \\
&= b_0^z + b_1^z x_p + b_2^z y_p + b_3^z x_p y_p + b_4^z x_p^2 + b_5^z y_p^2 + b_6^z x_p^3 + b_7^z x_p^2 y_p + b_8^z y_p^3 + b_9^z x_p y_p^2, \quad (2.29)
\end{aligned}
$$

where a_i^z and b_i^z are the polynomial coefficients determined with the Matlab fit function. The physical locations of the 23×23 dots are known, and via the fitting, one finds the set of coefficients that relate each pixel coordinates to the physical coordinates at $z = h$. A fourth order polynomial fit did not improve the calibration since the coefficients of higher order terms a_i and b_i with $i > 10$ are negligible. Therefore, a third order polynomial is used throughout this project. These polynomial fits describe the transformation from pixel to real world coordinates more accurately than the calibrations discussed in section 2.2.3. The factor $Pix2Cm(z)$, is an approximation and obtained from only four points at the outer points of the measurement area, whereas this calibration captures and uses 23×23 points inside the measurement area. This new calibration of the field of view of the camera is more accurate and contains effects such as lens deformations, rotation or tilt of the camera and even rotation or tilt of the internal CCD. These effects are small since the coefficients of the higher order terms are small but are anyway included using current calibration method.

In figure 2.12, a two dimensional schematic representation of the camera calibration is shown in real world coordinates. The two calibration plates are positioned at heights $z = h'$ and $z = h''$, where the relations from pixel to real world coordinates are determined using equations (2.28) and (2.29). They are indicated by $f_{h'}(x_p, y_p)$ and $f_{h''}(x_p, y_p)$, respectively. Two arbitrary white dots of the calibration plate are indicated by solid black ellipses whose positions in real world coordinates only differ in the vertical.

The next step is to calibrate a number of pixel trajectories, i.e. to construct a set of pixel trajectories in real world coordinates, indicated by the blue lines in figure 2.12. This set of pixel trajectories is then converted into a set of vectors. Any arbitrary set of pixels that covers the measurement area uniformly can be used. In the following, a 23×23 grid of points is defined for which the pixel trajectories will be calculated. When this set of pixel trajectories is calculated, a third order polynomial fit is made that describes all the pixel trajectories of the pixels inside the calibrated region. The set of calibrated pixels can be treated as if it is a photographed calibration grid at an unknown height, indicated by open black ellipses at $h' < z < h''$. The two pixels trajectories that correspond to this calibration plate are shown by the blue lines and indeed intersect the virtual dots on the arbitrary calibration plate indicated by black ellipses.

From the set of pixels that are being calibrated, we calculate the corresponding real world coordinates at the two known calibration heights, i.e. $h' = 12.99$ cm and $h'' = 23.93$ cm, indicated by the red dots in figure 2.12. At these two heights, we can use the pixel to real world functions previously defined by equations (2.28) and (2.29). Both coordinates (x', y', h') and (x'', y'', h'') intersect with the corresponding pixel trajectory in real world coordinates, i.e. the blue lines. The trajectory of this (blue) pixel is calculated using the two points (solid red dots) in real world coordinates and will be represented by a vector. The origin of this vector is chosen at the bottom of the setup (x_c, y_c, z_c) where $z_c = 0$ cm. This vector is composed of the three components, normalized along the vertical, $dz_c = 1$ cm. The magnitude in x and y directions are given by dx_c and dy_c, respectively. For each pixel in the arbitrary grid, we now have six variables $(x_c, y_c, z_c, dx_c, dy_c, dz_c)$ where z_{c0} and dz_c are known constants by definition. The final step is to find the global vector fitting all pixel trajectories. The fit relates each pixel coordinates on the

image to a set of six variables representing the vector variables that describe the pixel trajectory.

$$
\begin{aligned}
x_c &= f_{z=0}(x_p, y_p) \\
&= a_0 + a_1 x_p + a_2 y_p + a_3 x_p y_p + a_4 x_p^2 + a_5 y_p^2 + a_6 x_p^3 + a_7 x_p^2 y_p + a_8 y_p^3 + a_9 x_p y_p^2, \qquad (2.30) \\
y_c &= g_{z=0}(x_p, y_p) \\
&= b_0 + b_1 x_p + b_2 y_p + b_3 x_p y_p + b_4 x_p^2 + b_5 y_p^2 + b_6 x_p^3 + b_7 x_p^2 y_p + b_8 y_p^3 + b_9 x_p y_p^2, \qquad (2.31) \\
z_c &= 0 \text{ cm} \\
dx_c &= c_0 + c_1 x_p + c_2 y_p + c_3 x_p y_p + c_4 x_p^2 + c_5 y_p^2 + c_6 x_p^3 + c_7 x_p^2 y_p + c_8 y_p^3 + c_9 x_p y_p^2, \qquad (2.32) \\
dy_c &= d_0 + d_1 x_p + d_2 y_p + d_3 x_p y_p + d_4 x_p^2 + d_5 y_p^2 + d_6 x_p^3 + d_7 x_p^2 y_p + d_8 y_p^3 + d_9 x_p y_p^2, \qquad (2.33) \\
dz_c &= 1 \text{ cm}
\end{aligned}
$$

where the coefficients are determined with the Matlab *fit* function. The chosen 'arbitrary' grid of 23×23 points was sufficient to find the global fit for all pixel trajectories.

If the number of points on the calibration plate is not large enough, an incorrect fit of the relations f_z and g_z is found. Since the final fit of all pixel trajectories, equations (2.30) to (2.33) depend on the accuracy of the relations f_z and g_z, and the number of calibration heights h, two tests are performed where the number of points is doubled. Secondly, more calibration heights are used, to construct the trajectories using linear regression.

Increasing the number of points on the calibration plate is not possible. However, the vertical barriers against which the calibration plate is positioned, can be moved to a different positions to find new fits of f_z and g_z for the same z value, i.e. equations (2.28) and (2.29). Since the heights at which the plate is positioned are identical to the first camera calibration measurements, both sets of 23×23 can be combined into a set of 46×46, from which new fits for $f_{h'}$, $f_{h''}$, $g_{h'}$ and $g_{h''}$ can be found. The differences between the coefficients from the first and new calibrations are negligible, and the first set of coefficients is chosen, using only 23×23 points.

Additional calibration measurements, where the PIV calibration plate is positioned at new heights can be added for which new relations of $f_z(x_p, y_p)$ and $g_z(x_p, y_p)$ are determined. In figure 2.12, the gray line represents the new height h''' at which $f_{h'''}(x_p, y_p)$ and $g_{h'''}(x_p, y_p)$ are calculated. Next, we use the same set of 'arbitrary' pixels to calculate their trajectories in real world coordinates. By introducing the additional set of coordinates (red circles) at h''', linear regression has to be implemented, since the three coordinates will not perfectly exist on one straight line. The least squares approach is chosen to determine the best fit of the pixel trajectory trough the different levels. In figures 2.13 and 2.14, the obtained pixel trajectories are shown from a set of four different height $z = 12.99, 17.49, 21.99$ and 23.93 cm. The obtained pixel trajectories correctly intersect in a small region in space at $H_C = 179.5$ cm, and pass trough each of the calculated positions. Note that the calibration here is given in millimeters and that the coordinate system is defined by the centre of the PIV calibration plane. In the measurements, we use a translated coordinate system where the position of the digital projector is set to $(0, 0, H_P)$, to match the height calculations of the pattern matching technique.
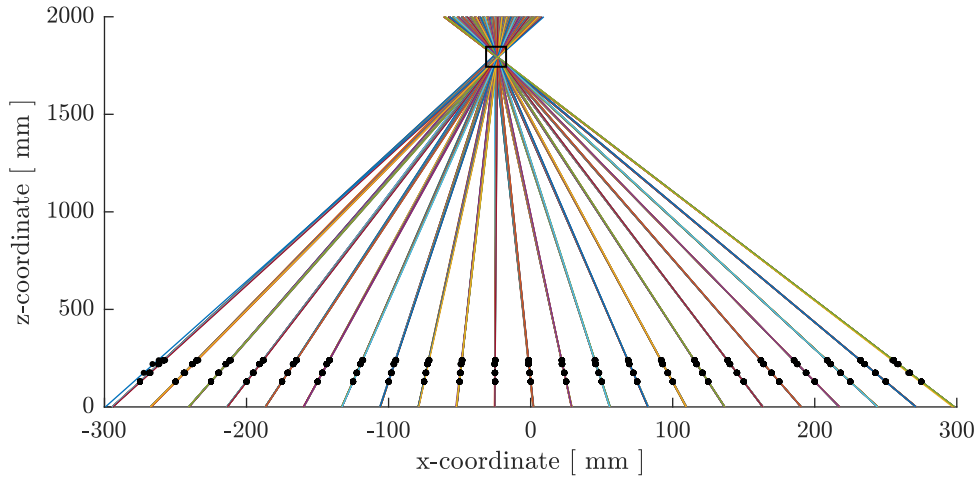
Figure 2.13: Side view of the calibration of the camera. The PIV plane is positioned at four different heights $z = 12.99, 17.49, 21.99$ and 23.93 cm, from which the four corresponding transformation fits of $f_z(x_p, y_p)$ and $g_z(x_p, y_p)$ are determined. The 23×23 set of points is then used to calculate the corresponding positions on the four heights, indicated by black dots. Via the least square method, we calculate the trajectories and the corresponding vector $(x_c, y_c, z_c = 0$ cm, $dx_c, dy_c, dz_c = 1$ cm). The position of the camera in this coordinate system is $(X_C = -24.32$ mm, $Y_C = -37.45$ mm, $H_C = 1795$ mm).
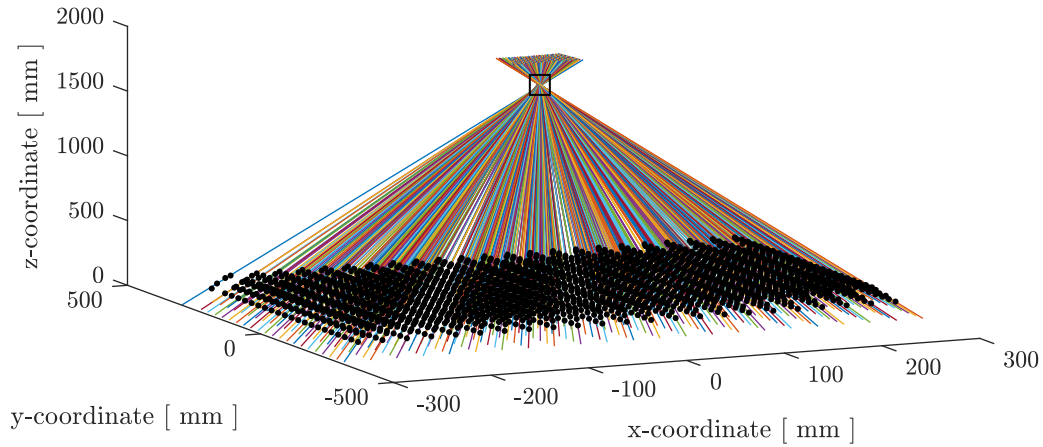
Figure 2.14: Three dimensional view of the camera calibration using four different heights of the calibration plate.

Digital Projector

The dot trajectories are calibrated in a similar way to the camera calibration, where the patterns are projected onto different horizontal heights. Each pattern is projected onto two horizontal planes at different heights, and the shifts in the positions are compared. Because the camera is already calibrated and the height of the plates are known, the real world coordinates of the projected dots (x, y, h) are easily found since each pixel trajectory only intersects the $z = h$ plane once. In figure 2.17, two images are shown, where the patterns are projected at two different heights: $z = 0$ cm and $z = 36.71$ cm. These images clearly show the dominating shift along the $x-$direction compared to the smaller shift along the $y-$direction due to changes in the height of the surface onto which the dots are projected.

(a) $z = 0.0$ cm (b) $z = 36.71$ cm

Figure 2.15: Images of the projector calibration where the first patterns is projected at two horizontal planes at different heights.

In figure 2.16, a two dimensional schematic representation of the projection calibration is shown in real world coordinates, i.e. a side view of the (x, z)-plane. The patterns are projected at $z = 0$ cm, h' and h''. The real world coordinates of a single dot on the different heights are used to construct the trajectory of that dot. Linear regression is used on the real world coordinates of each dot to construct the trajectory through the points at different heights. The solution of this trajectory is defined by a vector. The origin of the vector is defined similar to the camera calibrations, at the bottom (x_P, y_P, z_P) with $z_P = 0$ cm. This vector is composed of the three components normalized along the vertical, i.e. the magnitude in the vertical is $dz_P = 1$ cm. The magnitude in x and y directions are given by dx_P and dy_P, respectively. In the calibration of the digital projector, no fits are needed since only the 3000 trajectories have to be determined. The trajectory (vector) of each dot is then allocated to the corresponding dot. The final set of trajectories are shown in figures 2.17 (a) and (b). The patterns are projected on four different levels $z = 12.8, 17.3, 21.8$ and 26.3 cm indicated by black dots. The trajectories obtained from these four heights, intersect in the pinhole model of the projector at $H_P = 158$ cm, indicated by the red square. Similar to the camera calibration, we have found a small region in space where all trajectories intersect, coinciding with the location of the projector. Note that the calibration here is given in millimeters and that the coordinate system is defined by the center of the PIV calibration plane. In the measurements, we use a translated coordinate system where the position of the digital projector is set to $(0, 0, H_P)$ to match the height calculations of the pattern matching technique.
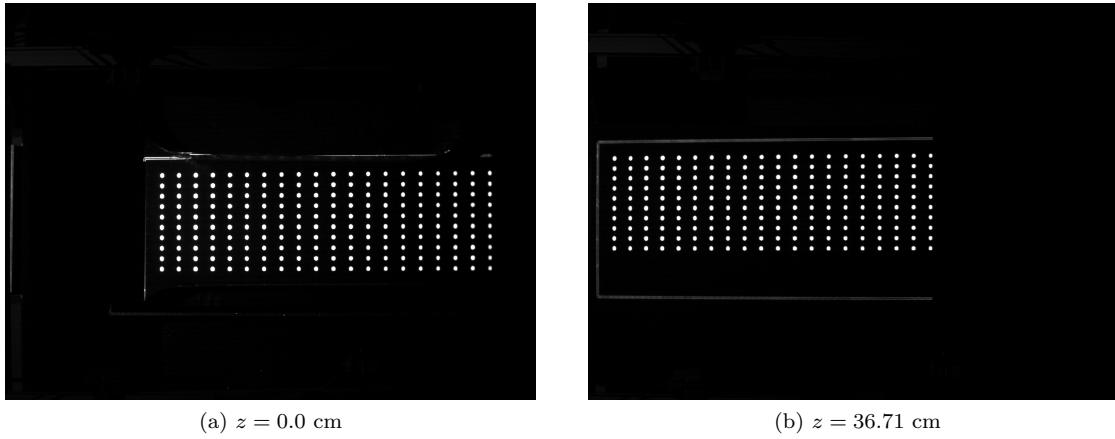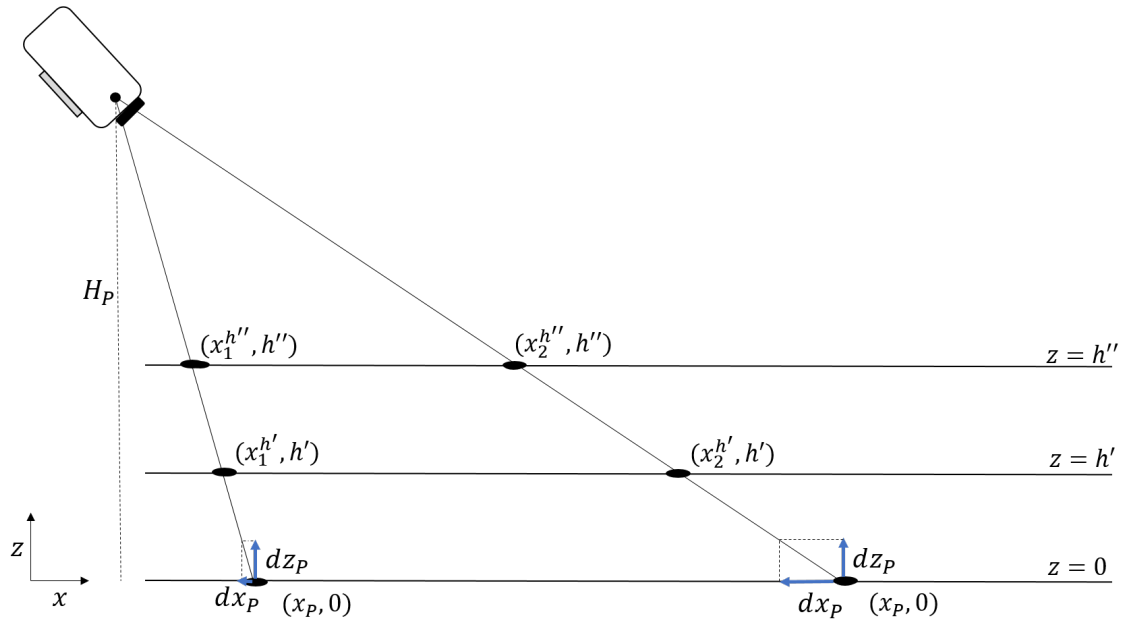
Figure 2.16: Two dimensional schematic representation of the projector calibration in real world coordinates. Two points x_1 and x_2 of the projection are indicated by black dots at three different heights at $z = 0$, h' and h'' cm. Photographs of these projections are taken with the calibrated camera. Therefore, one can determine the real world coordinates of the dots at each height since a pixel trajectory only intersects a horizontal plane once. The dot trajectories are determined in real world coordinates via the least square method after which the corresponding dot vector is defined having its origin at $(x_P, y_P, z_P = 0 \text{ cm})$ and magnitudes $(dx_P, dy_P, dz_P = 1 \text{ cm})$.
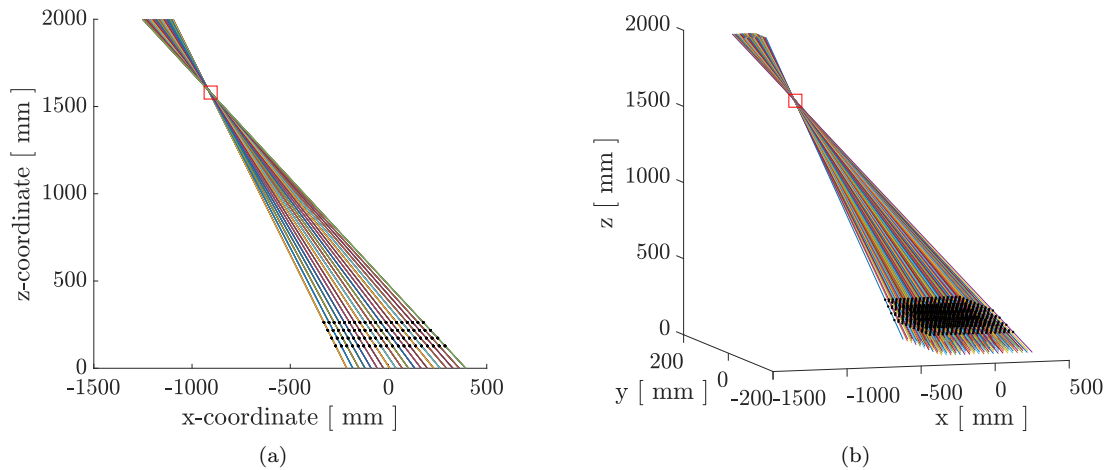
Figure 2.17: (a) Two and (b) three dimensional representation of the calibration of the dot trajectories in real world coordinates. The dots, indicated by black dots, are projected on four horizontal plates at $z = 12.8$, 17.3, 21.8 and 26.3 cm. The obtained dot trajectories intersect at the pinhole of the projector, indicated by the red box at $(X_P = 906 \text{ mm}, Y_P = 94 \text{ mm}, H_P = 1580 \text{ mm})$. The coordinate system is defined by the camera calibration.

2.4 Tests and comparison between both measurement techniques

The chronological description of the different stages are described by three different versions of the pattern matching technique. During each 'stage' in the project, a different version of the technique is implemented. The final version of the pattern matching technique, as discussed in section 2.2.1, is the result of different insights obtained from earlier stages throughout the project. With versions here, we refer to the different calculation methods or approximations given by equations (2.20), (2.22) and (2.10), respectively.

During the first two stages of the project, we studied the height calculations of the pattern matching technique of De Zwart (2017), and implemented the effect of variations in the projection angle and refraction at the water surface. During the third stage of the project, we implemented and studied the photogrammetric technique, which led to the finding of the conceptional errors made in the previous versions/approximations of the pattern matching technique. The corrected version of the pattern matching technique is called the third version of the pattern matching technique (section 2.2).

In this work we present each stage for three reasons. The different insights that are made throughout the entire project can now be indicated to a specific stage. The final version of the pattern matching technique and the implementation of the photogrammetric technique are the outcome of all these insights. Secondly, by presenting a complete story, one can easily acquaint the conceptual differences that are illustrated in the different versions. The third reason, is that some assumptions we made and did not hold, can be valid under different positioning of the camera and projector. Therefore, an approximated method could be used like in the work of De Zwart (2017), who accurately measured the bottom morphology using the first version of pattern matching technique.

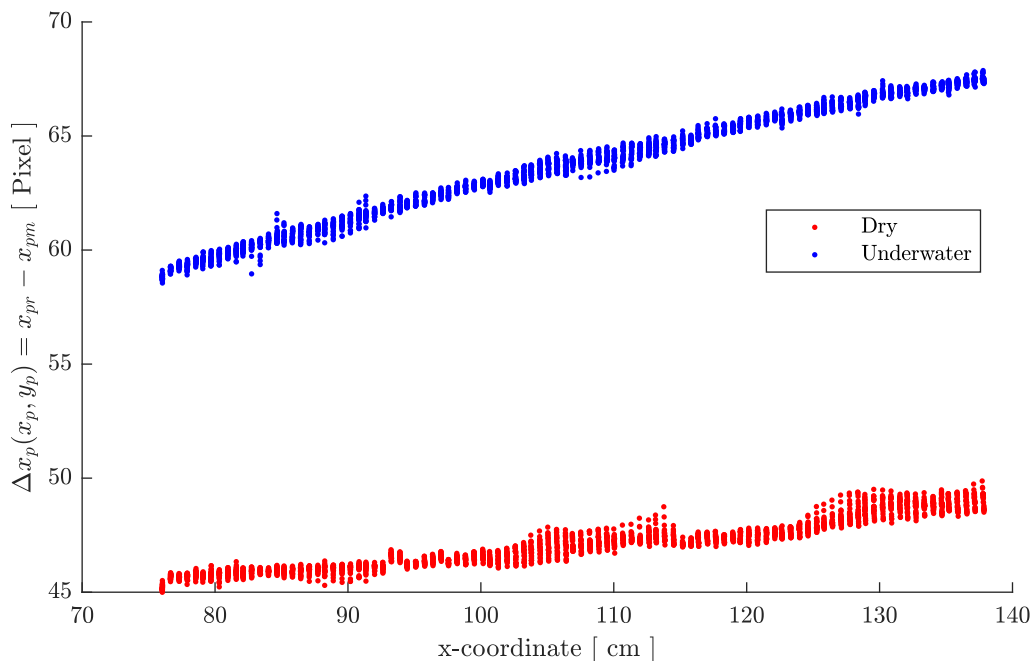Figure 2.18: The differences in pixel positions between the reference measurement and the measurement of a horizontal plate at $z = 4.75$ cm, in dry $\Delta x_p(x_{pd}, y_{pd})$ (red) and underwater $\Delta x_p(x_{pw}, y_{pw})$ conditions (blue), respectively. The water level of the underwater measurements is $H_W = 11.53$ cm. The shifts in pixel are given as function of the $x-$coordinate in real world coordinates.

A test measurement of a horizontal plate is performed to investigate the performance of each technique. The measurements of the plate are performed in both dry and underwater conditions, where the water layer has a height of $H_W = 11.53$ cm. By measuring the plate in both conditions, the effect of refraction is investigated.

In all three versions of the pattern matching technique, the same input $\Delta x_p(x_p, y_p)$ is used and only the method of height calculation changes. The measured shifts in pixels for each dot are given by $\Delta x_p(x_p, y_p) = x_{pr} - x_{pm}$, and are shown in figure 2.18. The locations of (x_{pr}, y_{pr}), are determined in a dry reference measurement. The coordinate (x_{pm}, y_{pm}), represents the measured pixel coordinates of the projected dots on the plate in dry and underwater conditions. The positions of the dots in the images are obtained via the detection method described in section 2.1. The pixel coordinates are transformed to real world coordinates via the transformation discussed in section 2.2.3.

In both dry and underwater measurements, an increasing relation between pixel difference and the $x-$coordinate is found. The magnitude of $\Delta x_p(x_{pw}, y_{pw})$ in underwater conditions has a offset of 15 pixels with respect to the dry measurement, and increases more strongly. This offset can be explained via the refracted positions where the $x_{rd} - x_{md} < x_{rd} - x_{mw}$.

The dry measurement shows a larger scatter in the measured $\Delta x_p(x_{pd}, y_{pd})$ that are not the result of variations in the measured plate. Moreover, if variations in $\Delta x_p(x_{pd}, y_{pd})$ are from deformation in the plate, the underwater measurement should also contain the same variations in $\Delta x_p(x_{pw}, y_{pw})$. The spread and intensity of a projected dot, strongly depends on the surface onto which the dot is projected. On the bottom of the tank, a stainless steel plate is added to increase the contrast between the projected dots and the background. For the horizontal measurements of a plane, a PVC plate is used. However, in dry conditions the difference in light scattering on different surfaces is more present than in underwater conditions. The preprocessing of the images, i.e. conversion to binary, is done via the Matlab function *imbinarize*. The function transforms the images into binary via an adaptive thresholding. The input values for this adaptive tresholding are based on underwater conditions. The inputs for dry measurements should be adjusted due to the difference in scattering. More research on this topic, together with the size of the projected dots, are already addressed in a new study.

2.4.1 Pattern matching technique, version I

The calibration of $C_{1,2}$ is done by the inclined plate shown in figure 2.8. The calibration is first performed in dry conditions, to measure the angle of the plane γ along the $x-$direction, $\frac{dh}{dx} > 0$. The projections of x_{md} and x'_{md} represent the outer columns of the measurement area with $\Delta x = x'_{md} - x_{md} = 71.2$ cm. The height difference over Δx is given by $\Delta h = h'(x_{md}) - h(x_{md}) = 4.17$ cm. The angle of the plate can be calculated and is $\gamma = \arcsin(\frac{\Delta h}{\Delta x}) = 3.36°$. It is kept constant for dry and underwater calibrations. Using $h(x) = \sin(\gamma) \cdot x + h_0$, we can calculate the (average) magnitudes of C_1 and C_2 for dry and underwater measurements, respectively. This yields

$$C_1 = \frac{h(x)}{\Delta x_p(x_{p1}, y_{p1})} = 0.106 \text{ [cm/pixel]}, \tag{2.34}$$

$$C_2 = \frac{h(x)}{\Delta x_p(x_{p2}, y_{p2})} = 0.131 \text{ [cm/pixel]}, \tag{2.35}$$

where the subscript 1 and 2 of the pixel coordinates, indicate the obtained positions for dry and underwater conditions.

The measured increasing $\Delta x_p(x_p, y_p)$ for the horizontal plate, shown in figure 2.18, can not be explained from the relation $h = \Delta x_p / \tan(\theta)$, since both h and θ are constants. When the measured $\Delta x_p(x_p, y_p)$ is multiplied by the constant factors $C_{1,2}$, the same (scaled) relation between the height and x is found. In figure 2.19, the two results of the first version of the pattern matching technique are shown. The results show an increase in h along the $x-$coordinate, and for the underwater situations h is calculated around 8.5 cm, whereas the plate was positioned at $z = 4.75$ cm. Therefore, we conclude that the approximations of the first version do not hold for the used setup.
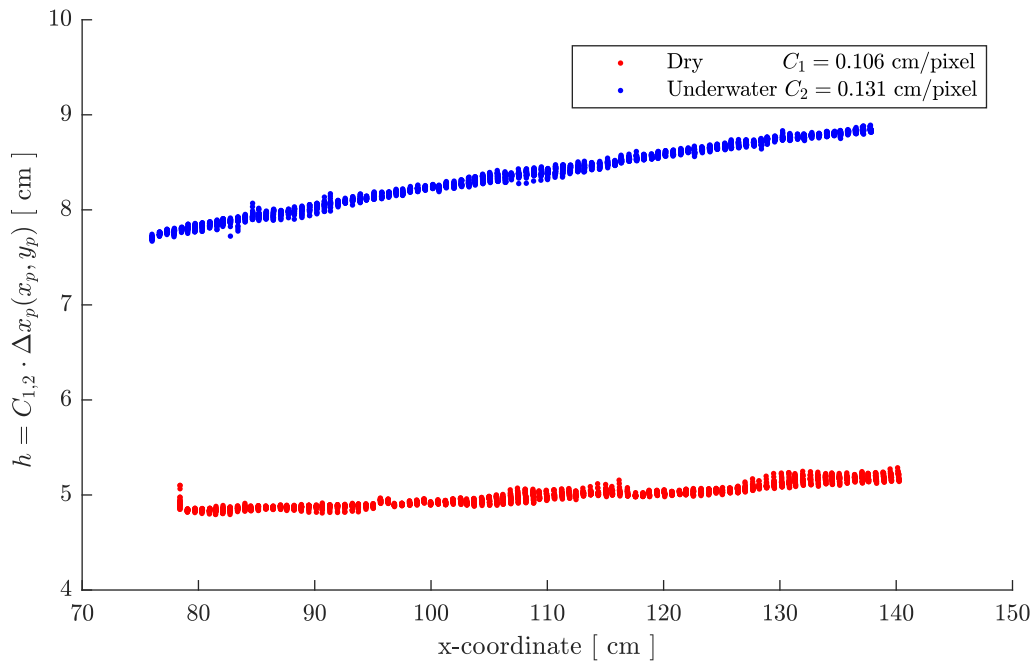
Figure 2.19: Calculated height of a horizontal plate at $z = 4.75$ cm using the first version of the pattern matching technique, equation (2.22). The red dots indicate the calculated heights in dry conditions and the blue dots represent the underwater measurement with $H_W = 11.53$ cm.

2.4.2 Pattern matching technique, version II

Inside the measurement area, we measured the variation of the projection angle in dry conditions. We found that $26° < \theta_1^x(x_{rd}) < 42°$ and thus the assumption of a constant θ is questionable. Using equation (2.3), we can calculate the variation on $\theta_2^x(x_{mw})$. Both angles are shown in figure 2.20. The magnitude of the shift $d(x_{rd}, H_W)$ in the x−coordinate due to refraction is calculated using equation (2.6), and is also given in figure 2.20.

When both effects are calculated and included in the height calculation, we evaluate equation (2.22), shown in figure 2.21. The calculated height of the horizontal plate without water is indicated by the red points and the underwater measurement is indicated by the blue points. The variation/noise in the calculated height h is the result of the variation in $\Delta x_p(x_p, y_p)$ due to the centroid detection in dry and underwater conditions. The second version of the pattern matching technique, calculates the height of the horizontal plate closer to the physical height of $z = 4.75$ cm than the first version, where $h \approx 8$ cm. However, there is still a large discrepancy between the calculated height and the horizontal level in real world coordinates. In both conditions, the calculated height decreases along the x−axis.

Additional dry test measurements are performed and the same trend is found in the calculation of other horizontal planes. These dry measurements of a horizontal plate positioned at $z = 2.05$, 4.50 and 6.50 cm are normalized to investigate the influence of $1/\tan\left(\theta_1^x(x_{rd})\right)$ in the dry height calculations: equation (2.22). It is the factor which is used to calculate the vertical height from horizontal displacements in dry conditions. The difference in the dot locations are divided by the constant height of the plate to find the relation between shift and height i.e. $\tan\left(\theta_1^x(x_{rd})\right) \overset{?}{=} (x_{rd}-x_{md})/h$. The relation between $(x_{rd}-x_{md})/h$ and the known height of a plate $z = h$ is shown in figure 2.22, together with $\tan\left(\theta_1^x(x_{rd})\right)$. This figure shows a disagreement of current theory since $(x_{rd} - x_{md})/h \neq \tan\left(\theta_1^x(x_{rd})\right)$. The three normalized height measurements all intersect in one curve. However, the $\tan\left(\theta_1^x(x_{rd})\right)$ is expected to follow the same profile. The magnitude
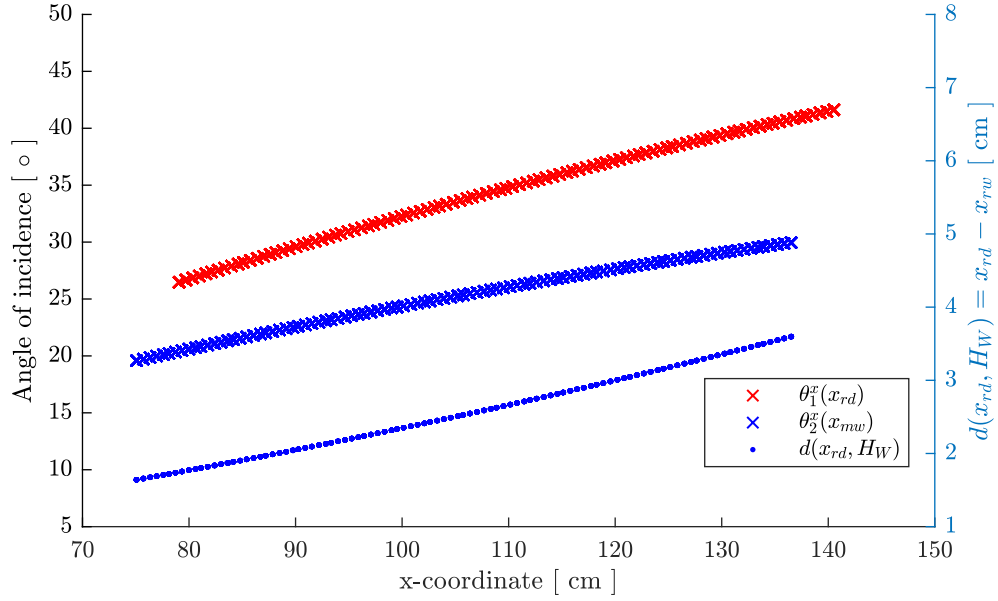
Figure 2.20: The two adjustments in the second method of the height calculations: the angle of incidence $\theta_1^x(x_{rd})$ and horizontal shift $d(x_{rd}, H_W)$. The angle of incidence $\theta_1^x(x_{rd})$ at the water surface and the angle of incidence at the bottom $\theta_2^x(x_{mw})$ in the (x, z) plane are represented by the $\times$ markers. The horizontal shift in reference location due to refraction for $H_W = 11.53$ cm is indicated by the blue dots. The blue and red marker colors indicate underwater and dry situation, respectively.

of $\tan\left(\theta_1^x(x_{rd})\right)$ is thus too small for $x < 90$ cm and too large for $x > 90$ cm. Therefore, the inverse factor $1/\tan\left(\theta_1^x(x_{rd})\right)$ is over predicting the height for $x < 90$ cm and under predicting the height for $x > 90$ cm. This explains the decreasing behaviour for the obtained results in figure 2.21. Moreover, the under prediction of h in underwater conditions, is due to the difference in magnitude of $\theta_2^x(x_{rd})$ and $1/\tan\left(\theta_2^x(x_{rd})\right)$ not shown in 2.22. This effect is not further discussed since the dominating effect here is the difference in $(x_{rd} - x_{md})/h$ and $\tan\left(\theta_1^x(x_{rd})\right)$. The transition point of over and under predicting the height is exactly the $x-$coordinate of the camera at $X_C = 90$ cm. In the third version of the pattern matching technique, we include the influence of the camera and the angles $\alpha_{1,2}^{x,y}(x, y)$ between the location of the camera (X_C, Y_C, H_C) and measured point (x_{md}, y_{md}, h).
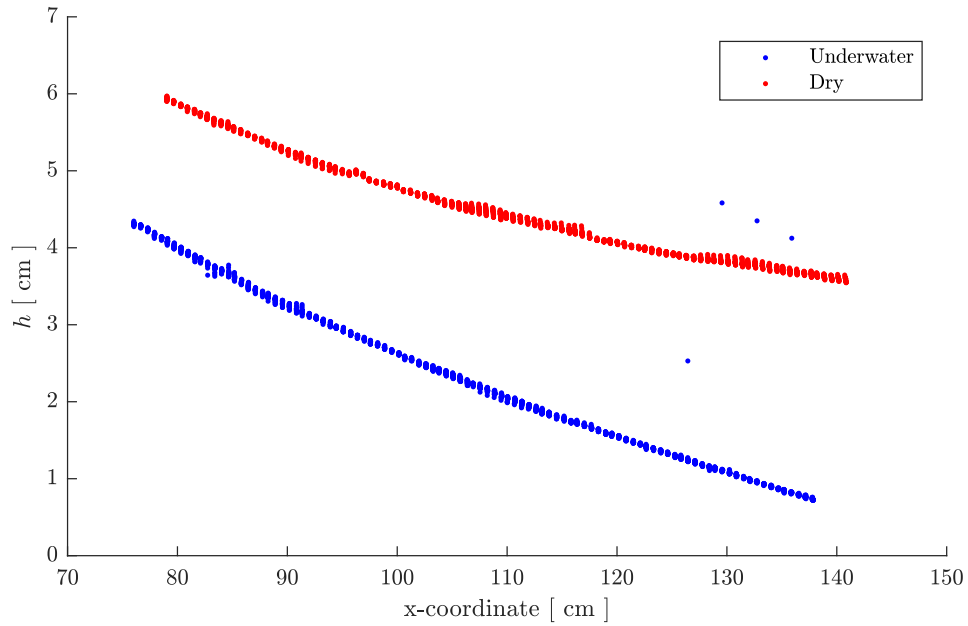
Figure 2.21: Calculated height of a horizontal plate at $z = 4.75$ cm using the second version of the pattern matching technique, equation (2.20). The red dots indicate the calculated heights in dry conditions and the blue dots represent the underwater measurement with $H_W = 11.53$ cm.
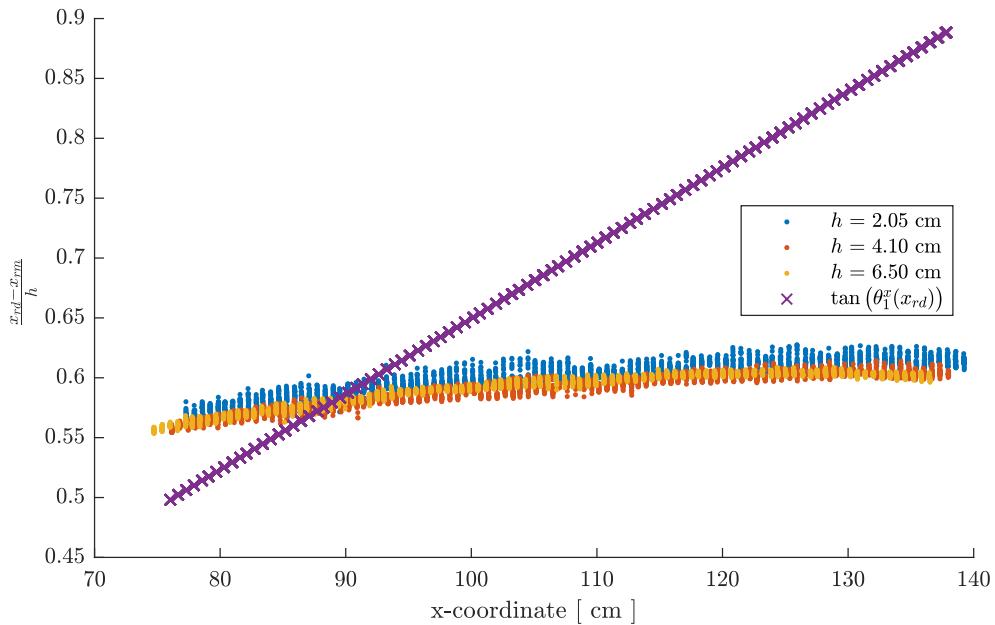
Figure 2.22: Normalized location difference for measurements of a horizontal plate positioned at three different heights in dry conditions. The plate is measured at $h = 2.05$, 4.10 and 6.50 cm. The $\tan\left(\theta_1^x(x_{rd})\right)$ obtained from the dry reference measurements is also shown to check the theory.

2.4.3   Pattern matching technique, version III + Photogrammetry

After the implementation of the photogrammetric technique, we found an incorrect interpretation of the transformation from pixel coordinates to real world coordinates. The first correction is shown in figure 2.6, where the angles $\alpha^x_{1,2}(x_{mw})$ between the position of the projected dot and the camera are included. Secondly, we transform the pixel coordinates (x_p, y_p) to other real world coordinates $(x_m, y_{mw}, 0)$ at $z = 0$ cm, using the transformation $Pix2Cm(0)$.

Because these effects were found after the photogrammetric technique was implemented, which provided more accurate results, we did not include the calculations of $Pix2Cm(z)$ and $\alpha^x_{1,2}(x_{mw})$ for underwater measurements. However, we have included the $\alpha^x_1(x_{md})$ for dry measurements.

Pattern matching technique, version III

The result of the height calculations of the plane at $z = 4.75$ cm in dry conditions, is shown in figures 2.23 and 2.24, where a two and three dimensional representation of the plane given. The same pixel differences $\Delta x_p(x_{pr}, y_{pr})$ between the reference and measured plane are used. However, different real world coordinates for x and y are obtained for the height calculation. The red dots indicate the measured surface in dry conditions. The obtained surface accurately represents the horizontal plane with a maximum error of $\epsilon = 0.075$ cm. Note that the variations in the measured pixel difference (figure 2.18) are also found in h. Therefore, we conclude that the accuracy of the pattern matching technique is limited by the accuracy of the obtained dot positions. The calculation of the height in dry conditions are accurate enough for the current project, since the average diameter of the sediment particles is 0.25 cm. However, the final goal is to perform underwater measurements and thus, we chose to proceed with the photogrammetric technique.

Photogrammetry

After the calibration of the camera and digital projector, we know the trajectories of the projected dots and the pixels in the field of view of the camera. When the dot patterns are being projected onto the horizontal plate at $h = 4.75$ cm, we can calculate the corresponding intersections of both trajectories. This can be done for underwater and dry conditions. The results are shown in figures 2.25 and 2.26. Figure 2.25 shows the result of the height calculation in the (x, z) plane similar to the results of the pattern matching techniques. The calculated h is in agreement with the physical height of the plane in both dry and underwater measurements. The red points indicate the calculated height in dry conditions and show a small deviation around $x = 80$ cm. The underwater measurement shows the opposite effect where the calculated height is smaller than the physical height. The magnitude of the error $\epsilon = 0.05$ cm is smaller than the error of the pattern matching technique. In figure 2.26, a complete three dimensional overview is given of the measurement area.

Note the difference between the results of the pattern matching and photogrammetric techniques. Figures 2.23 and 2.25, show the different results of the height calculations in dry conditions. Both calculations methods use the same set of centroids of the projected dots on $z = 4.75$ cm. Therefore, we conclude that the reference measurement in the pattern matching technique contains the errors found in the pattern matching technique, since these variations are not found in the results of the photogrammetric measurements.
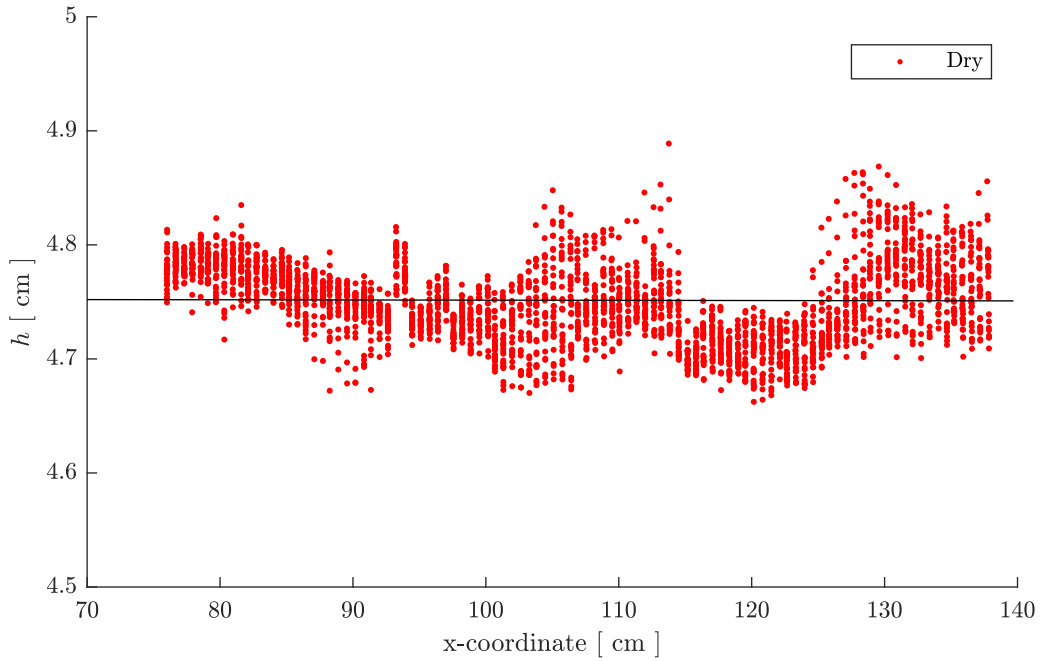
Figure 2.23: Calculated height of a horizontal plate in dry conditions at $z = 4.75$ cm using the third version of the pattern matching technique, equation (2.10).
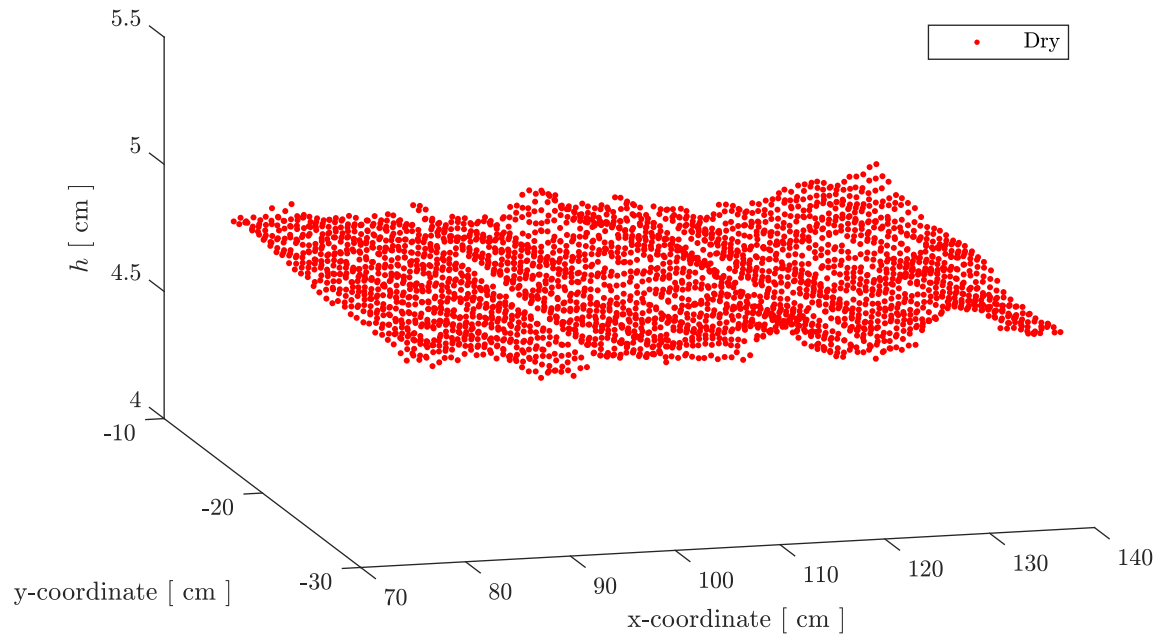
Figure 2.24: Three dimensional height calculation of a horizontal plate in dry conditions at $z = 4.75$ cm using the third version of the pattern matching technique, equation (2.10).
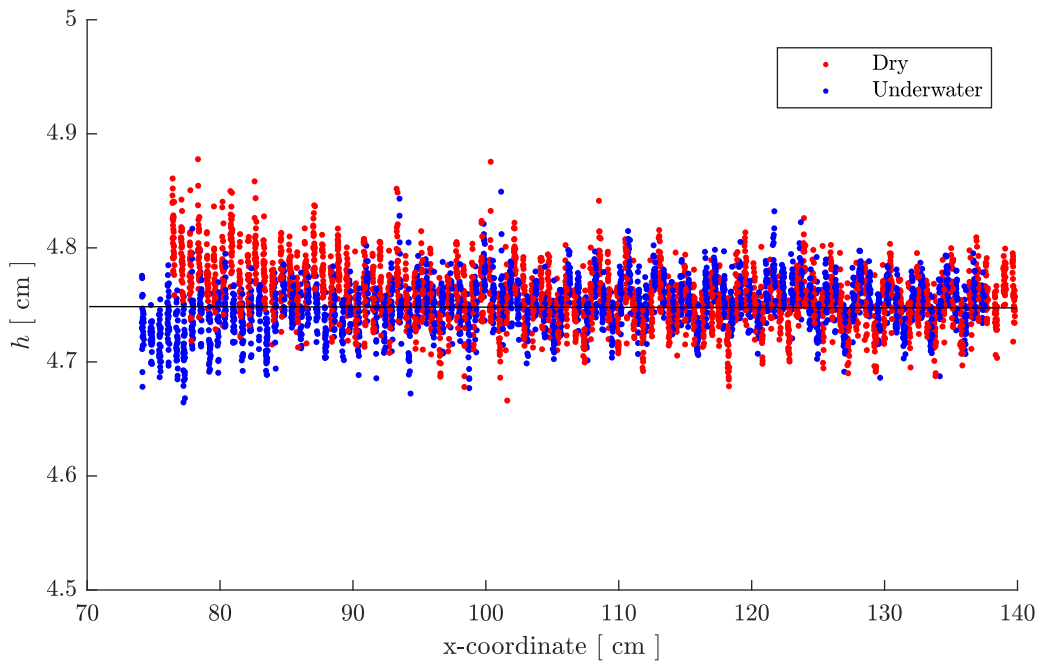
Figure 2.25: Calculated height of a horizontal plate at $z = 4.75$ cm using the photogrammetric technique. The red dots indicate the calculated heights in dry conditions and the blue dots represent the underwater measurement with $H_W = 11.53$ cm.
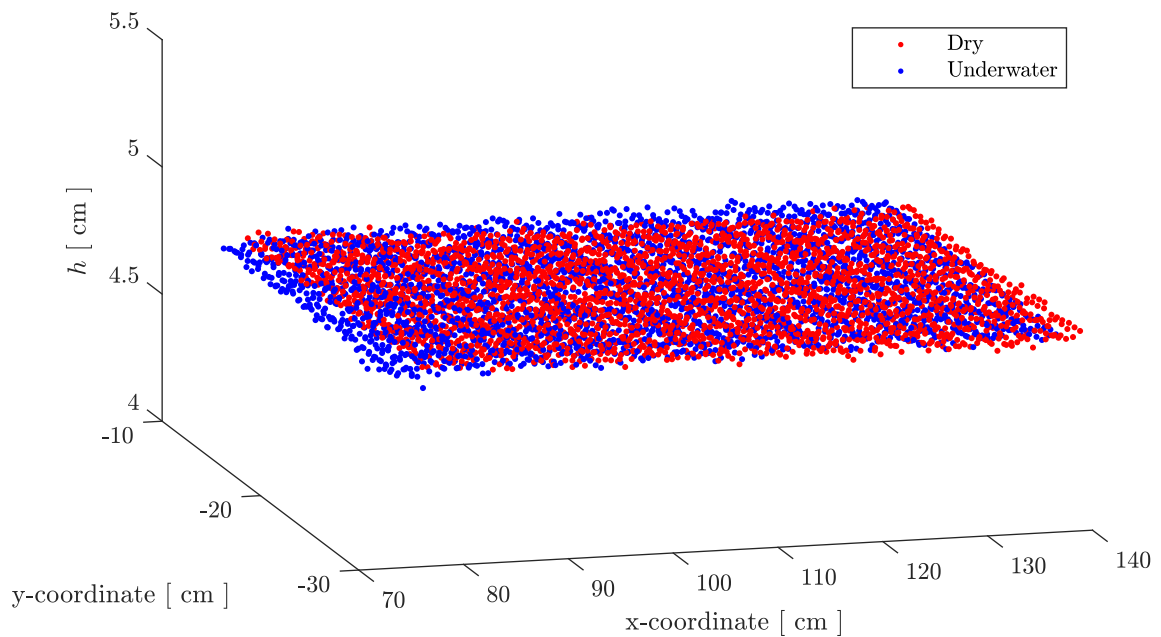
Figure 2.26: Three dimensional height calculation of a horizontal plate at $z = 4.75$ cm using the photogrammetric technique. The red dots indicate the calculated heights in dry conditions and the blue dots represent the underwater measurement with $H_W = 11.53$ cm.

Discussion

After the final corrections in the pattern matching technique, we found that the techniques are very similar. They both calculate the bed morphology using the same principles and positions of the centroids on the images. The angles, explicitly calculated in the pattern matching technique, are also found in the vector components of photogrammetry, e.g. $\frac{dx_P(x)}{dz_P(x)} = dx_P(x) = \tan\left(\theta(x)\right)$, since $dz_P = 1$ cm. The largest difference between the techniques is the calibration method. Because both techniques use the same dot positions from the dot detection method, it is the calibration of the techniques that is the governing factor in the accuracy of the calculated height.

The calculations of the pattern matching technique are based on the positions of the projected dots at $z = 0$ cm, and the angles under which the dots are projected and captured. This requires to measure the physical positions of the digital projector (X_P, Y_P, H_P) and the camera (X_C, Y_C, H_C), which can be problematic.[6] Moreover, the relation $Pix2Cm(z)$ is defined by four points. This relation is needed to correctly obtain the real world coordinates of the reference measurement $(x_{rd}, y_{rd}, 0)$ and measurement $(x_{md}, y_{md}, 0)$ in dry conditions. From these locations, we calculated the angles $\theta_1^{x,y}(x_{md}, y_{md})$ and $\alpha_1^{x,y}(x_{md}, y_{md})$, that are used for the height calculation.

The calibration of the photogrammetric technique is performed differently. The accuracy of the camera and projector calibration is limited by the physical measurements of the heights and distances between the white dots on the PIV calibration plate. Since the error on these measurements is smaller, a more accurate reconstructions can be performed. Moreover, the camera calibration using $f_z(x_p, y_p)$ and $g_z(x_p, y_p)$, includes possible lens and camera deformations. These effects are not included in the pattern matching technique that uses $Pix2Cm(z)$. To remove the

Figure 2.27: Error of (a) the pattern matching technique and (b) photogrammetric technique. A horizontal plate at $z = 21.8$ cm is used to calculate the difference $h - 21.8$ cm and is shown for both techniques.

difference in light scattering that depends on the surface onto which the dots are projected, we use a PVC plate positioned at $z = 1.25$ cm as new reference height for the pattern matching technique. This allows us to measure the magnitude and spatial dependence of the errors of both height calculations methods. Two comparison measurements are preformed and shown in figures 2.27 and 2.28. The plate is positioned horizontal at $z = 21.8$ cm and $z = 26.3$ cm and measured in dry conditions. The difference of the calculated height and the physical height is shown for both techniques, $h - 21.8$ cm and $h - 26.3$ cm, respectively. These images show that the error of the pattern matching technique is radially dependant to the position to the camera. Underneath the camera, located at $(X_C = 90$ cm, $Y_C - 22.5$ cm), we find the maximum error (over prediction). At the outer edges of the measurement area, we find an under prediction of the height. This shows,

---

[6]The actual required position for the calculations is the pinhole of the camera and projector that cannot (directly) be measured. Therefore, some uncertainty will be present in the calculations of the pattern matching technique.

that deformations in the lens are not included in the pinhole model of the camera, leading to an incorrect calculation of the actual $\alpha_1^{x,y}(x_{md}, y_{md})$.

The magnitude of the error in the photogrammetric technique is smaller. The plate is correctly measured with an accuracy of $\epsilon = 0.05$ cm. However, there are some regions where the error is larger. These 'spots' are also found in the results of the pattern matching technique, located at ($x = 85$ cm, $y = -17.5$ cm). Therefore, we assume that the camera (lens) contains some defects that are not included in both camera calibrations. In the results of the photogrammetric measurements we have small height gradients along the $x-$coordinate. The sign of gradient differs in both measurements and the magnitude is smaller than the accuracy of the physical installation and height measurement of the 'horizontal' plane. Therefore, we assume that the plates are not positioned horizontally but under a slope that we have measured.
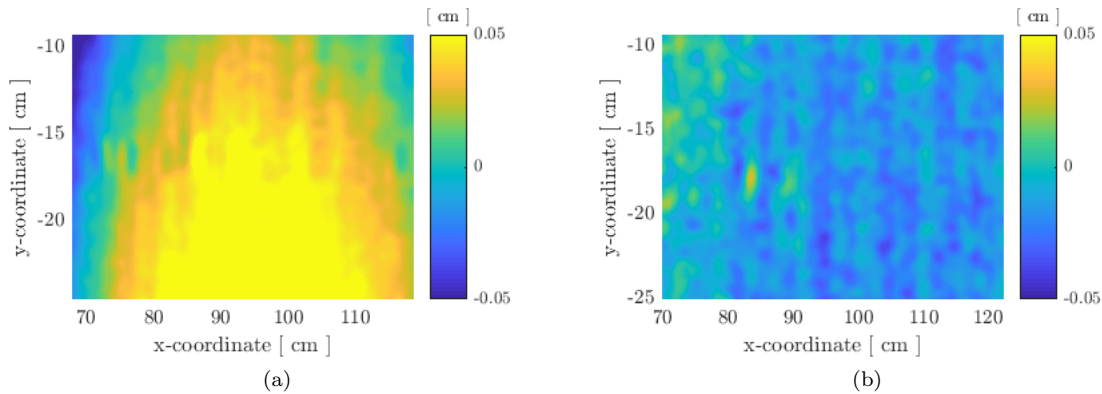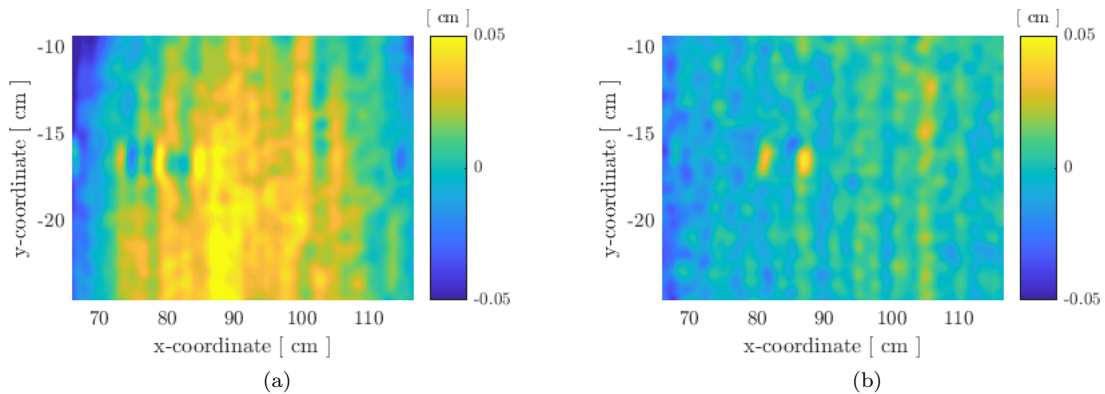

Figure 2.28: Error of (a) the pattern matching technique and (b) photogrammetric technique. A horizontal plate at $z = 26.3$ cm is used to calculate the difference $h - 26.3$ cm and is shown for both techniques

The calibration of the pattern matching technique uses a single dry reference measurement of the projected dot patterns onto the (metal) bottom plate. From the obtained dot locations we calculate the angles θ and α of the dot trajectories and pixel trajectories, respectively. For the calibration of the photogrammetric technique, we position a PVC plate on several heights onto which the dot patterns are projected. Because the detection of the dots is not perfect, due to the transformation to binary, we expect little uncertainty in the obtained centroids. In the calibration of the photogrammetric technique, we used the least square method to increase the accuracy of the obtained trajectories.[7] A second (minor) effect is the different material onto which the dots are projected and captured. The dot detection is based on projections onto a sediment bed, whereas in the calibration measurements, we used a metal and a PVC plate for the pattern matching and photogrammetric technique, respectively. Because reflection and scattering of the the projection depends on the surface, there is a change in the intensity of the dots on the images and thus in the obtained dot positions. This effect is assumed to be negligible and not investigated in this project $\epsilon \approx 0.1$ pixel. The calibration of the pattern matching technique depends completely on the accuracy of the obtained centroids in the dry reference measurement. For photogrammetry, a number of horizontal heights are used and thus an error on the obtained location of the centroids averages over the different heights, resulting in a more robust calibration. The magnitude of the error in the pattern matching technique is larger, and the calibration of the photogrammetric technique is recommended. Note that the camera calibration used in photogrammetry, can be implemented into the pattern matching technique. The surfaces that are presented in the remainder of this work, are measured with the photogrammetric technique.

---

[7]Increasing the height difference of the calibration levels, decreases the uncertainty on the obtained trajectories.

Chapter 3

Bed evolution under an oscillating flow

In this chapter, we present the laboratory setup and implementation of the morphology and Particle Image Velocimetry (PIV) measurement techniques. The photogrammetric technique is used to calculate the sediment bed thickness under an oscillating flow inside a tidal channel. In section 3.1, we describe the experimental setup that is used to measure the transient sediment bed thickness and tidal velocity field at the water surface. The sediment bed thickness is measured during flow reversal, in the absence of moving sediment due to the turning tidal velocity $v \approx 0$ cm/s. For this, the duration of the measurement has to be shorter than the flow reversal. First, we describe the synchronization between the morphology measurements and the tidal motion, discussed in section 3.1.2. Secondly, we present the implementation of PIV that led to the finding of a discontinuous illumination of the digital projector. This finding allowed to perform PIV and morphological measurements simultaneously, and it is detailed in section 3.1.3.

The measurements that are performed during flow reversal are influenced by a changing water level height. The effect of changing H_W on the sediment thickness calculation is investigated in section 3.2. Moreover, the fluid velocity at the free surface is measured for different water levels to investigate the flow characteristics. Finally, we present the results of the bed morphology and fluid velocity inside the tidal channel for an experiment in which a random bed morphology self-organizes into a dune that migrates through the channel.

3.1 Experimental setup and implementation of measurement techniques

3.1.1 Experimental setup

The experiments are performed in a 150 cm $\times$ 100 cm $\times$ 30 cm perspex tank that is partially filled with tap water. A false bottom of 100 cm $\times$ 100 cm $\times$ 5 cm is positioned inside the tank and covered by a metal plate of 90 cm $\times$ 100 cm for more stability. It defines the reference height $z = 0$ cm and creates a shallow region. Two curved metal barriers with a height of 10 cm are positioned on the false bottom and form a tidal channel with a length of 65 cm and width of 21 cm that divide the tank into an open area, that represents the sea side, and a semi-enclosed basin or estuary. A schematic representation of the side and top view of the experimental setup are given in figures 3.1 and 3.2, respectively. A digital projector is positioned under an angle and projects dot patterns onto the bottom of the tidal channel. Two cameras are positioned above the channel, one is used to photograph the changes in the projected patterns, and the other to measure the velocity field using PIV. The oscillating flow inside the channel is the result of the 'tides' generated by a piston that oscillates into the water with period T and amplitude $\Delta H_{\text{piston}}/2$.

Increasing the length of the channel results in larger disturbances at end the tidal channel due to the back wall of the tank. The minimum distance used throughout this project is 15 cm, as shown in figure 3.2. At the sea side of the channel, a different effect is present. The channel and estuary are positioned on the false bottom that create a step in the bottom profile. Via colored dye experiments, we visualized the tidal flow and found no significant effects at the entrance of the channel if it is positioned at 20 cm from the step. The metal plate on top of the false bottom is added to provide a stable reference height and more contrast on the images of the projections. Since air or sediment can creep under the plate during drainage of the water it is important to check the height of the metal plate since it is used as the reference plane throughout the project.

The false bottom is covered with polystyrene particles of variable shape and size, but with an average diameter of 2.1 mm and a density of 1055 kg/m^3, also used by Van der Linden (2014). The small difference in density between the water and sediment makes them almost neutrally buoyant in water. This makes the particles especially useful in the laboratory experiments since they will get transported easily and will make the sediment transport easily measurable. The sediment bed is leveled before adding additional sediment ripples/patches. Via two rectangular barriers of $\Delta z = 2.0$ cm, that are positioned at both ends of the false bottom we can level the bed using a rigid scraper to control the initial volume of sediment in the measurement area.

The channel openings are rounded circular with a radius of 9 cm. The rounded channel ends are used to remove the erosion effects of scour holes due to the strong convergence of fluid flow in these regions. Note that there is a difference in friction when sediment grains move over the metal plate or over the sediment bed. To remove this effect, a layer of sediment with sufficient thickness is required. The layer of 2 cm was sufficient for the test conditions in this particular setup.

The tides are generated via a piston connected to a linear EC-motor. The linear EC motor is controlled by a PID-controller that is actuated by the computer using the program LinMot Talk. The piston oscillates with an amplitude $\Delta H_{\text{piston}}/2$ and a period T. The cross-sectional area of the piston A_{piston} and oscillation amplitude are constant throughout all experiments. The position of the piston as a function of time is shown in figure 3.3. The red markers at $H_{\text{piston}}(t)$ indicate the moments at which the measurements are triggered. In section 3.1.2 and 3.1.3, we explain these triggers and give a complete overview of the timing during the measurements.
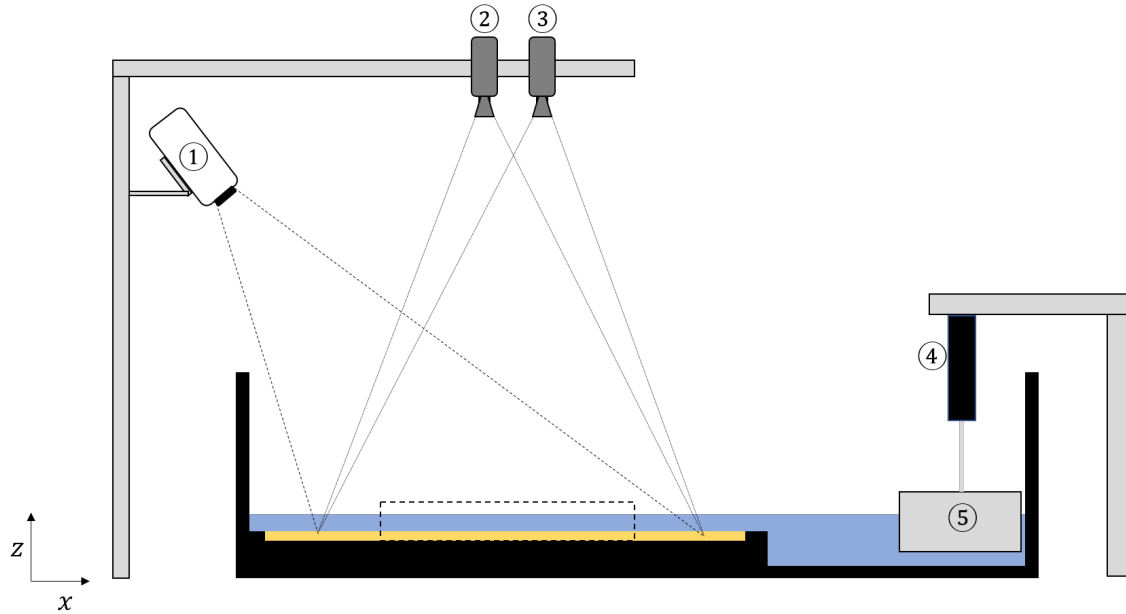
Figure 3.1: Two dimensional schematic representation of the side view of the experimental setup. The digital projector ① is positioned under an angle and projects dot patterns onto the sediment bed. Two CCD cameras ②, ③ capture the projected dots and floating tracer particles. Via an EC-motor ④ we oscillate the piston ⑤ that forces the water level to rise and fall accordingly.
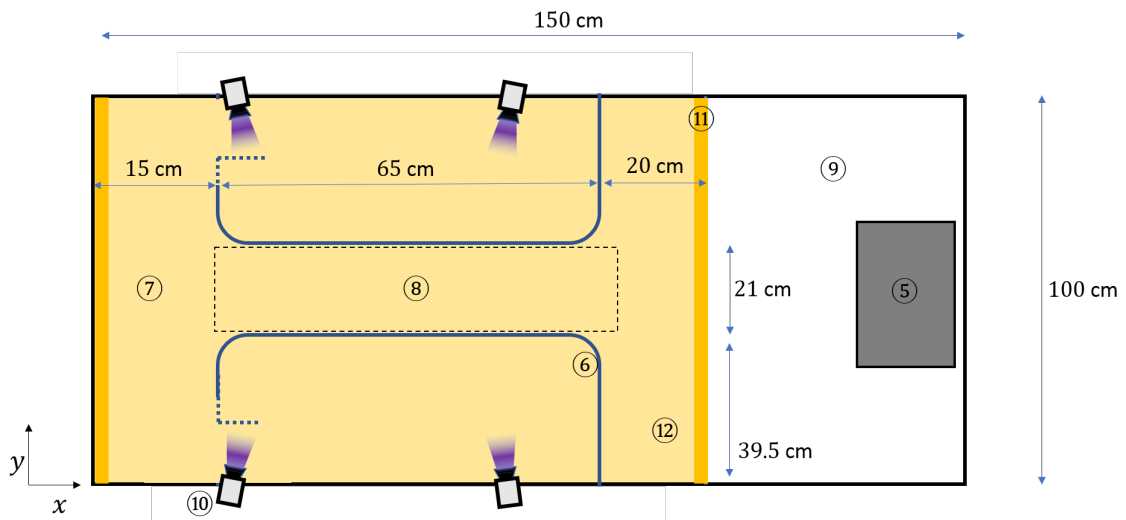
Figure 3.2: Two dimensional schematic representation of the top view of the experimental setup with the physical dimensions. The channel walls ⑥ divide the tank into three regions, a semi enclosed basin ⑦, the tidal channel ⑧ where the measurement area is indicated by the dashed box, and the sea side ⑨. Via four UV LED lights ⑩ we illuminate the tracer particles for PIV measurements. The horizontal barriers ⑪ with height $\Delta z = 2$ cm, are used to level the sediment and are positioned at the edges of the sediment domain. The water level $z = H_W$ is measured at the position of ⑫.

The morphodynamic measurement setup consists of an Allied Pike CCD camera (resolution: 1388×1038 pixels) and a Benq digital projector (resolution: 1920×1080 pixels) that is connected to the computer via a VGA connector. The camera is positioned above the channel at a height of $H_C = 177.4$ cm. The digital projector is mounted behind the tank in the extension of the tidal channel at a height of $H_P = 154.2$ cm. Both heights are measured from the center of the lenses.[1] This position of the projector enables to illuminate the complete bottom of the channel and the exit of the channel at the estuary side. There are parts close to the openings of the channel that are not illuminated due to the channel barriers blocking the projected light. A different position of the projector would be needed if the measurement area should include these shadowed regions near the entrance of the channel. During the project, we found a small shift (0.35 cm) in the projections during the first 30 minutes of illuminating. The digital projector heats up when operating which influences the field of projection. After 30 minutes, the field of projection stays constant and measurements are taken only after this 'warm up' time. We have also seen another effect where the entire field of projection gets shifted spontaneously. This shift is 2.1 cm into the negative $y-$direction. The moment at which the shift occurrence was random, and we have not solved this issue. However, we assume that it is an error between the digital and VGA-synchronisation. The field of the projector can be reset by restarting the projector.

The Particle Imaging Velocimetry (PIV) measurement setup consists of a RedLake MegaPlus 2 Double CCD camera (resolution: 1600×1200 pixels), positioned above the channel at $H_C = 179.1$ cm, and floating tracer particles. By photographing the tracer particles and comparing the positions of the tracer particles in two consecutive images, we can measure the velocity field at the water surface. The PIV calculations are performed with the program PIVview3C. The floating tracer particles are luminescent white polyethylene micro-spheres with a density of 980 kg/m^3 and a diameter of 600-700 μm (Coshperic 2018). They are coated with tween-80, a bio-compatible surfactant that protects the spheres from contamination and makes them hydrophilic. The density and (spherical) size are chosen so that the response time of the particles to the motion of the fluid is reasonably short, i.e. low Stokes number. This is required to accurately follow the flow while being large enough for detection by the PIV camera. The water surface is illuminated by four UV LED lights (Lz4-44UV00, Led Engin) positioned next to the channel, shown in figure 3.2. The particles absorb ultraviolet light ($\lambda = 365$ nm) and emit yellow-green light ($\lambda = 525$ nm). Because the spectrum of the UV diodes contains some wavelengths of the visible spectrum, the PIV camera is equipped with an UV-filter, which removes most of the reflection at the water surface and bottom of the tank.

3.1.2 Implementation of the morphodynamic measurement techniques

The morphodynamic measurements consist a digital projector and a CCD camera projecting and photographing the (deformed) dot patterns on the sediment bed inside the tidal channel during flow reversal. The calculations of the sediment bed thickness are preformed after the experiment is finished. In the following section, we discuss the different important aspects in the morphological measurements, i.e. the timing of projecting and photographing the patterns during the tides. We found that for short experiments, no synchronization between the measurement and oscillating piston is required. However, when experiments with more than 200 periods are performed, a synchronisation is needed.

Timing of projecting and imaging during flow reversal

The morphodynamic measurements are performed every N tidal periods. For short experiments, the camera is controlled via a LabView application and is triggered manually, making a continuous recording of the sediment bottom onto which the 15 dot patterns are projected. The digital projector is controlled by Matlab and activated manually at the moment of flow reversal inside the channel. The Matlab program consists of a loop that projects the patterns only during the flow reversal. In between two sets of projections, the projection program pauses $T - t'$ seconds, where

---

[1]The height of the calculated pinholes are $H_C = 179.5$ cm and $H_P = 158$ cm.

t' is the time it takes to project all the 15 patterns, measured via the internal clock of Matlab. The digital projector thus projects during alternating[2] flow reversals and the photographs are only taken when the camera is activated manually.

The goal is to perform fast measurements and minimize the time t'. This can be done by reducing the number of projections or increasing the projection rate. The number of patterns is already optimized and discussed in section 2.1. In the following, we discuss the rate at which the dot patterns are projected and captured. The camera can record at 30 frames per second (fps) while the digital projector operates at 60 fps. In theory, the measurements can be performed within $t' = 0.5$ seconds since only 15 frames are needed. To photograph the images with enough contrast in intensity, the exposure time of the camera is varied between 4 and 20 milliseconds, see section 3.1.3. The exposure time of the camera can be further decreased but this results in images with (too) low intensities of dots at the sea side of the channel due to the gradient in light along the channel.

During the flow reversal, we project the set of dot patterns using a secondary loop. This loop requires a pause between two projections δt_p or it will only project the last pattern from the last iteration.[3] The precise timing between the *plot* command in Matlab and the time of physical projection by the digital projector is not examined. The computational power of the computer is also assumed to influence this timing since the duration of the 15 projections t' fluctuates. In the projection program, a pause of $\delta t_p = 0.075$ seconds is implemented between two projections. The duration of this pause exceeds the frame rate of the camera. In the continuous recordings of the camera, we sometimes find images where one projection is captured in 6 consecutive frames, whereas another projection is only captured within 2 or 3 consecutive frames. Therefore, we remark that the timing between Matlab and the digital projector is not ideal and unnecessary images are being taken. A different projector/camera synchronization is needed, a new projection method could be used where a movie of the set of patterns is continuously playing in repetition. In this project, we chose to work within Matlab and thus accept the 'slower' measurements, and the capturing of unneeded images that require a selection process to extract only the 15 frames of the 15 different projections.

The decision to work within Matlab had also to do with a flaw in long lived experiments. The starting time of the projections started to differ from the moment at which the tide reversed. The tidal motion is controlled by the linear motor that is programmed to finish the oscillatory motion within T seconds. However, the motion control of the motor is not perfect, and the motor performs one tidal cycle in $T + t''$ seconds, where t'' is an offset that varies throughout the experiment. Because of the increasing time difference, the measurements at 0T and 500T are performed at different moments of the tide, and possibly whilst the sediment is still moving.[4] Due to the random delays and presumably the influence of the average water level H_W, changing the resistance on the motor, we implemented a new triggering signal to control the timing of the morphology measurements.

In the final experimental setup, the hardware of the motor is equipped with a triggering output signal. A trigger signal is sent to Matlab when the motor reaches the maximum height. Figure 3.3 shows the imposed position of the bottom level of the piston $H_{\text{piston}}(t)$ over three tidal periods. A continuous motion is obtained when the input of one period is defined by more than 210 data/position points. Decreasing the number of points in the input $H_{\text{piston}}(t)$, results in an impulsive motion of the motor, visualized by small ripples on the water surface. The linear motor is programmed to follow this smooth input but the actual height contains some minor variations in position and time t''. The difference in height is neglected but an asymmetric behaviour is expected due to the difference in buoyancy acting on the piston. During ebb, $\frac{\partial}{\partial t} H_{\text{piston}} > 0$, the movement of the piston aligns with the direction of buoyancy force whereas during flood,

---

[2]Two flow reversals during one tide. i.e. at the transition from ebb to flood $T/2$ and flood to ebb T.

[3]In the recommendations a possible test is mentioned that can check this premise by using an exposure time greater than t'. However, without a pause in Matlab, all 15 *plot* commands can be sent before the frame (rate) of the projector refreshes.

[4]The effect of a difference in water level is still possible due to the changes in bottom morphology that influence the flow field. However, during flow reversal $v \approx 0$ cm/s and a constant H_W is assumed.
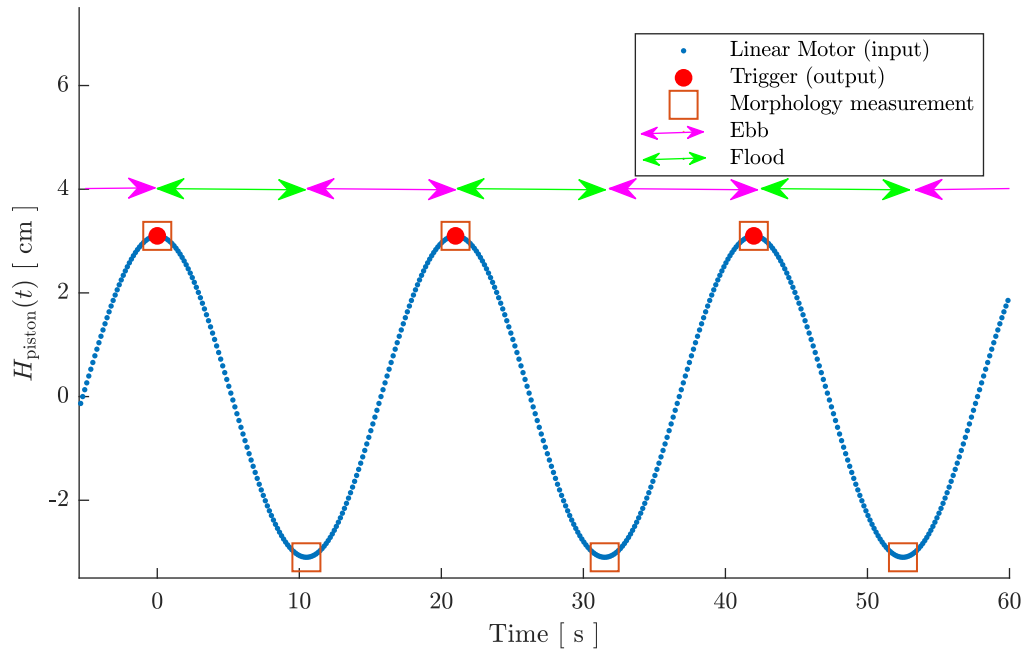

Figure 3.3: Theoretical height profile of the bottom of the piston $H_{\text{piston}}(t)$ connected to the EC-motor. The EC-motor forces the piston to oscillate with an amplitude $\Delta H_{\text{piston}}/2 = 3$ cm and period $T = 21$ seconds. The corresponding tidal motion of H_W has ebb and flood intervals indicated by pink and green arrows, respectively. Moments of maximum $H_{\text{piston}}(t)$ are indicated by red dots and correspond to a minimum water level and visa versa. The trigger moments, represents the transition between ebb to flood. The measurements are performed during flow reversal and are indicated by red squares.

$\frac{\partial}{\partial t}H_{\text{piston}} < 0$, more resistance will be present. The difference in timing t'' is included and controls the start of the measurements.

The $H_{\text{piston}}(t)$ is used to trigger the Matlab projection program after N triggers. If the trigger is detected by Matlab, we pause $\frac{T}{2} - 0.5$ seconds and trigger the LabView application that activates the camera. The LabView application is triggered by Matlab and the continuous recording starts 0.5 seconds before the projections start. This triggering system allows for long lived experiments where there is no shift in time of the measurements. This is not only useful for one single experiment but also to compare different experimental results. Moreover, the moment at which a measurement is performed is defined by the number of tides N and can be chosen freely. It is also possible to perform the measurements during the other flow reversal, during the transition of ebb to flood. By measuring the sediment bed at the transition from flood to ebb, and at the transition from ebb to flow, one can investigate the amount of sediment transported within half a tide.

The volume flux trough the channel can be estimated together with the height variations of the water level using the difference $\Delta H_{\text{piston}} = 6$ cm. The area of the free water surface is given by $A_{\text{tot}} - A_{\text{piston}}$ and consists of the areas of the sea, the tidal channel and the estuary, indicated by A_{sea}, A_{channel} and A_{estuary}, respectively. In this way,

$$
\begin{aligned}
A_{\text{tot}} &= A_{\text{piston}} + A_{\text{sea}} + A_{\text{channel}} + A_{\text{estuary}} \\
&= 1000\,\text{cm}^2 + 7150\,\text{cm}^2 + 1365\,\text{cm}^2 + 5485\,\text{cm}^2 \\
&= 15000\,\text{cm}^2.
\end{aligned}
$$

The change in water level ΔH_W, is the ratio between the volume of the displaced water $\Delta V = A_{\text{piston}} \Delta H_{\text{piston}}$, and the area of the free water surface

$$\Delta H_W = \frac{\Delta V}{A_{\text{tot}} - A_{\text{piston}}} = \frac{\Delta H_{\text{piston}} A_{\text{piston}}}{A_{\text{tot}} - A_{\text{piston}}} = 0.429 \,\text{cm}. \tag{3.1}$$

Note that the assumption of constant equally rising and falling water level depends on T, ΔV and the geometry of the system. The speed at which the information of changes in the water level propagate is given by the wave velocity c. For shallow water, it can be estimated via $c = \sqrt{g \cdot H_W} \approx 100$ cm/s where g is earths gravitational acceleration. The corresponding time scale t_c can be calculated using the maximum length between the piston and back-wall of the estuary: $t_c = l_c/c \approx 2$ seconds. This is small compared to the time scale of the tidal period $T = 21$ seconds, and thus in agreement with our assumption of an equally rising and falling water level in the setup. However, the water level is deformed due to the channel obstructing the flow field and exchange of water between sea and estuary (De Haas 2016). These deformations are visualized by the projected pattern that are reflected of the water surface onto the ceiling. The reflected pattern at the ceiling wobbles revealing the transient deformations in H_W.

Calculations of the total volume flux Q trough the channel and averaged velocity v are only given to estimate the order of magnitude (Wells & van Heijst 2003). The total volumetric discharge trough the channel is given by the fraction of the areas

$$Q \frac{T}{2} = \Delta V \frac{A_{\text{estuary}}}{A_{\text{tot}} - A_{\text{piston}}} = A_{\text{estuary}} \Delta H_W = 2350 \,\text{cm}^3. \tag{3.2}$$

The magnitude of the velocity v can be estimated using

$$A'v = \frac{\Delta V \frac{A_{\text{estuary}}}{A_{\text{tot}} - A_{\text{piston}}}}{\frac{T}{2}}, \tag{3.3}$$

where A' is the cross sectional area of the channel, that depends on $h(x, y)$, H_W and the width of the channel W_{channel}. For a constant cross sectional area of the channel $A' = 125$ cm^2, we find a velocity of $v \approx 3.3$ cm/s.
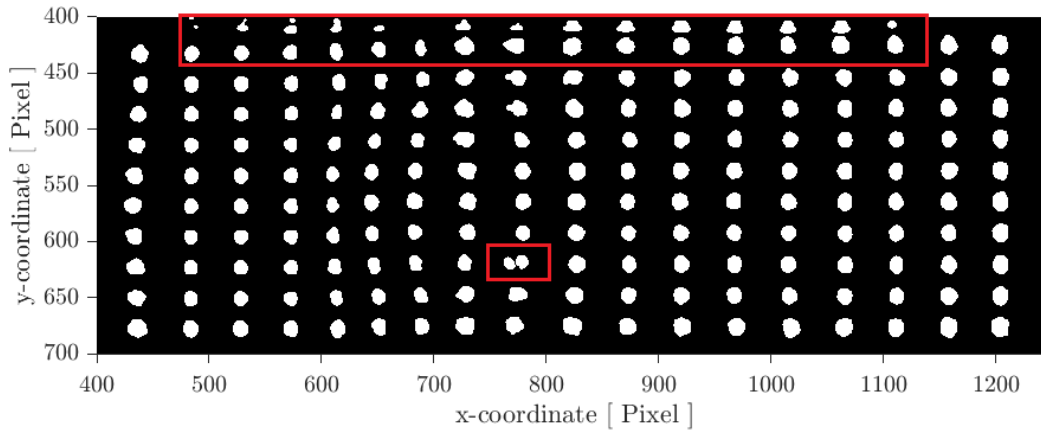
Figure 3.4: Binary filtered image of a dot pattern including reflection of the aluminum barrier indicated by the upper red box. The presence of a floating particle indicated by the lower red box at $(x_p = 768, y_p = 619)$.

False detection of dot position

In section 2.1, an overview was given on the image preprocessing, where the images are converted into binary via an adaptive technique. These binary images are then smoothed and filtered to remove the roughness effects on the dots due to the sediment. From this filtered binary image we locate all white areas via the Matlab function *regionprops*. It is possible that additional white areas are formed that do not represent projected dots. Via additional conditions, using the minor and major axis of the obtained areas, we can remove most of these areas. However, the selection process does not always work correctly.

The most common cause of additional areas in the binary images is the presence of floating (sediment) particles. When such a sediment particle floats underneath a projected dot whilst a picture is taken, it can be seen on the image. The projected dot illuminates two different regions, the sediment bed that is partially illuminated by the light that was not blocked by the floating particle, and the floating particle that is illuminated by the dot. In the current work, these images are not used for the height calculations. The same problem can occur when there are floating patches of PIV particles that cluster together. Before the start of the experiments floating sediment particles are easily sunk by spraying water via a spray bottle. However, it is possible that particles move to the water surface during the experiment. The second cause of additional white areas, is the reflection of light near the channel barriers. These barriers are made out of aluminum strips that reflect (scattered) light onto the sediment bottom. This can cause high light intensity areas in the photographs that are transformed into white areas in the binary images.

An example of a processed binary image is given in figure 3.4. The figure shows a series of reflected dots at $y_p \approx 410$ and a floating particle at $(x_p = 768, y_p = 619)$ indicated by the red squares. The reflection can be removed by reducing the measurement area or introducing a new condition that removes centroids with $y_p < 425$.

3.1.3 Implementation of PIV measurement technique

The morphological measurements are performed during flow reversal whereas PIV measures the velocity field at the water surface during the entire tidal cycle. The measurements are performed simultaneously, which is important when a comparison between the two results is made. When the measurements are performed separately, the obtained velocity field is measured at a different moment than the obtained bed morphology. If the bed has not changed, one can indeed relate the velocity field with the measured bed morphology. However, in some situations the bed morphology does change significantly.

During the calibration of the PIV measurement technique, we searched for a combination of a PIV camera lens & a projection color, in order to remove the projected dot patters in the images obtained with the PIV camera. Such a combination could be used to perform the measurements simultaneously but was not found. However, during this search we found a discontinuity in the illumination of the digital projector. It is this discontinuity that is used to perform both measurements 'simultaneously', i.e. consecutive on a small time scale.

Similar to the work of De Zwart (2017), we use a function generator to send short block pulses to the UV LED lights and PIV camera. The floating tracer particles at the water surface are then illuminated by the UV LED lights and photographed by the PIV double CCD camera. The function generator triggers the UV LED lights and a trigger box that is connected to the PIV camera. The exposure time of the PIV camera is set at 4.5 milliseconds. After this exposure time, the data is copied from the front CCD chip to the second CCD chip, so it can be saved on the computer while acquiring a second image.[5] In current project this feature is tested but not used for the experimental setup since the velocities in the channel did not require such a fast image acquisition. The UV LED lights are activated before the camera is activated and are switched off after the image is taken. The exposure of the CCD of the camera thus completely takes place within the illumination time. The after glow/post exposure emission time of the luminescent particles is small and can be neglected for the triggering time scales discussed here. An UV filter is added on the PIV camera to filter out reflected UV light. The filter also blocks some short wavelengths in the visible spectrum.

In a double recording, were both cameras were recording continuously, we captured the projected dot pattern and PIV tracer particles with both cameras. The projected dot patterns and PIV particles where captured together on the photographs of the PIV camera. However, the illuminated PIV particles had a constant intensity whereas the intensity of the dot patterns varied trough time. The intensity increased and decreased in a periodic manner. This periodic intensity was not found on the images from the camera for morphodynamic measurements. The effect of decreasing intensity is partially explained by the difference in exposure times of the two cameras, and that the PIV setup and projections are not synchronized. Most importantly, there are moments in which the digital projector is not projecting. To investigate this effect we added a light intensity detector (BPW34 sensor) in front of the projector so that the photo diode is completely covered by one single dot. Via the light detector, we measure the intensity of the incoming light as a function of time for different projection colors. Figure 3.5 shows the discontinuity in the projections of the digital projector. The intensities for the primary colors are measured individually and show a step wise illumination for each individual color. When white dots are projected (not shown), each color is projected consecutively. For yellow dots, i.e. green plus red, we identify the two primary colors that are projected consecutively. During the projection of white dots the digital projector is actually projecting blue, green and red dots before pausing $\delta t \approx 3$ milliseconds. The length of the pause between illuminations can be further increased by projecting only primary colors ($\delta t \approx 7$ milliseconds) or the secondary colors yellow and cyan ($\delta t \approx 4.5$ milliseconds). The latter two can be done since they remove the illumination of blue and red, respectively.

Both the PIV tracer particles and projected dots need to have enough contrast in intensity to use the images for the velocity and sediment bed thickness calculations. Increasing the pause by using only a primary color allows longer illumination of the luminescent tracer particles and

---

[5]Single CCD cameras can operate at a fixed maximum number of fps that can not be increased. Double CCD cameras can copy an image to a second (internal) CCD that allows for very fast consecutive image acquisition.
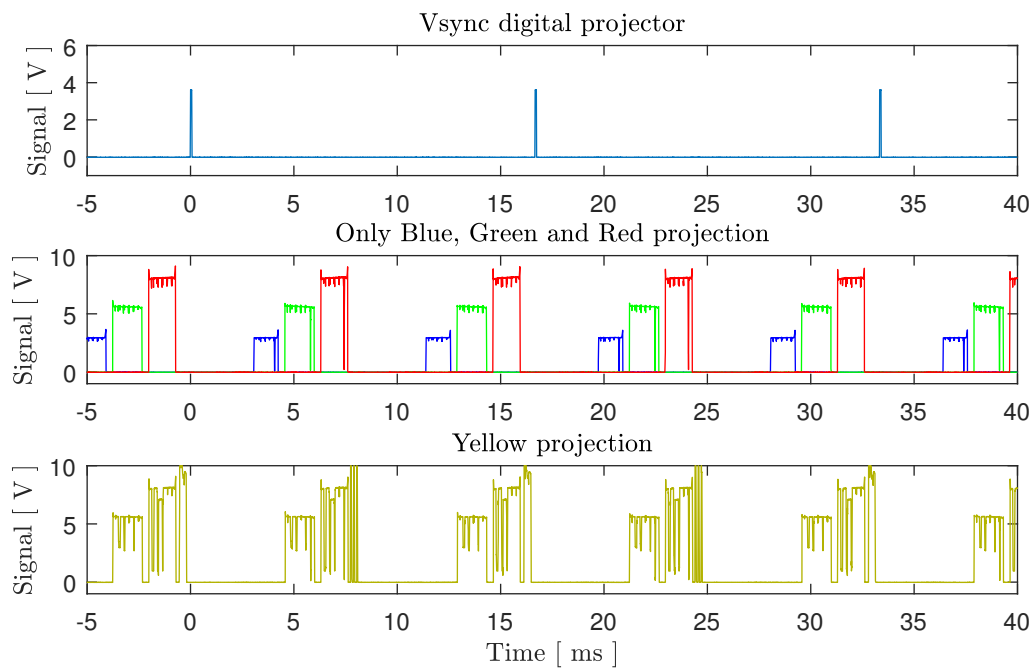
Figure 3.5: Timing of the digital projector. The Vsync (60 fps) is measured by the function generator and a light intensity meter is used to measure the illumination of the digital projector. First, the three primary colors are projected individually and are presented together with the measured intensity of a yellow projection. The projected secondary color yellow shows the illumination of the primary colors green and red that are projected consecutively. The measurement time is defined via the Vsync and show a pause δt in the illumination of the digital projector of 3 and 4.5 milliseconds for white and yellow projections respectively.

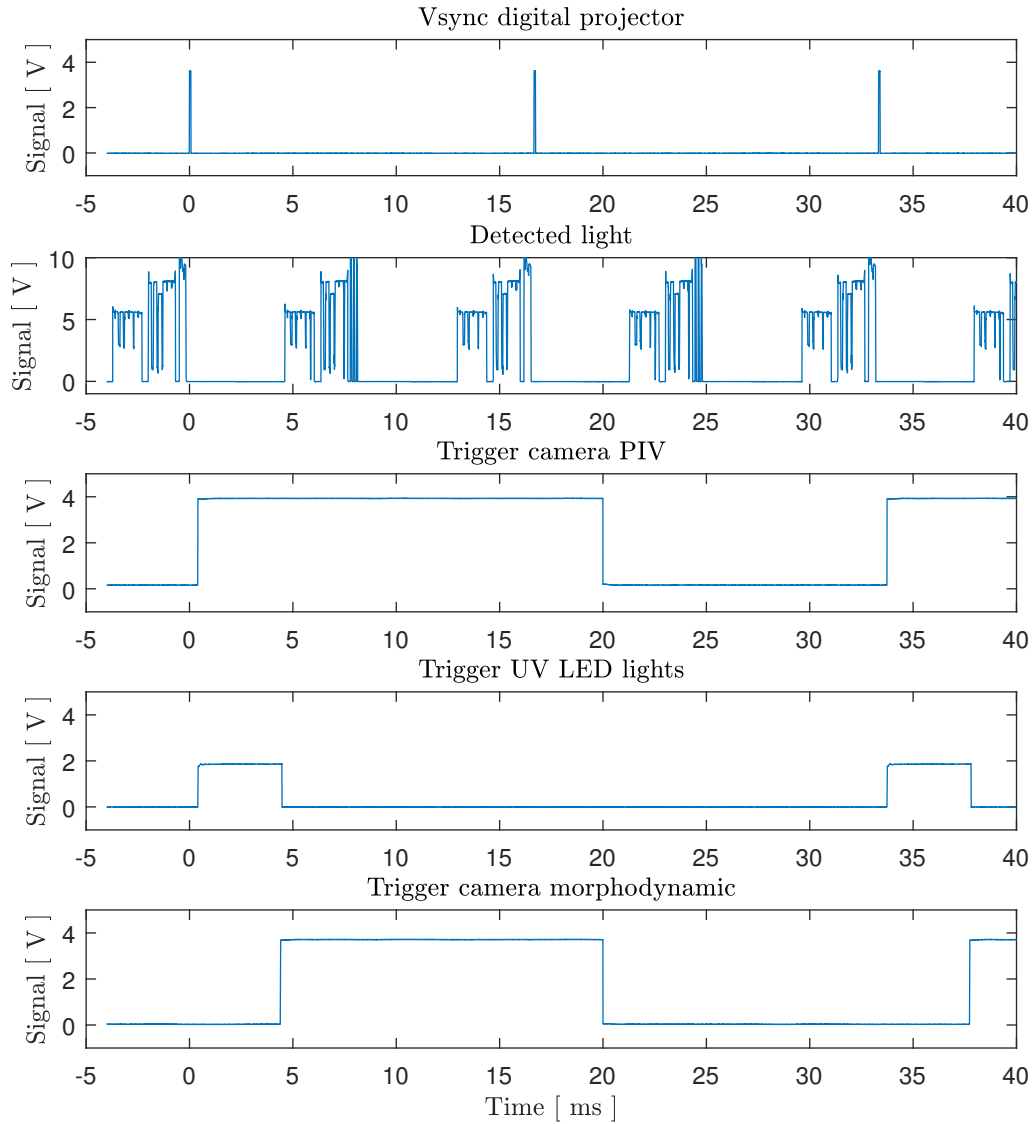Figure 3.6: Timing of the digital projector, UV LED lights and both cameras. The measured Vsync (60 fps) of the digital projector defines the timing of the measurements. The projection of a yellow dot pattern is measured and shows the discontinuous illumination of the digital projector. During the moments where the digital projector is not projecting, the PIV camera and UV LED lights are triggered. The exposure time of the PIV camera is set to 4.5 milliseconds during which the UV LED lights are activated. The camera used for morphodynamic measurements is triggered after the UV LED lights are deactivated, the exposure time of this camera is set to 15 milliseconds, capturing two consecutive projections of the same dot pattern. The trigger signals of the cameras (operating at 30 fps) are extended to leave out a Vsync pulse and forcing the system to operate at 30 fps.

thus gain more contrast. The downside of only projecting a single primary color is the decreasing contrast of the projected patterns in the images for the morphology measurements. The optimal combination is the 4.5 milliseconds pause for projecting yellow dots, since they provide the largest contrast with the sediment.

Figure 3.5 also shows the vertical sync (Vsync) of the digital projector. The signal is obtained from the VGA female DE15 socked (Pin 15) of the digital projector and gives the frame rate of the digital projector. Note that there are two illuminations for each Vsync. Therefore, the projector has a projection rate of 120 fps. It is assumed that the projected image can only change after a Vsync (60 fps). Therefore, the vertical sync is used to define the timing of both cameras and the UV LED lights.

In figure 3.6 a complete overview is given of the triggering of both cameras and the UV LED lights. When the Vsync is measured, the function generator sends two block pulses to the trigger box connected to the PIV camera and the power supply of the UV LED lights. The UV LED lights are activated for 4.7 milliseconds overlapping the exposure time of the PIV camera (4.5 milliseconds). The pulse for the PIV camera is extended beyond the next Vsync. The maximum frame rate of the camera used to measure the morphodynamics is 30 fps. By extending the block pulses for both cameras, one measured Vsync gets skipped and the total measurement is forced to operate at 30 fps. The duration of the pulse is not relevant for the activation of the PIV camera since it gets activated by the trigger box if the measured signal (rising edge of block signal) reaches a threshold of 3 V. The triggering of the camera for morphodynamic measurements is similar since it gets activated at a different moment but when a threshold of 3 V is measured. Using the current triggering system it is possible to increase the exposure time of the camera to a maximum where 4 illuminations are captured, e.g. from 5 to 33 milliseconds, shown in figure 3.6. However, similar contrast is found when the exposure time is less than 15 milliseconds. When the exposure time exceeds 15 seconds, it is possible that the projection program of the digital projector changed the projected pattern during image acquisition. When this happens during the exposure of the CCD of the camera, two consecutive projections are measured in one image. Therefore, the maximum exposure time of the camera for morphology measurements is set to 14 milliseconds.
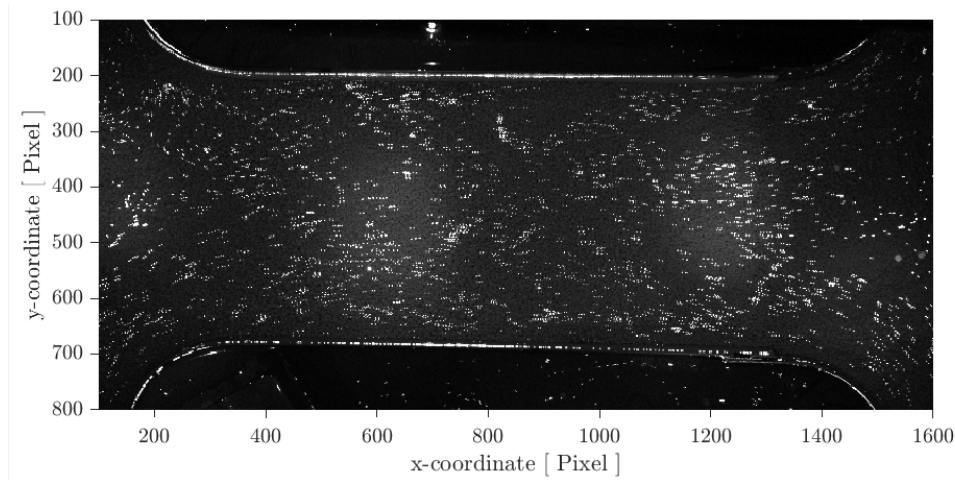
Figure 3.7: Photograph pair of the displaced luminescent tracer particles. The moving sediment bed is also captured at the direct regions below the UV LED lights. Any motion in the sediment bed will influence the PIV result and the background is removed.

Particle Image Velocimetry using PIVview3C

The PIV calculations are performed with the program PIVview3C, which uses an image pair of consecutive images of the tracer particles and measures their displacement. In this subsection we discuss the illumination of the luminescent tracer particles together with the image preprocessing which is needed to correctly calculate the velocities of the tracer particles. The images of the PIV particles contain the positions of the floating luminescent particles. There are three aspects of the photographed PIV particles that presumably influence the resemblance between the measured velocity field and the tidal velocity: the similarity between particle motion and fluid motion, the measured velocity at the air-water interface is located between two boundary layers, and the changing water level height during the tide differs from the constant height at which the PIV camera is calibrated.

The floating luminescent tracer particles are white polyethylene micro-spheres coated with tween-80. During long periods of downtime, e.g. during night, the particles would still form patches and accumulate at the side walls of the tank as a result of the Cheerios effect. These particles patches are easily redistributed by hand before the measurements are performed. The shape, size and density of the particles are chosen so that the response time t_0 of the particles compared to the motion of the fluid is reasonably short to accurately follow the flow. Secondly, the size of the particles has to be large enough for detection and small enough to not block the projected patterns. The response time of the spherical particles ($t_0 = 2.163 \times 10^{-7}$ seconds) defines the Stokes number $\text{Stk} = t_0 u_0 / l_0$ where $u_0 = \mathcal{O}(1)$ is the order of the fluid velocity and $l_0 = \mathcal{O}(1)$ the typical order of length scale in centimeters. The order of Stk is $\mathcal{O}(10^{-7})$ and validates the assumption that the particles faithfully follow the flow.

The measured velocity field corresponds to the velocity of the PIV tracer particles at the oscillating free water surface. Since the free surface is the interface between air and water, there is a boundary layer in both media. Because the PIV particles are on top of the water boundary layer, one should remember this effect when looking at the obtained velocity fields. For the conditions in this project the boundary layer can be neglected, since the air is assumed to move accordingly (Raffel *et al.* 2018). Furthermore, the PIV camera is calibrated for a certain horizontal level H_W where the relation between pixel coordinates and real world coordinates is determined via a calibration, similar to the camera calibration of the photogrammetry given by equations (2.28) and (2.29). The changes in the water level during the tide are $\Delta H_{W,max} \approx 0.43$ cm, and are not
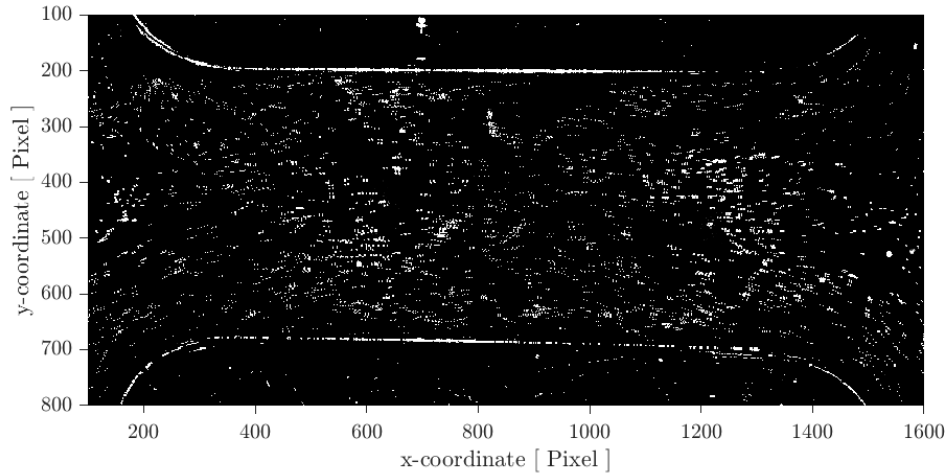
Figure 3.8: Processed image pair of the moving luminescent tracer particles. In PIVview3C a mask is added to remove the regions outside the channel and to remove the channel walls.

measured but can be neglected. This variation is significant with respect to the variations in H_W during flow reversal. However, if we use a constant pixel to real world relation, the maximum error on v is 0.2375% and is neglected.[6]

An exposure time of 4.5 milliseconds is used since this gives a clear contrast between the luminescent tracer particles and the surrounding (De Zwart 2017). The intensity of the tracer particles can be enhanced by increasing the exposure time or by adding more UV light by increasing the voltage on each UV LED light or increasing the number of UV LED lights. Due to the illumination time of the digital projector, only the voltage and number of UV LED lights can be varied. The diodes emit some wavelengths in the visible spectrum that are not blocked by the UV filter on the PIV camera. Near the centre of the channel at $x_p \approx 650$ and at $x_p \approx 1250$ the sediment bed is captured by the PIV camera. Due to the working principle of PIV, changing backgrounds need to be removed since it contains movement of the illuminated sediment, which is not related to the movement of the tracer particles. The photograph pair of figure 3.7 is preprocessed into 3.8 before used in PIVview3C.

The image pairs of the tracer particles are processed and shown in figure 3.8, where the illuminated sediment bed is removed. The basic principle of PIV is that the image get divided into interrogation windows, named correlation boxes in PIVview3C. The interrogation windows from each image pair are then cross-correlated with each other, pixel by pixel. From this correlation it is possible to determine the average particle displacement X and find the average velocity X/t where t is the time between the images, $t = 0.033$ seconds. A velocity map over the whole target area is obtained by repeating the cross-correlation for each interrogation window for each of the image pairs captured by the camera (Raffel *et al.* (2018) and **PIVView**). Via grid refinement, we can decrease the size of the correlation boxes. Therefore, a new velocity fields with a higher spatial resolution is obtained. The starting grid are boxes of 256 pixel × 256 pixel and decreases until a too low number of correlation points are determined: less than five particles per box or when the size of the correlation window is smaller than the displacement. The minimum size of correlation boxes is 64 pixels × 64 pixels and the overlapping between the windows is set to 25%. The density of tracer particles on the water surface is thus one of the conditions that defines the spatial resolution of the measured velocity field.

---

[6]For an angle $\alpha = 10°$, $\Delta H_W = 0.4$ cm and displacement of $L = v \cdot 1/30 = 3.3/30 = 0.11$ cm, one can calculate the error of the magnification effect that is $\epsilon = 2.375 \cdot 10^{-3}$ cm.

Summary of the experimental setup

Before the results are presented, we briefly summarize the morphology and PIV measurement techniques and the corresponding timing. A schematic overview is given in figure 3.9, where the main components are indicated together with the most important connections between these components. Via the numbers ① to ⑥, we chronologically describe the controls and triggers used to perform PIV and morphology measurements. The computer is the central component to which the EC-motor, digital projector and cameras are connected. It controls the oscillatory motion of the EC-motor and piston using LinMot Talk ①. The height of the piston is monitored and an output trigger is sent when the piston reaches its maximum height ②. The Matlab projection program is triggered by this signal and activates the projection of the dot patterns ③. The digital projector starts projecting the dot patterns onto the sediment bed during flow reversal ④. The Vsync of the digital projector is measured via the oscilloscope and is used to sent two signals using the function generator ④. The first signal ⑤ is sent to the power supply of the UV LED lights and trigger box of the PIV camera. The second signal ⑥ is directly sent to the morphology camera. Via a LabView application both cameras are monitored and only record when the LabView application is activated, i.e. LabView sets the cameras on standby before ③. When the cameras are on stand by whilst being triggered, they make a single photograph. The cameras are put on standby after the N periods, right before the 15 different patterns are being projected. Therefore, both cameras are on standby during the set of projections but only make a photograph when the external triggers are received ⑤ and ⑥.
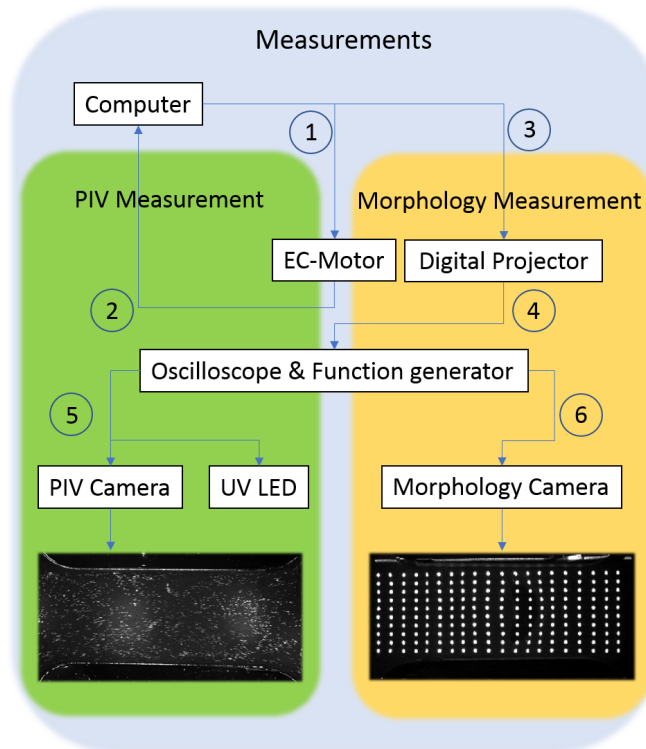
Figure 3.9: Schematic overview of components and connections/triggers used in PIV and morphology measurements. ① LinMot Talk controlling the EC-motor, ② EC-motor triggering the Matlab projection program, ③ projection program operating the digital projector, ④ illumination of projections at frame rate Vsync, ⑤ function generator sending trigger pulses to UV LED lights and trigger box that activates the PIV camera, ⑥ function generation sending trigger to morphology camera.

3.2   Results

The final bed thickness calculations are performed with the photogrammetric technique since it is the most complete. The height calculations of the horizontal plates provided an accurate reconstruction of the measured surface for dry and underwater measurements, $\epsilon < 0.05$ cm. Note that these underwater measurements are performed in a stagnant layer of water. During the morphology measurements inside a tidal channel, we perform the measurements trough a moving water level. The influence of possible height variations in H_W during the measurement are discussed in section 3.2.1. One possible effect is the difference between the defined H_W, measured under stagnant conditions, and the actual H_W during the measurement. Secondly, the effect of a deformed/inclined water level changing the refraction.

We also performed set of PIV measurements where the effect of H_W on the tidal velocities are measured for different water levels. The symmetry of the tides and duration of ebb and flood are compared to see if and how they depend on H_W. These results are given in section 3.2.2. In section 3.2.3, we present the results of the final measurements of the transient bed morphology and measured velocity field.

3.2.1   Effect of the changes in the water level during the morphological measurements

The maximum morphological measurement duration is 2.1 seconds in which the 15 dot patterns are projected onto the underwater sediment bed and captured by the camera. In the bed thickness calculations, including the calculation of refraction, we assumed that the water level is horizontal and the height does not vary in position and time during the measurement. A comparison is made between the calculated $h_{\mathrm{flowreversal}}(x, y)$, measured during flow reversal, and the calculated $h_{\mathrm{stationary}}(x, y)$ measured in the (dry/) stationary situation, to see possible variations that contradict our assumption of a constant H_W. The magnitude of the variations in H_W are expected to be small, but during the early test measurements, we found a significant effect in the height calculations $\epsilon \approx 0.15$ cm. In absence of the synchronization of the digital projector and linear motor, together with the regular order of projections, a periodic 'error' was found on the calculated heights. Therefore, we implemented the synchronization and changed the order of the projections; see section 3.1.2 and section 2.1, respectively. These two aspects removed the error. However, we do know that their are smaller water level variations due to the wobbling refracted dot pattern on the ceiling, that visualises these variations.

Due to practical limitations, it is not possible to measure the water level directly inside the channel during flow reversal. The height of the water level is always measured at the sea side near the inlet of the channel in stagnant water, i.e. when the piston is at rest, positioned at $H_{\mathrm{piston}} = 0$ cm.[7] The water level is measured via a caliper, which contains a small offset in measured height due to capillary wetting. Throughout the project, we actually measured the contact point of the liquid and solid, which differs from the actual water level H_W. The measurements of this contact point have an accuracy of 0.05 cm. The offset due to capillary wetting is neglected since it is assumed to be constant for all measurements of the water level.

We do not directly measure the magnitude of the difference between measured H_W in stagnant water and actual H_W in the channel during the morphological measurements. We measured the influence of the water level difference on the bed morphology calculations. If the horizontal bottom of the channel is measured in the absence of sediment, we find the magnitude in variations in h due to the changes in H_W.

Two tests are performed where the height of the bottom is measured ($h = 0$ cm) for different water levels, during flow reversal or during a stationary situation. First, a comparison between flow reversal and stagnant water is made where $H_W = 6.28$ cm in both cases as measured in stagnant conditions. Note that the measured variations in h also contain the possible influence of a deformed water level that is not present in stationary conditions. The latter effect can be

---

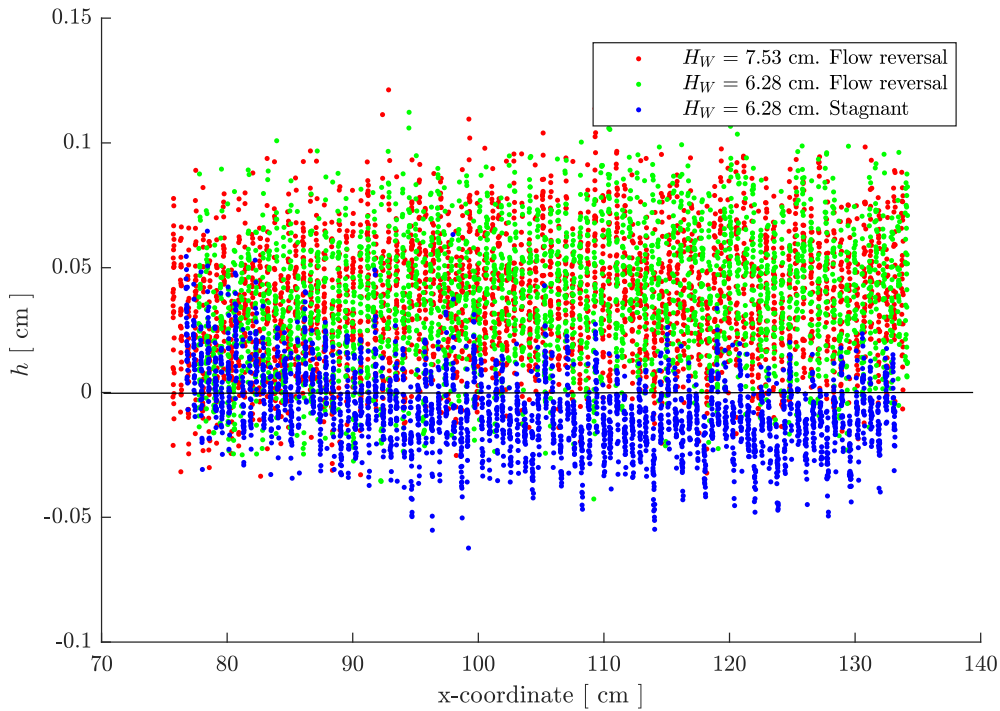[7]The measurement location is indicated by ⑫ in figure 3.2.

Figure 3.10: Height calculations of the bottom $z = 0$ cm of the channel cm during flow reversal (red and green) and stagnant water (blue). The magnitude of the noise in stagnant conditions is smallest and the measurements during flow reversal contain some under prediction at $x = 80$ cm.

estimated by measuring the bed morphology during two flow reversals for $H_W = 7.53$ cm and $H_W = 6.28$ cm. When we assume that the only difference between these situations is the height of the water level in the channel ($7.53 - 6.28 = 1.25$ cm), we can estimate the magnitude of this effect.

The differences in the obtained h are shown in figure 3.10, where the red and green points indicate the calculated surface during flow reversal for $H_W = 7.53$ cm and 6.28 cm, respectively. The reconstruction of the bottom plate in stagnant water is indicated by the blue dots with $H_W = 6.28$ cm. From these height calculations, we can conclude that the measurements during flow reversal differ from the height calculations in stationary water. The level of scatter increases and an offset of 0.05 cm is found over the entire length of the channel, corresponding to an incorrect input of H_W in the height calculations. The magnitude of the scatter in height is less than 0.05 cm for these particular conditions. The level of scatter in the stagnant water measurements is smallest and only a small over prediction of h is found around $x = 80$ cm. Due to the level of noise that is two times larger than the noise in stagnant calculations, we conclude that there are small deformations in the water surface that increase the error on h by 0.05 cm. Moreover, the measured water level in stagnant conditions does not correspond to the actual height of H_W during the measurement. The correction for this offset can be investigated and is most likely a constant correction on H_W. These findings are not studied thoroughly, and more measurements are required to optimize and to find the actual water level during the measurement. A possible improvement is to measure the reflected dots from the free water surface on a screen. After calibration, these dot reflections can be used to acquire the height of the free water surface at which the projected dots are reflected using triangulation. Another non-intrusive stagnant water level measurement is also recommended where a single dot is projected onto an underwater reference height. The refracted dot position captured by the camera can then be used to evaluate the water level.

3.2.2 Influence of the water level on tidal velocity

During the morphology experiments, discussed in section 3.2.3, a sediment bed of $h = 2$ cm is added on the bottom of the tidal channel. Therefore, a measured water level of $H_W = 7$ cm corresponds to an actual water layer of $H_W - h = 5$ cm above the sediment bed. In this section, we present the velocity fields that are measured in the absence of sediment to study the relation between the water level and the (tidal) velocity field. The velocity fields are measured at the free surface inside the channel using the un-synchronized PIV measurement setup, i.e. without the timing from the EC-motor and camera.[8] This makes it more difficult to draw conclusions from the obtained results between the different PIV measurements. However, some conclusions and insights can be made, like the duration of the tides and the magnitude of the tidal velocity. The timing of the measurements is an experimentally obtained time and is defined when the averaged velocity is equal to 0 cm/s, measured at $x = 105$ cm.

The influence of the water level H_W on the magnitude of the tidal velocity is shown in figure 3.11, where the water level is increased in steps from 5 cm to 7.5 cm. The averaged tidal velocity at the centre of the channel is periodic, with $T = 21$ seconds for all water levels. The flood period here is indicated by $0 < t < 9.15$ seconds, and the ebb period during $9.15 < t < 21$ seconds. Due to the definition of $t = 0$ seconds, each curve is not defined precisely in time and might need a translation in time. The maximum magnitude of $v(t)$ is measured during flood for water levels above 5.5 cm. The magnitude of v depends on the water level, which is related to the cross-sectional area of the channel that depends on H_W. Because the same amount of volume is being displaced by the piston, the magnitudes of the velocity $v(t)$ increase for decreasing water levels. The measured asymmetry in the magnitude of tidal velocity and duration of ebb-flood, are specific characteristics for the used tidal setup. The influence of the back wall of the tank at $x = 50$ cm, is obstructing the flow. The channel barriers only leave two openings of 15 cm to the semi-enclosed basin. The influence of the size of these openings on the flow was only investigated in a low water situation $H_W = 5$ cm using colored dye measurements. From the obtained PIV measurements, shown in figure 3.11, we do indeed find a symmetry for the tidal velocity with $H_W = 5$ cm. However, the symmetry does not hold for increasing water levels.

PIV measurements with $H_W = 5$ cm are performed multiple times to check the reproduciblility of the measured symmetric velocity field. We obtained the same velocity field from these additional measurements. The sizes of the interrogation windows in PIVview3C are increased to check if they are too small due to higher velocities. These new velocity fields, with lower spatial resolution, were the same and thus this measurement is considered valid.

A converging averaged asymmetric velocity profile is found for high water levels, i.e. $H_W > 6.75$ cm, where the magnitudes of the maximum velocities are asymmetric $v_{\text{ebb}} < v_{\text{flood}}$. This asymmetry is commonly found in nature (see e.g. Dronkers 1986). The tidal asymmetry can be related to the net sediment transport inside a system.

---

[8]This set of experiments was performed before the synchronization is implemented.
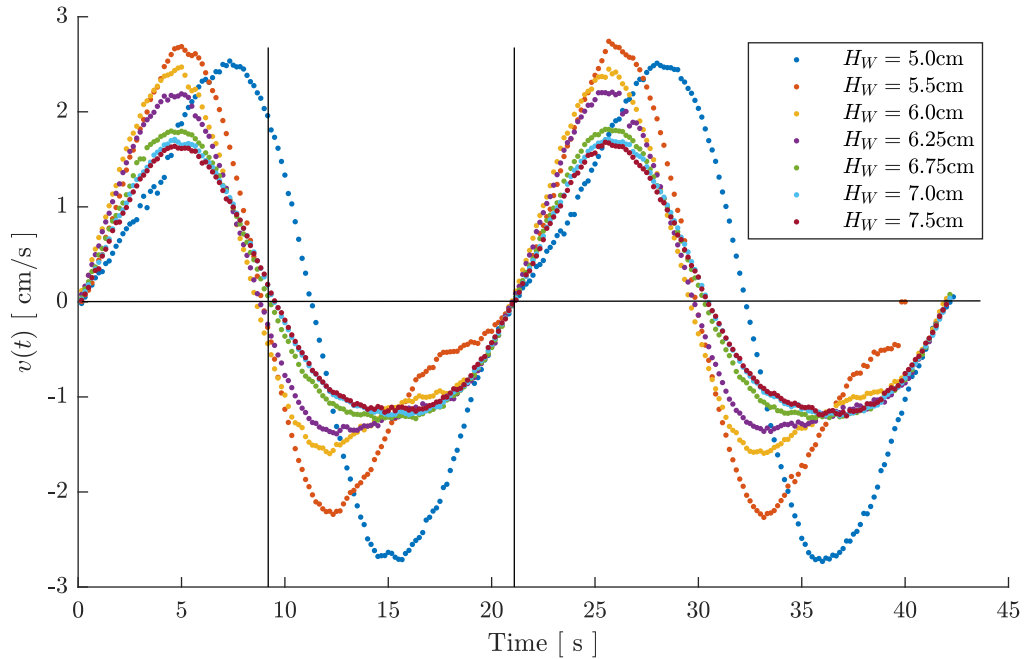
Figure 3.11: The measured averaged velocity $v(t)$ at the centre of the tidal channel at $x = 105$ cm. The water level H_W is varied to see its response/influence on the magnitude and profile of $v(t)$. The time scale is experimentally obtained at moments where $v(t) = 0$ cm/s. The tides are composed of a flood interval ($0 < t < 9.15$ seconds) and an ebb interval ($9.15 < t < 21$ seconds). For a water level of $H_W = 5$ cm we find a more symmetric tide with a duration of flood and ebb 10.8 and 10.2 seconds, respectively.

3.2.3 Transient bed morphology in a tidal channel

The results of the morphological measurements of the transient sediment bed, together with the results of the PIV measurements of the velocity field, are presented in this section. The sediment bed is flattened at $z = 2$ cm by carefully scraping the sediment layer with a rigid horizontal bar over the two barriers at the edges of the sediment domain. This is done to control the initial volume of sediment inside the tidal channel. The bed is then perturbed to investigate the evolution of these perturbations in time. The transient sediment bed $h(x, y, t)$ inside the channel is measured over 500 tidal periods. Two consecutive morphological measurements are performed after $N = 5$ periods, to measure the sediment bed thickness during the two flow reversals in one tide. The first measurement measures the bed thickness during the transition from flood to ebb and the second during the transition from ebb to flood. The changes in the bed morphology during the ebb phase can then be illustrated in erosion-deposition maps. The measured sediment bed thickness of the initial condition $h(x, y, t = 0)$, is given in figure 3.12, where the underwater measurement is performed for a water level of $H_W = 7.61$ cm.

The measured bed thickness $h(x, y, t = 0)$ is represented by two surfaces. First, we show all the 3000 measurement locations indicated by blue points. In the lower figure, we show a contour plot of measured data, obtained via second order polynomial interpolation. The interpolation is required since the (x, y) coordinates of the measured locations are variable, while a mesh-grid is needed to fit the bed thickness. The initial bed consists of one small and two larger sediment patches. The small patch is initially located at $x = 85$ cm near the entrance of the channel to the semi-enclosed basin. The two larger perturbations are initially located around $x = 110$ cm and $x = 130$ cm.
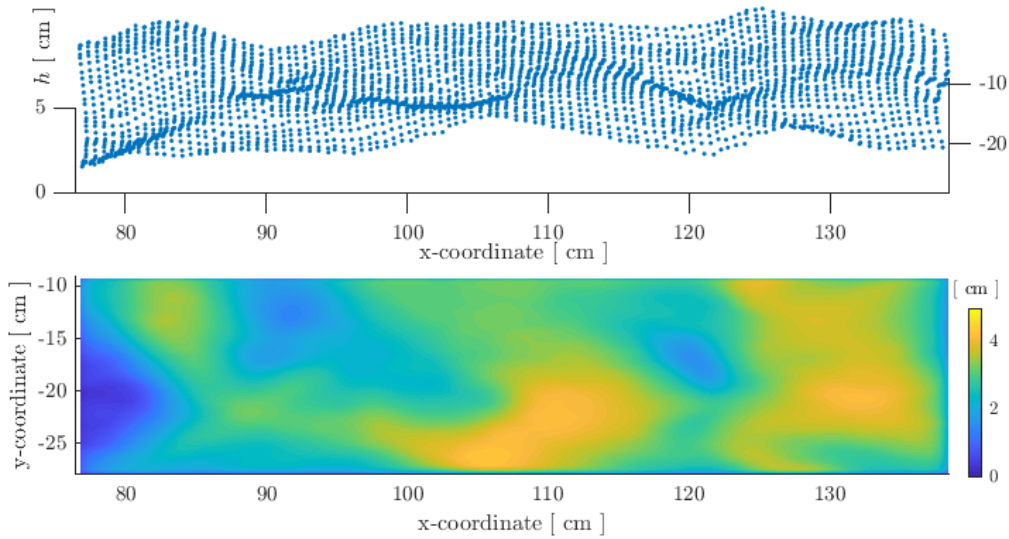
Figure 3.12: Measured bed thickness $h(x, y, t = 0)$ at the beginning of the experiment. The initial bed morphology is a random perturbed bed that is measured over time to investigate the evolution of the perturbations. The 3000 measurement points of the surface are indicated by blue dots in the upper sub figure. A contour map of the bed is given and indicates the height of the sediment.

The photogrammetric measurements of sediment bed thickness are shown in figure 3.13. The sediment patch initially located at $x = 110$ cm, migrates into the negative $x-$direction towards the semi-enclosed basin. The patch is initially located at one side of the channel $(-29 < y < -18)$ cm, but grows into the complete width of the channel $(-29 < y < -9)$ cm within 150 tidal periods. In literature, the denomination of these structures varies (a complete classification of sub-aqueous sediment structures is presented by Carling 1999). In another experimental study by Stefanon *et al.* (2010), similar scaled bed morphologies are observed in tidal channels and are addressed as dunes. In this work, we follow this convention and identify these perturbation as dunes. The migration speed of the dune is constant during the duration of the measurement and approximately $6.5 \ 10^{-5}$ cm/s or 0.0137 cm/T. These migration rates are calculated via the steep lee slope of the dune (Knaapen & Hulscher (2002) and Barnard *et al.* (2013)). The contour maps show a possible formation of a second dune, from the perturbation initially located at $x = 130$ cm. This sediment patch, located near the channel entrance with the sea, also grows in height and width over time and moves in the negative $x-$direction. In the final measurement, at $t = 500T$, we see that this patch almost separates with the bed to form a second dune.

The erosion and deposition maps are shown in figure 3.14, where blue and yellow regions correspond to erosion and deposition of sediment, respectively. These maps quantify the bed load transport during half a tide. From these maps we see a shift in the regions of erosion and deposition. We find deposition at the lee and stoss sides of the dune during half a tide. The top of the dune is being eroded together with the area between initial perturbations. This area or trough also grows in size and deepens over time. After 200 periods this trough reaches the bottom plate of the experimental setup $z = 0$ cm, changing the bed load transport in these areas.

Due to the presence of the dune, the sediment bed next to the lee side is eroded. From the erosion-deposition maps, we see that this sediment is deposited onto the growing dune. When the dune approaches the small perturbation, initially located at $x = 85$ cm, the entire patch gets eroded. Note that this perturbation did not form a dune and was stable until the dune approaches it after 250 periods. The height and location of the perturbation are important conditions for the formation and growth of dunes.
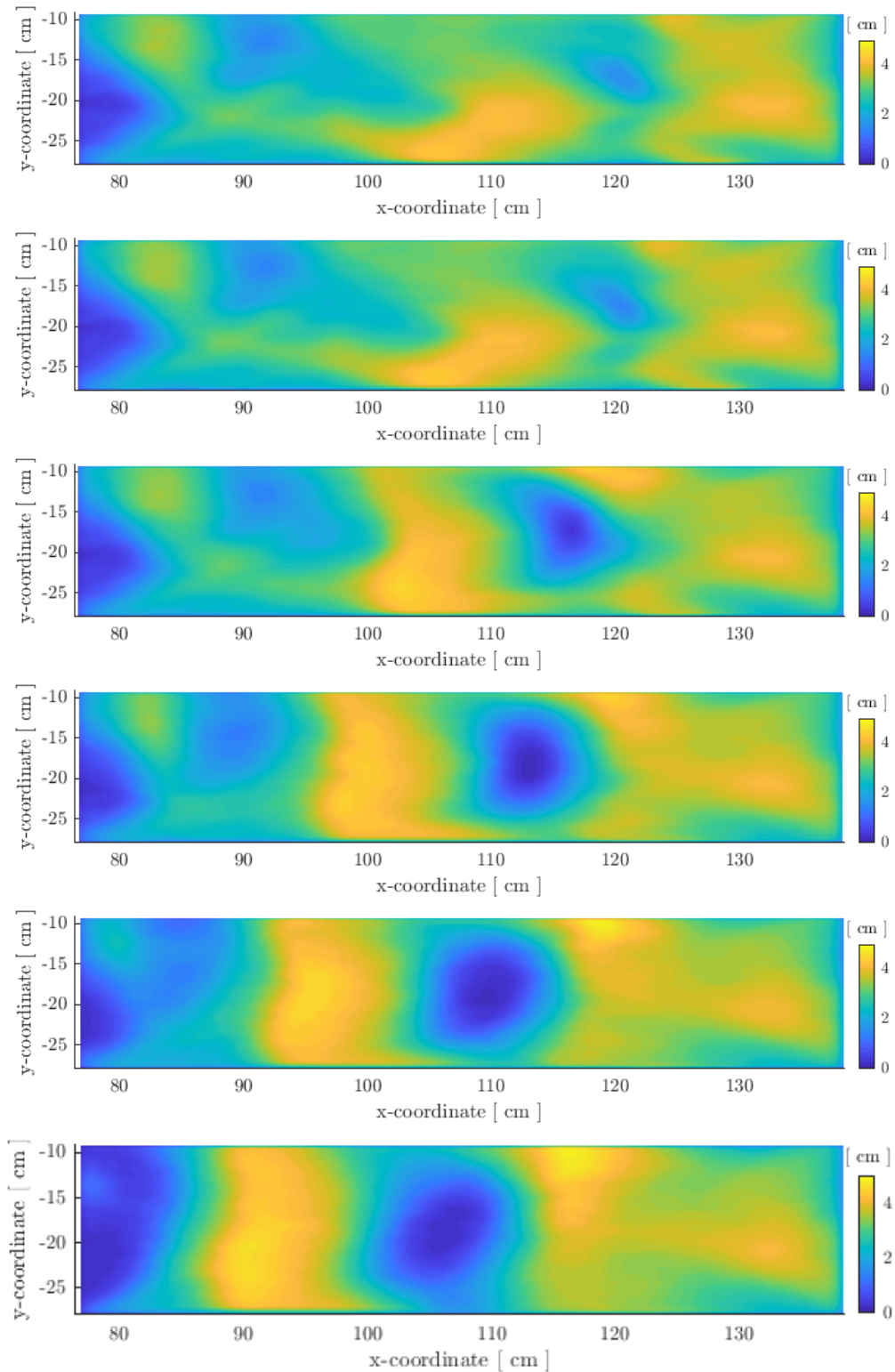
Figure 3.13: The contour maps of the transient bed morphology show the migration and growth of the initial perturbations. The measurements are taken during the transition from flood to ebb at $t = 0T$, $5T$, $125T$, $250T$, $375T$ and $500T$. The perturbation covers the entire width of the channel after 200 periods. The trough of the sediment patch reached the bottom at $t = 250T$ changing the bed load transport at $z = 0$ cm.
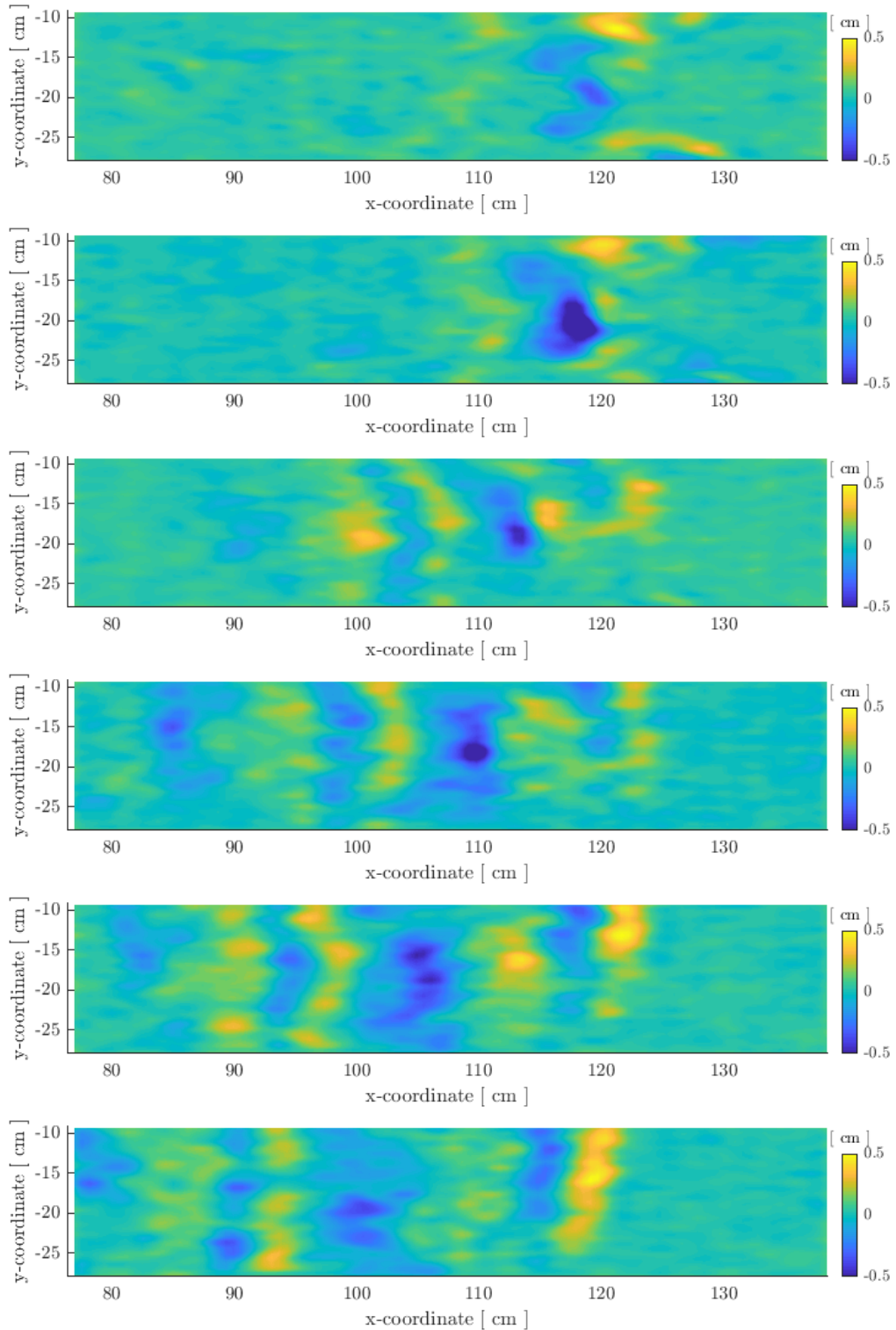
Figure 3.14: Erosion and deposition areas measured between the transitions from flood to ebb and ebb to flood at $t = 0T$, $5T$, $125T$, $250T$, $375T$ and $500T$. The yellow areas indicate areas of an increase in height (accumulation) whereas the blue areas indicate regions of a decrease in height (erosion).
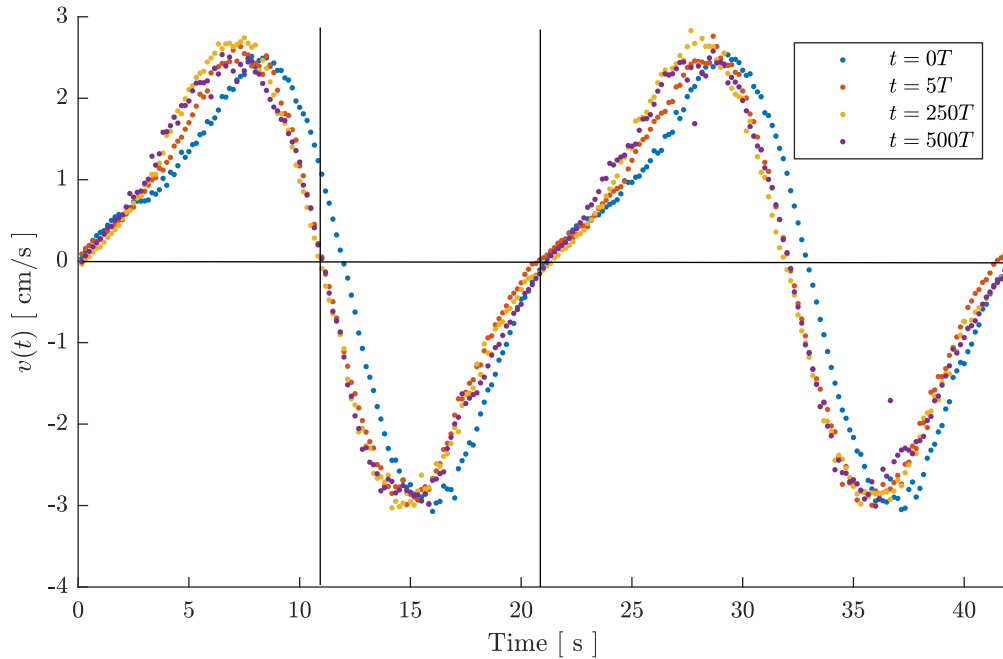
Figure 3.15: Averaged velocity $v(t)$ inside the channel measured at $x = 105$ cm. The measurements are taken at $t = 0T$, $5T$, $250T$ and $500T$.

After the initial conditions, the system changes from a stagnant into a 'sloshing' tidal system. Therefore, changing the bed morphology and velocity field during the first tides. Especially the bed can vary significantly due to the unstable and unnatural formation of the sediment patches where the sediment bed is not packed. From the measurements at $t = 0T$ and $t = 5T$, we see that there are no large variations in the bed morphology for the initial perturbations. However, in other tests, we found significant effects in over the first few periods when an 'unstable' initial morphological bed is chosen. Also the erosion-deposition maps do show a large difference, confirming an unstable initial condition.

The PIV measurements are performed at $t = 0T$, $5T$, $250T$ and $500T$, to measure the tidal velocity field at the water surface during different moments of the experiment. The averaged magnitude of the tidal velocity at $x = 105$ cm is shown in figure 3.15. From this measured velocity signal, we see an asymmetry between the magnitude and duration of the flood and the ebb phase. The duration of the tide is 21 seconds, with flood and ebb lasting 11 and 10 seconds, respectively. The magnitude of the tidal velocity during flood is 2.8 cm/s, while during ebb we have measured a tidal velocity of -3.0 cm/s. This velocity is compared with the averaged measured velocity with $H_W = 5$ cm in the absence of sediment, shown in figure 3.11. Note that the difference in the magnitude of the velocity is in agreement with the duration of the phases, so that the net volumetric discharge of water is zero. The dominating transport is bed-load transport. Because we have a shallow water layer in which the sediment grains settle in maximum 2 seconds, we neglect the settling lag for suspended sediment transport. This effect is the result of the longer tidal phase in which sediment has more time to settle to the bottom, while during the other phase this time interval is shorter, leading to less deposition. Note that this effect would not be in agreement with the direction in which the dunes migrate and direction of sediment transport.

In this project, the magnitude of the tidal velocity seems to be the governing factor for bed-load transport. The critical shield parameter is reached in both tidal phases, but because the velocity during the ebb phase is dominating, a larger shear stress at the bottom is expected, increasing the

erosion during the ebb phase into the negative $x-$direction. The duration of in the tidal intervals in which the shields parameter is larger than the critical value, also depend on the duration of the tidal phase. The critical shields parameter and the duration of the intervals where $v(t) > v_{\text{critical}}$ are not investigated here.

Finally, we remark that the sediment transport is influenced by standing vortices, that do not reach the water surface and are not measured by PIV. They can be found during the flow reversal in between two dunes and strongly influence the sediment transport.

An overview of the measured velocity fields is given in figure 3.16, where the velocity and corresponding vorticity fields are shown at $t = 0T$, $5T$, $250T$ and $500T$. The results of these PIV measurements show the velocity field of the flow reversals at the time of a morphology measurements. From the vorticity maps, we can see an increasing vorticity region around $x = 113$ cm. At this location, there is initially a maximum height in the sediment bed at $t = 0T$ and $t = 5T$. From the maps at $t = 250T$ and $t = 500T$, the position of highest vorticity is around $x = 110$ cm where the height of the sediment bed is minimal. Therefore, the positions of these strong vorticity do not align with the position of the (migrated) dune. To compare the velocity and vorticity field with the tidal flow without sediment, we show the measured field for $H_W = 5.0$, 6.25 and 7.5 cm in figure 3.17. From these measurements, it is clear that the high vorticity regions at the water surface are residual flow structures from the lateral boundary layer of previous tide. This boundary layer is rolled up forming a dipolar structure at the outlet of the channel, which is been sucked back into the channel after the flow reversal (see Wells & van Heijst 2003, for a detailed description of the process). The magnitude of these vorticity cells are expected to decrease in strength for increasing water levels, as found during the measurements without sediment. Figure 3.17 shows the measured vorticity and velocity during the flow reversal for three different water levels $H_W = 5.0$, 6.25 and 7.5 cm. The decreasing magnitude of the velocity field shown in figure 3.17 also shows that the dipolar structure is not being transported as far.
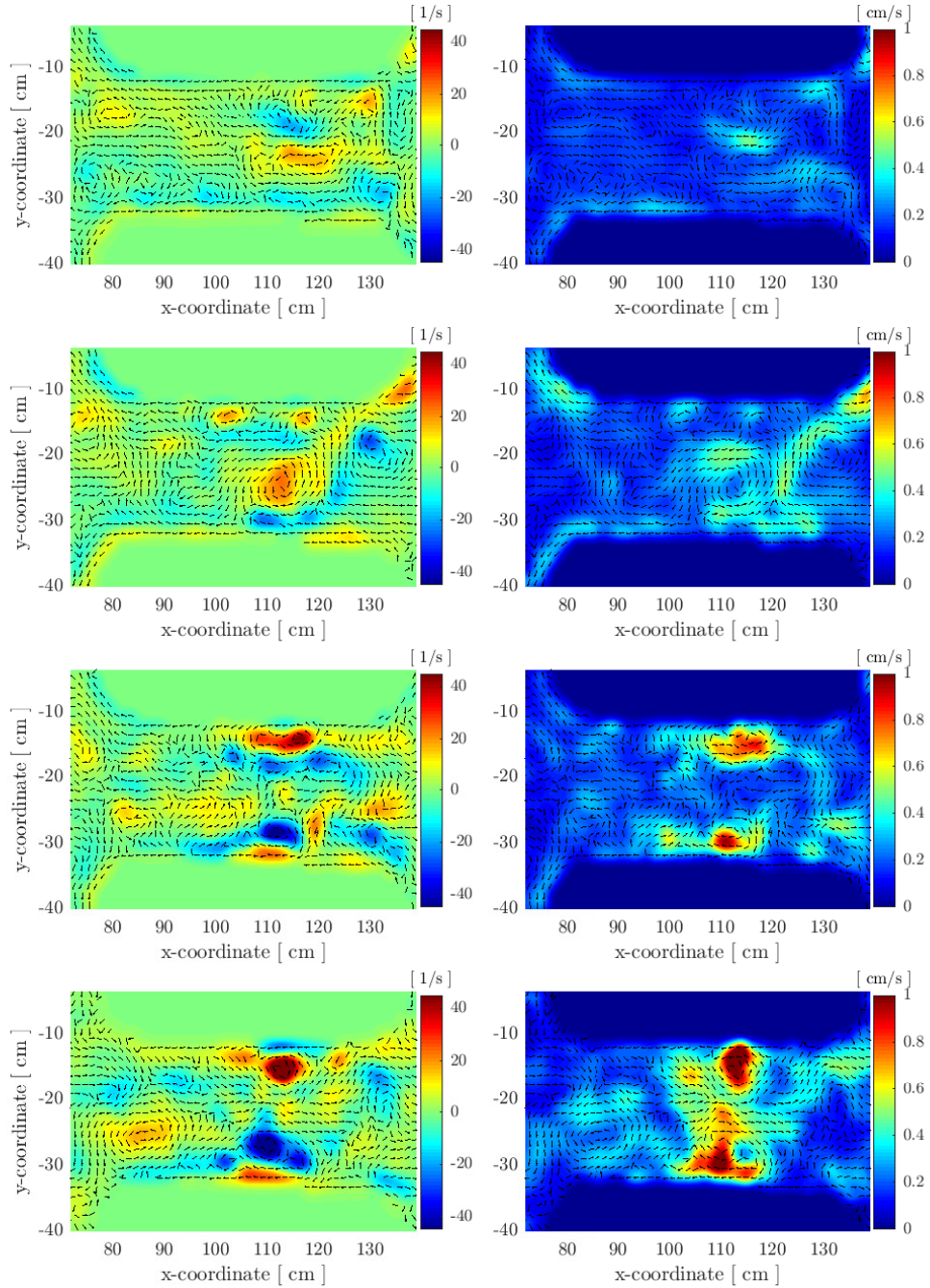
Figure 3.16: Measured vorticity (left) and velocity (right) fields at $t = 0T$, $5T$, $250T$ and $500T$ during flow reversal between flood to ebb in the morphological experiment. The strength of the vorticity cells increases and is located at $x = 110$ cm.
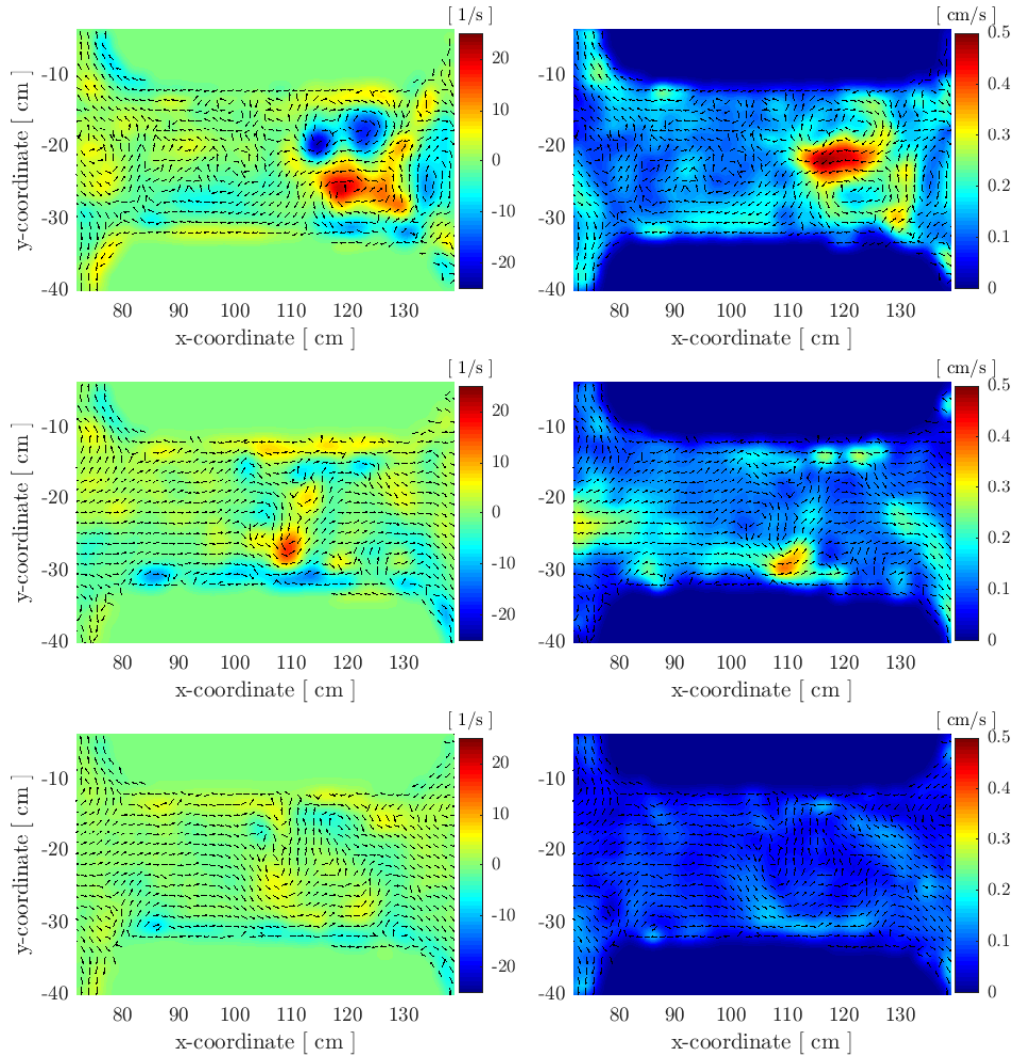
Figure 3.17: Measured vorticity (left) and velocity (right) field during flow reversal between flood to ebb for different water levels $H_W = 5.0$ 6.25 and 7.5 cm in the absence of sediment. The strength of the vorticity cells decrease for increasing H_W. The cells are being transported less far due to the lower velocities as a result of the increasing cross-sectional area in the channel.
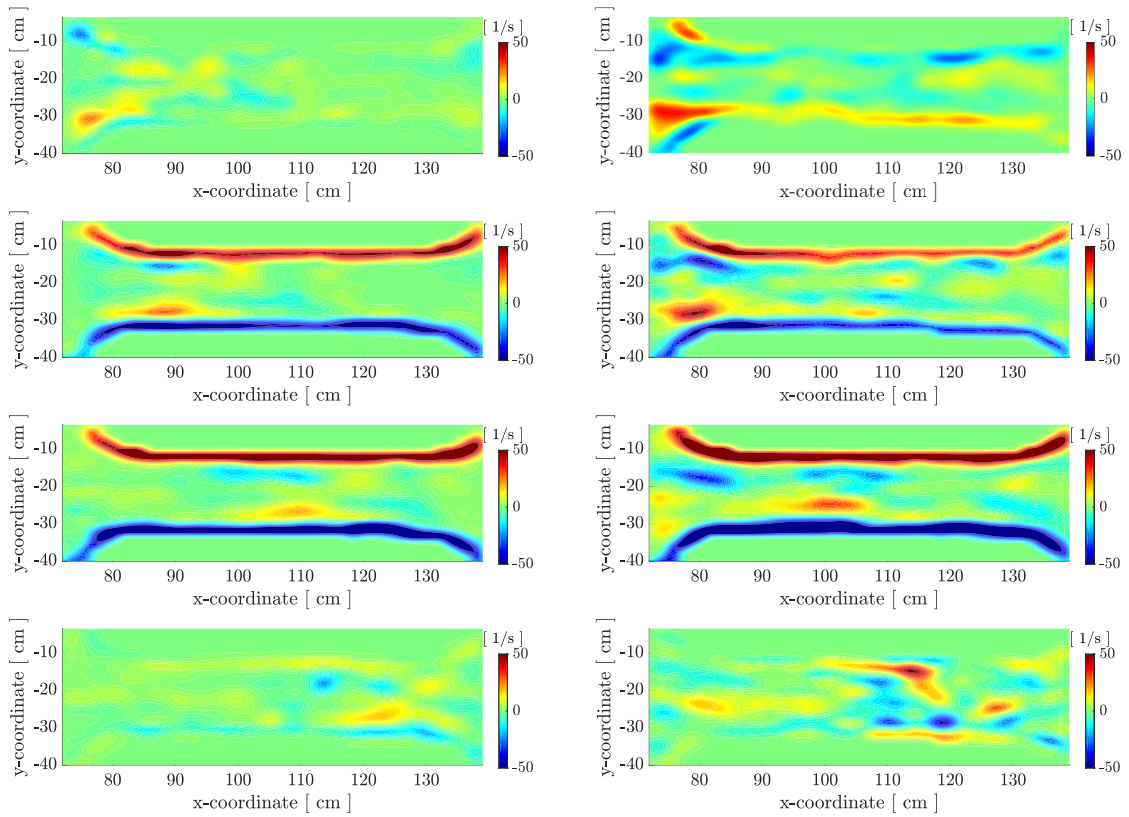
Figure 3.18: Measured vorticity fields during half a tide during the ebb phase for $H_W = 5.0$ cm in the absence of sediment (left) and $H_W = 7.6$ cm from the morphology measurement at $t = 500T$ (right). The formation of the new boundary layers at the channel walls and roll-up of the old boundary layers is shown for both situations at four moments during half a tide. The magnitude of these vorticity cells is stronger in the morphology measurement despite the lower averaged water level indicating the influence of h on the magnitude of the vorticity.

The transient behaviour of the the vorticity cells is shown in figure 3.18. The vorticity field is shown at four moments in half a tide, starting from the flow reversal from ebb to flood. The first column shows the measurements for the situation without sediment with a water level of $H_W = 5$ cm. The second column represents the measured vorticity field at these same moments during the morphological measurement at $t = 500T$. The later contains stronger circulation cells presumably due to the influence of the bottom morphology.

The migration speed of the vorticity cells depends on the velocity fields, and thus on the bed morphology inside the channel. From this experiment we find that the strength of the vorticity cells depends on the bed morphology. Since all these effects are related to each other, and we have only analyzed one situation with sediment, it is not possible to draw conclusions about a (possible) coupling between the measured velocity field and bed morphology.

Chapter 4

Conclusions

The main goal of this study was to implement a measurement technique to perform fast and non-intrusive measurements of the transient bottom under an oscillatory flow with a moving free surface. We presented and tested three different versions, with different levels of complexity, of a pattern matching technique based on the work of Munro, Dalziel & Jehan (2004) and De Zwart (2017), and one photogrammetric technique.

For all techniques, a set of dot patterns is projected onto the sediment bed. Changes in the sediment bed result in deformations in the dot patterns captured by one camera. For the pattern matching technique changes in the horizontal positions of the projected dots are related to the variations in the height of the sediment bed. This relation does not only depend on the changes in bed morphology, but also on the positions of the digital projector and the camera with respect to the measurement area.

In the photogrammetric technique, we calculate the intersection between the light trajectory from the projector to the illuminated dot and the pixel trajectory from the centroid of the dot to the camera. This technique allows to perform underwater measurements where refraction at the water surface is included even if only a dry calibration is made. The main difference between the pattern matching and the photogrammetric technique is the way the calibrations are performed. This difference makes the photogrammetric technique superior in terms of accuracy.

The use of a digital projector allows for a lot of flexibility in the choice of patterns and the rate at which they are projected. However, having some prior knowledge of the bed morphology is required to optimize the resolution and accuracy. Additionally, it is important to take into account that digital projectors are not designed to perform precise measurements. This means that the projection is sometimes unstable and that the projection rate strongly depends on the digital synchronization with the computer.

The photogrammetric technique was implemented in a laboratory setup of a tidal channel together with particle image velocimetry (PIV) to measure the flow velocity at the water surface. Via a discontinuity in the illumination of the projector, it is possible to perform both measurements simultaneously. We investigated the applicability and accuracy of the photogrammetric technique to measure the transient bed morphology under the oscillating tidal flow with a moving free surface. We have shown that the implementation of the photogrammetry technique is fast enough to consider the water level as constant and horizontal during flow reversal. This allows to perform accurate, high-resolution, non-intrusive underwater measurements of the transient bed morphology that can be related to changes in the flow.

4.1   Remarks and recommendations for future work

In this project, we first tested the accuracy of the morphology measurements using perfectly horizontal surfaces at different heights. When the dots are projected on a random bed morphology and the light crosses an interface, they get deformed into ellipses. The information of these deformed ellipses could also be used to calculate the slope of the bed. Moreover, one could make a new photogrammetric calculation where the projected dots are represented by cones instead of single lines. All these versions require an accurate detection of the dot. In this project, we assumed that the centroids of the projected dots/ellipses are the actual centre of the projection on the bed. However, there can be a differences in obtained centroid and the actual centre of the dot on the bed due to the adaptive transformation to binary images, from which the edges of the white areas were used to calculate the ellipse and its centroid. Additional tests where we measure a known curved surface, e.g. a corrugated plate, could give more insight on the actual accuracy of the dot detection and height calculations.

The channel walls are made out of aluminum barriers that started to oxidize and pollute the water. An alternative might be two transparent (perspex) pieces with different heights z_1 and z_2, that can be stacked to form one barrier with height $z_1 + z_2$. This allows to level the sediment bed more easily at a height of z_1. These transparent channel walls can reduce the reflection of light that increased the number of detected dots in current setup. Moreover, it enables to capture the side view of the channel to perform additional measurements. A third improvement, is the leveling of the sediment bed.

The measurements of the water level are performed with a caliper outside the channel and are limited in accuracy due to capillary wetting. A more accurate and non-intrusive method can be implemented where a single dot is projected onto a known reference height. The refracted position of the dot can be calibrated to perform a more accurate and time-dependent water level measurement. The water level at which a projected dot gets refracted is the same level at which this dot is reflected. The reflected pattern from the water surface can thus be used to measure the entire $H_W(x, y, t)$ inside the measurement area. By photographing the reflected projections onto a screen with an additional camera, one can measure the water level using triangulation similar to photogrammetry.

The speed of the pattern projections can be further increased. The connection and timing between the Matlab function *plot* and the actual projection of the pattern is not investigated. More information on this timing can be obtained by triggering the camera before a set of patterns is projected while making a single image with different exposure times. On these particular images, one can investigate the number of different patterns that are being projected during the exposure interval. By varying the pause between two different projections, a minimum duration of the pause between projections can be obtained.[1] Note that the timing is limited by the connection between Matlab and the digital projector. The CPU speed is presumably influencing this connection. An alternative is to project a (repetitive) movie of patterns at $30(/60)$ fps where each frame is a different projection. Using the Vsync of the projector, the camera can be triggered accordingly, increasing the measurement speed. The double CCD camera used for PIV measurements can be used to perform both morphodynamic and PIV measurements at maximum of 30 fps. The camera copies an image to a second (internal) CCD, that allows for very fast consecutive image acquisition where the first acquisition moments can be controlled, together with the exposure time t_{e1} of the first image. The exposure time of the second image is then defined by $t_{e2} = 33.3 - t_{e1}$ milliseconds, i.e. the time it takes for the first image to be send to the computer. The first image could measure the dot patterns whereas the second image captures the luminescent tracer particles whenever they are illuminated by the UV light.

---

[1] The pause was needed in order to project all images. Matlab only projects the final projection if no pause is implemented.

Bibliography

. Aagaard, T., Davidson-Arnott, R., Greenwood, B. & Nielsen, J. "Sediment supply from shoreface to dunes: linking sediment transport measurements and long-term morphological evolution". *Geomorphology* **60,** 205–224 (2004).

. Allen, J. R. "Morphodynamics of Holocene salt marshes: a review sketch from the Atlantic and Southern North Sea coasts of Europe". *Quaternary Science Reviews* **19,** 1155–1231 (2000).

. Baglio, S., Faraci, C., Foti, E. & Musumeci, R. "Measurements of the 3D scour process around a pile in an oscillating flow through a stereo vision approach". *Measurement* **30,** 145–160 (2001).

. Bagnold, R. A. "Motion of waves in shallow water. Interaction between waves and sand bottoms". *Proc. R. Soc. Lond. A* **187,** 1–18 (1946).

. Barnard, P. L., Schoellhamer, D. H., Jaffe, B. E. & McKee, L. J. "Sediment transport in the San Francisco Bay coastal system: an overview". *Marine Geology* **345,** 3–17 (2013).

. Carling, P. A. "Subaqueous gravel dunes". *Journal of Sedimentary Research* **69,** 534–545 (1999).

. Cebrián-Robles, D & Ortega-Casanova, J. "Low cost 3D underwater surface reconstruction technique by image processing". *Ocean Engineering* **113,** 24–33 (2016).

. Christiansen, T, Wiberg, P. & Milligan, T. "Flow and sediment transport on a tidal salt marsh surface". *Estuarine, Coastal and Shelf Science* **50,** 315–331 (2000).

. Claudin, P. & Andreotti, B. "A scaling law for aeolian dunes on Mars, Venus, Earth, and for subaqueous ripples". *Earth and Planetary Science Letters* **252,** 30–44 (2006).

. Coshperic. "Fluorescent Green Polyethylene Microspheres 1.015 g/cc - Various Sizes 355 um to 500 um (0.5 mm)". `https://www.cospheric.com/UVPMSBG_fluorescent_green_spheres_density1015.htm`.

. De Haas, K. "Sediment transport through a tidal inlet between a semi-enclosed basin and the sea. Bachelor's thesis, Eindhoven University of Technology". Bachelor's Thesis (2016).

. De Swart, H. & Zimmerman, J. "Morphodynamics of tidal inlet systems". *Annual review of fluid mechanics* **41,** 203–229 (2009).

. De Zwart, R. "Sediment transport by tidal dipolar vortices at the inlet of a semi-enclosed basin". MA thesis (Eindhoven University of Technology, 2017).

. Dronkers, J. *et al.* "Tidal asymmetry and estuarine morphology". *Netherlands Journal of Sea Research* **20,** 117–131 (1986).

. Duran-Matute, M., Gerkema, T., De Boer, G. J., Nauw, J. J. & Gräwe, U. "Residual circulation and freshwater transport in the Dutch Wadden Sea: a numerical modelling study". *Ocean Science* **10,** 611–632 (2014).

. Elias, E. P. & van der Spek, A. J. "Long-term morphodynamic evolution of Texel Inlet and its ebb-tidal delta (The Netherlands)". *Marine Geology* **225,** 5–21 (2006).

. Fagherazzi, S. & Overeem, I. "Models of deltaic and inner continental shelf landform evolution". *Annu. Rev. Earth Planet. Sci.* **35,** 685–715 (2007).

. Fagherazzi, S. & Sun, T. "A stochastic model for the formation of channel networks in tidal marshes". *Geophysical Research Letters* **31** (2004).

.   Foti, E., Rabionet, I. C., Marini, A., Musumeci, R. E. & Sánchez-Arcilla, A. "Experimental investigations of the bed evolution in wave flumes: performance of 2D and 3D optical systems". *Coastal Engineering* **58,** 606–622 (2011).

.   Friedrichs, C. T. & Perry, J. E. "Tidal salt marsh morphodynamics: a synthesis". *Journal of Coastal Research,* 7–37 (2001).

.   Gorte, B., Vargas-Luna, A. & Sirmacek, B. "Camera-projector 3D scanning of a semi-submerged terrain in a flume". *ISPRS Annals of Photogrammetry, Remote Sensing and Spatial Information Sciences II-4/w1,* 13–18 (2013).

.   Hench, J. L. & Luettich Jr, R. A. "Transient tidal circulation and momentum balances at a shallow inlet". *Journal of Physical Oceanography* **33,** 913–932 (2003).

.   Kleinhans, M. G., Van Rosmalen, T. M., Roosendaal, C. & Vegt, M. "Turning the tide: mutually evasive ebb-and flood-dominant channels and bars in an experimental estuary". *Advances in Geosciences* **39,** 21–26 (2014).

.   Knaapen, M. & Hulscher, S. J. "Regeneration of sand waves after dredging". *Coastal Engineering* **46,** 277–289 (2002).

.   McLaren, P. & Bowles, D. "The effects of sediment transport on grain-size distributions". *Journal of Sedimentary Research* **55,** 457–470 (1985).

.   Munro, R. & Dalziel, S. "Attenuation technique for measuring sediment displacement levels". *Experiments in fluids* **39,** 602–613 (2005).

.   Munro, R., Dalziel, S. & Jehan, H. "A pattern matching technique for measuring sediment displacement levels". *Experiments in fluids* **37,** 399–408 (2004).

.   Porter, K., Simons, R. & Harris, J. "Comparison of three techniques for scour depth measurement: photogrammetry, echosounder profiling and a calibrated pile". *Coastal Engineering Proceedings* **1,** 64 (2014).

.   Raffel, M. *et al. Particle image velocimetry: a practical guide* (Springer, 2018).

.   Ridderinkhof, W., Hoekstra, P., Van der Vegt, M. & De Swart, H. "Cyclic behavior of sandy shoals on the ebb-tidal deltas of the Wadden Sea". *Continental Shelf Research* **115,** 14–26 (2016).

.   Rooij, F., Dalziel, S. & Linden, P. "Electrical measurement of sediment layer thickness under suspension flows". *Experiments in fluids* **26,** 470–474 (1999).

.   Sheng, Y., Peene, S. & Yassuda, E. "Circulation and transport in Srasota Bay, Florida: The effect of tidal inlets on estuarine circulation and flushing quality". *Mixing in Estuaries and Coastal Seas* **50,** 184–210 (1996).

.   Signell, R. P. & Butman, B. "Modeling tidal exchange and dispersion in Boston Harbor". *Journal of Geophysical Research: Oceans* **97,** 15591–15606 (1992).

.   Solari, L., Seminara, G., Lanzoni, S., Marani, M. & Rinaldo, A. "Sand bars in tidal channels Part 2. Tidal meanders". *Journal of Fluid Mechanics* **451,** 203–238 (2002).

.   Stancanelli, L. M. *et al.* "Optical techniques for measuring swash zone morphodynamics". *Coastal Engineering Proceedings* **1,** 33 (2011).

.   Stefanon, L., Carniello, L., D'Alpaos, A. & Lanzoni, S. "Experimental analysis of tidal network growth and development". *Continental Shelf Research* **30,** 950–962 (2010).

.   Sumer, B. M. *et al.* "Backfilling of a scour hole around a pile in waves and current". *Journal of Waterway, Port, Coastal, and Ocean Engineering* **139,** 9–23 (2012).

.   Tambroni, N., Bolla Pittaluga, M. & Seminara, G. "Laboratory observations of the morphodynamic evolution of tidal channels and tidal inlets". *Journal of Geophysical Research* **110,** 1–14 (2005).

.   Van der Linden, S. "Particle dynamics in boundary layers below a swirl flow". MA thesis (Eindhoven University of Technology, 2014).

. Van der Molen, J., Gerrits, J. & De Swart, H. "Modelling the morphodynamics of a tidal shelf sea". *Continental Shelf Research* **24,** 483–507 (2004).

. Wells, M. G. & van Heijst, G.-J. F. "A model of tidal flushing of an estuary by dipole formation". *Dynamics of atmospheres and oceans* **37,** 223–244 (2003).